Tampere University

HEIDI KALLIOJÄRVI

Detection of Single-Diode Model Characteristic Values from Measured Current-Voltage Curves for Online Condition Monitoring Purposes of Photovoltaic Power Systems

Tampere University Dissertations 904

Tampere University Dissertations 904

HEIDI KALLIOJÄRVI

Detection of Single-Diode Model Characteristic Values from Measured Current-Voltage Curves for Online Condition Monitoring Purposes of Photovoltaic Power Systems

ACADEMIC DISSERTATION
To be presented, with the permission of
the Faculty of Information Technology and Communication Sciences
of Tampere University,
for public discussion in the auditorium S2
of Sähkötalo, Korkeakoulunkatu 3, Tampere,
on 19 January 2024, at 12 o'clock.

ACADEMIC DISSERTATION
Tampere University, Faculty of Information Technology and Communication Sciences
Finland

Responsible supervisor and Custos	Professor Emeritus Seppo Valkealahti Tampere University Finland	
Supervisor	Assistant Professor Kari Lappalainen Tampere University Finland	
Pre-examiners	Professor Giuseppe Marco Tina University of Catania Italy	Professor Emeritus Jarmo Partanen LUT University Finland
Opponent	Assistant Professor Patrizio Manganiello Delft University of Technology Netherlands	

The originality of this thesis has been checked using the Turnitin OriginalityCheck service.

Cover design: Roihu Inc.

ISBN 978-952-03-3155-9 (print)
ISBN 978-952-03-3156-6 (pdf)
ISSN 2489-9860 (print)
ISSN 2490-0028 (pdf)
http://urn.fi/URN:ISBN:978-952-03-3156-6

Carbon dioxide emissions from printing Tampere University dissertations have been compensated.

PunaMusta Oy – Yliopistopaino
Joensuu 2023

PREFACE

This dissertation was made at Electrical Engineering Unit of Tampere University between the years 2018 and 2023. The funding was mostly provided by companies and Business Finland, as well as Tampere University. Moreover, a personal grant from KAUTE Foundation is greatly appreciated.

I want to express my deepest gratitude to Prof. Seppo Valkealahti for the supervision of my work and to Assistant Prof. Kari Lappalainen for acting as the second supervisor. The inspiring conversations with Prof. Valkealahti and Assistant Prof. Lappalainen gave me always something new. Your guidance and support carried me over these years. I am also grateful to Prof. Giuseppe M. Tina and Prof. Jarmo Partanen for the pre-examination of my dissertation and to Assistant Prof. Patrizio Manganiello for acting as the opponent. I also thank Prof. Pertti Järventausta, Prof. Emeritus Teuvo Suntio, Associate Prof. Tomi Roinila, Dr. Tuomas Messo and Lasse Söderlund for their help and guidance in practical questions. The support of my other colleagues has been of high value as well. I am especially grateful to Dr. Markku Järvelä, Dr. Roosa-Maria Sallinen, Dr. Jenni Rekola, Dr. Heidi Krohns-Välimäki, M.Sc. Mamoona Akbar and M.Sc. Nida Riaz for their friendship.

Special thanks belong to my entire family and all my precious friends who have walked by my side during this journey. I am happy that you have been sharing these moments with me. Your support has been more than important. I am extremely grateful to my parents Mervi and Hannu for their honest encouragement at every moment. You have never lost your faith in me. Risto, Janne, and Urho, the joy and enthusiasm I see in your eyes has been a support that never loses its power. I love you from the bottom of my heart.

Valkeakoski, October 2023

Heidi Kalliojärvi

ABSTRACT

Photovoltaic (PV) power systems are prone to ageing and degradation occurring in the PV cells during their lifespan. Such phenomena cause significant output power degradation which manifests as economic losses. Hence, a reliable condition monitoring procedure to detect and quantify ageing is a necessity. Such procedures do exist, but they are typically laborious and costly. The present study aims at finding a solution for this problem.

A feasible approach for monitoring the condition of a PV system is to measure the current-voltage curves from the terminals of a PV unit and fit a mathematical model describing the operation of a PV module or a larger PV unit to the curves. The widely used single-diode model is a suitable choice. The fitted model parameters provide valuable diagnostic information on the condition of the PV cells.

However, there are some practical challenges. Firstly, the model parameters are affected by the operating conditions, the measurements of which seldom exist at practical PV sites. This makes it necessary to identify the operating conditions jointly with the model parameters. Secondly, using entire measured current-voltage curves in fitting requires the rundown of the PV system for the measurement period, while using partial current-voltage curves reduces the fit quality. Hence, a systematic study of the effect of the limitation of the measurement range on the fitted parameters is needed. Thirdly, the discrepancies in the current-voltage measurement data make such limitation even more involved. Hence a suitable pre-processing procedure for the measurement data is needed.

These issues are addressed in this thesis from an empirical viewpoint. First, a new pre-processing procedure for the measured current-voltage curves is developed. It can be used to improve the quality of such measurement data, making it more suitable for fitting. Thereafter, a novel single-diode model fitting procedure identifying the operating irradiance and temperature jointly with the actual model parameters is developed. It can be utilized fully without external irradiance or temperature measurements. Finally, the effect of limiting the measurement range of the current-voltage curves to the vicinity of the maximum

power point is systematically investigated, particularly focusing on ageing detection. It is shown how the measurement range of the current-voltage curves can be limited while maintaining the reliable detection of ageing. As a significant result, the developed single-diode model fitting procedure allows for the usage of suitably formed partial current-voltage curves in the parameter identification.

TIIVISTELMÄ

Aurinkosähkövoimalan aurinkokennot ovat järjestelmän elinkaaren myötä taipuvaisia ikääntymään ja rappeutumaan. Ikääntymisilmiöt aiheuttavat merkittäviä tehohäviöitä, mikä ilmenee taloudellisina tappioina. Näin ollen tarvitaan luotettava kunnonvalvontamenetelmä niin kennojen ikääntymisen toteamiseksi kuin ikääntymisen asteen määrittämiseksi. Tällaisia menetelmiä löytyy, mutta niiden käyttö on tyypillisesti työlästä ja kallista. Tämän väitöstutkimuksen tarkoitus on löytää ratkaisu kyseiseen ongelmaan.

Käyttökelpoinen lähestymistapa aurinkosähkövoimalan kunnonvalvontaan on virta-jännitekäyrien mittaaminen aurinkopaneelin tai -paneelikokonaisuuden liittimistä ja aurinkokennon toimintaa kuvaavan matemaattisen mallin sovittaminen mitattuihin käyriin. Malliksi soveltuu laajasti käytetty yksidiodimalli. Mallin sovitteen parametrit tarjoavat diagnostisesti arvokasta tietoa aurinkokennojen kunnosta.

Tässä on kuitenkin eräitä käytännön haasteita. Ensinnäkin yksidiodimallin parametreihin vaikuttavat myös toimintaolosuhteet, joiden mittauksia on harvoin käytännön aurinkosähkövoimaloissa. Täten on tarpeen tunnistaa toimintaolosuhteet laskennallisesti yhdessä yksidiodimallin parametrien kanssa. Toiseksi kokonaisten virta-jännitekäyrien käyttö sovitukseen vaatii voimalan alasajon mittausjakson ajaksi, kun taas osittaisten virta-jännitekäyrien käyttö heikentää sovitteen laatua. Näin ollen järjestelmällinen tutkimus mittausalueen rajoittamisen vaikutuksesta sovitteen antamiin parametreihin on tarpeen. Kolmanneksi virta-jännitemittausdatassa esiintyvät poikkeamat tekevät mittausalueen rajoittamisesta entistä hankalampaa. Täten tarvitaan sopiva mittausdatan esikäsittelymenetelmä.

Näitä kysymyksiä käsitellään tässä väitöskirjassa kokeellisesta näkökulmasta. Ensiksi kehitetään uusi esikäsittelymenetelmä mitatuille virta-jännitekäyrille. Menetelmää voidaan käyttää parantamaan mittausdatan laatua, mikä tekee datan soveltuvammaksi yksidiodimallin sovittamiseen. Seuraavaksi kehitetään uusi yksidiodimallin sovitusmenetelmä, joka tunnistaa laskennallisesti varsinaisten yksidiodimallin parametrien ohella toimintalämpötilan ja -säteilyvoimakkuuden.

Menetelmää voidaan käyttää täysin ilman ulkoisia säteilyvoimakkuus- ja lämpötilamittauksia. Lopuksi tarkastellaan järjestelmällisesti virta-jännitekäyrien mittausalueen rajoittamista maksimitehopisteen ympäristöön keskittyen lähinnä ikääntymisen tunnistamiseen ja näytetään, miten virta-jännitekäyrien mittausaluetta voidaan rajoittaa niin, että ikääntyminen saadaan yhä tunnistettua luotettavasti. Merkittävä tulos on, että kehitetty yksidiodimallin sovitusmenetelmä mahdollistaa sopivasti mitattujen osittaisten virtajännitekäyrien käytön parametrien tunnistamisessa.

CONTENTS

SYMBOLS AND ABBREVIATIONS

Abbreviations

a-Si	amorphous silicon
AC	alternating current
AR	anti-reflective
BJT	bipolar junction transistor
CdTe	cadmium telluride
CIGS	copper indium cadmium diselenide
DC	direct current
EIA	US Energy Information Administration
EL	electroluminescence
ESR	equivalent series resistance
EVA	ethylene vinyl acetate
Fraunhofer ISE	Fraunhofer Institute for Solar Energy Systems
IEA	International Energy Agency
IGBT	insulated gate bipolar transistor
IQR	interquartile range
IRENA	International Renewable Energy Agency
IRT	infrared thermography
LID	light-induced degradation
mc-Si	multi-crystalline silicon
MOSFET	metal-oxide-semiconductor field-effect transistor
MPP	maximum power point
MPPT	maximum power point tracking
n-type	negative type
NASA	National Aeronautics and Space Administration
OC	open-circuit
p-type	positive type
PID	potential-induced degradation
PV	photovoltaic
RMSE	root mean square error

Si	silicon
SQL	structured query language
STC	Standard Test Conditions
TAU	Tampere University
THD	total harmonic distortion
WHO	World Health Organization

Greek alphabet

γ_I	ratio of maximum power point and short-circuit currents
γ_U	ratio of maximum power point and open-circuit voltages
ΔI_{MPP}	change in maximum power point current
ΔR_h	change in shunt resistance
ΔR_s	change in series resistance
ΔU_{MPP}	change in maximum power point voltage

Latin alphabet

A	ideality factor
FF	fill factor
FF_{STC}	fill factor at Standard Test Conditions
G	irradiance
G_{eff}	efficient irradiance
G_{STC}	irradiance at Standard Test Conditions
I	current
I_D	drain current
I_{MPP}	current at maximum power point
$I_{MPP,STC}$	current at maximum power point at Standard Test Conditions
I_o	dark saturation current
I_{o1}	dark saturation current in quasi-neutral regions
I_{o2}	dark saturation current in depletion region
I_{ph}	photocurrent
$I_{ph,STC}$	photocurrent at Standard Test Conditions
I_{SC}	short-circuit current
$I_{SC,STC}$	short-circuit current at Standard Test Conditions
k_B	Boltzmann constant
K_I	temperature coefficient of short-circuit current at Standard

	Test Conditions
K_U	temperature coefficient of open-circuit voltage at Standard Test Conditions
NFF	normalised fill factor
N_s	number of series-connected PV cells
$N\Delta R_h$	normalised change in shunt resistance
$N\Delta R_s$	normalised change in series resistance
P	power
P_{MPP}	power at maximum power point
q	electron charge
R_h	shunt resistance
$R_{h,STC}$	shunt resistance at Standard Test Conditions
R_s	series resistance
$R_{s,add}$	additional series resistance
$R_{s,STC}$	series resistance at Standard Test Conditions
SPR	serial-parallel ratio
T	temperature
T_{STC}	temperature at Standard Test Conditions
U	voltage
U_{DS}	drain-source voltage
U_{GS}	gate-source voltage
U_{MPP}	voltage at maximum power point
$U_{MPP,STC}$	voltage at maximum power point at Standard Test Conditions
U_{OC}	open-circuit voltage
$U_{OC,STC}$	open-circuit voltage at Standard Test Conditions
U_T	thermal voltage

1 INTRODUCTION

The ongoing battle against climate change requires continuous actions to be taken. Indeed, climate change is currently considered the largest threat to global health (World Health Organization (WHO), 2021). A key feature of climate change is global warming. Such warming mainly results from the emission of greenhouse gases into the Earth's atmosphere. These emissions originate largely from the usage of fossil fuels in energy production. This detrimental development has rendered the need to replace fossil fuels in energy production with non-fossil energy sources whenever possible. This holds especially for electricity production. (International Energy Agency (IEA), 2021; United Nations, 2023.)

The alternative option for fossil fuels in electricity production is provided by sources of renewable energy. Remarkably, the substitution of fossil fuels by renewable energy sources in energy production belongs to the most significant actions in climate change mitigation. The share of renewable energy from global electricity production was estimated to be almost 29% in 2020 (IEA, 2021). The major renewable energy sources include solar photovoltaic (PV) power, wind power, bioenergy and hydropower; some other forms of renewable energy also exist such as geothermal energy and tidal energy (US Energy Information Administration (EIA), 2022).

Of the renewable energy sources, solar PV energy is globally the fastest growing (IEA, 2021); its growth has been exponential for the past few decades. By the end of 2012, the global solar PV power installation capacity was 104 GW, whilst by the end of 2021 the corresponding figure was 849 GW (International Renewable Energy Agency (IRENA), 2022). However, the conversion of light into electricity is not a modern invention as such; the photoelectric effect was discovered by Edmond Becquerel in 1839 but explained by Albert Einstein in 1905 (Copeland et al., 1942; Millikan, 1914). Since then, the various steps taken to better understand the PV effect principles and develop the PV cell technologies have enabled the establishment of the wide-scale utilisation of PV power systems in electrical energy production. This development has been further enhanced by the indisputable advantages of solar PV power as an energy resource. Firstly, there

exists no threat of lacking manufacturing material: silicon (Si), being the most common manufacturing material, is widely available and inexpensive. Secondly, the manufacturing process causes only low emissions to the atmosphere. Indeed, the carbon footprint of PV was estimated to be approximately 2% of that of coal in 2015 (Solar Power Europe, 2022). Thirdly, PV systems cause no emissions or other disturbances to their environment during their operation. Unlike wind turbine systems which feature noise and flashing lights, solar PV systems are quiet and inconspicuous. Fourthly, solar PV systems can be specifically sized and scaled according to the need, purpose, and location, which enables their versatile usage. A PV system can either be connected to the power grid or constitute a stand-alone system so that the excess energy is stored into rechargeable batteries. Finally, solar energy is inexhaustible and, as such, overwhelmingly sufficient to cover the global energy need. These aspects make solar PV power an ecologically and economically viable tool for electricity production.

The performance and lifetime of a PV system depend strongly on the condition of its PV modules. However, how to maintain sufficiently good condition of the PV modules throughout their expected operational lifetime is far from obvious. Regardless of the warranties guaranteed by the manufacturers, PV modules tend to suffer from a variety of unpredictable and often premature degradation and ageing phenomena during the course of their lifespan (Manganiello et al., 2015). Indeed, such mechanisms occurring in PV modules may drastically decrease the output power of the PV system. Hence the ageing and degradation of PV modules should be detected early. However, the visual inspection of such defects is often neither economically feasible nor quantitatively reliable. This makes the exploitation of specific condition monitoring procedures mandatory. A useful tool for such purposes is provided by the electrical current-voltage (*I-U*) characteristic curves measured from the terminals of a PV system. Such an approach is characterised by quantitative accuracy and applicability to most PV systems when compared to other techniques such as electroluminescence (EL) or infrared thermographic (IRT) imaging of PV modules, which require the use of drones or other specific high-cost equipment and might be complex (Ahmad et al., 2019; Fadhel et al., 2019).

Much effort has been put in the literature into developing different condition monitoring approaches based on measured *I-U* curves to detect ageing and degradation occurring in PV systems. Such approaches often rely on the fitting of the mathematical single-diode model describing the operation of a PV cell, module, or larger PV unit to the experimental *I-U* curves measured from the PV

system. Indeed, the magnitude, variation, and drift in the theoretical single-diode model parameters that are mathematically identified from measured *I-U* curves can reveal the occurrence of changes in the characteristics of the PV cells (Petrone et al., 2017b). However, most of the existing condition monitoring approaches based on the single-diode model parameter identification demand the measurement of the operating irradiance and temperature of the PV system. Without such information, no diagnostic conclusions can be drawn, as the parameter values are also affected by the operating conditions. Unfortunately, there seldom exist irradiance or temperature sensors at practical PV sites, and if they do exist, they are placed in a specific location, thus not representing the operating conditions of all the PV modules of the installation. Most importantly, inverter manufacturers aim to analyse the *I-U* curves independently of other measurement systems. Hence, the simultaneous mathematical identification of operating irradiance and temperature jointly with the single-diode model parameters is mandatory. However, only few published studies (Lappalainen et al., 2020; Lappalainen et al., 2022a) have addressed this issue by presenting such procedures. In Lappalainen et al. (2020), explicit equations are used instead of more accurate iterative ones. Lappalainen et al. (2022a) does exploit iterative equations, but a large number of equations is needed, which increases the complexity of the method. This renders the need to develop an iterative method with fewer equations. One of the aims of this thesis is to fill this gap, so that the operating irradiance and temperature become simultaneously identified.

After developing a single-diode model fitting procedure with operating condition identification capabilities, another major challenge remains regarding the applicability of the model for condition monitoring at real PV sites. The problem is that for most single-diode model parameter identification approaches, the usage of partially measured *I-U* curves is insufficient for reliable parameter identification (Petrone et al., 2017a). However, the entire curve from beginning to end cannot be measured during the normal operation of the PV system, as it rather requires a temporary rundown of the PV system. Such undesired interruptions in electricity production and the consequent disturbances to the power system could be avoided if only partial *I-U* curves in the vicinity of the maximum power point (MPP) were measured. However, such a reduction of the measured *I-U* curve portion reduces the accuracy of the fitted parameters and thus weakens the reliability of the diagnosis. Hence it is reasonable to ask how the measurement region of the *I-U* curve should be limited. The literature offers single-diode model identification approaches operating on reduced *I-U* curve measurement data. However, they

typically show only one or two examples on the formation of a partial *I-U* curve used for fitting. Consequently, the optimal choice for the measured portion of the *I-U* curve for single-diode model parameter identification still remains unclear. To address this issue, Lappalainen et al. (2022a) systematically investigated the effect of *I-U* curve cutting on the fitted parameters by utilising percentages of the MPP power (P_{MPP}) as the cutting limits. Unfortunately, the used dataset comprises only a small number of *I-U* curves, whence there exists no statistically reliable study on the effects of the selection of the measurement region of the *I-U* curve on the fitting accuracy of the single-diode model. In addition, no other principle for limiting the measurement region of the experimental *I-U* curve has been investigated than the MPP power-based approach mentioned in Lappalainen et al. (2022a). However, as voltage acts as the reference quantity of the inverter, the performance of an MPP voltage (U_{MPP}) based *I-U* curve cutting in the single-diode model fitting should be investigated as well. These issues constitute a clearly missing area of the literature and addressing them is one of the tasks of this thesis.

A practical challenge appearing in the fitting of the single-diode model to experimental *I-U* curves gathered from real-case PV systems is the poor quality of the measurement data. Indeed, the measured *I-U* curves might be noisy, discrepant, and suffer from measurement errors and other inaccuracies. Ignoring such inconsistencies in the data before fitting might lead to inaccurate fitting results and hence to unreliable diagnostic conclusions. However, the literature yet lacks a sophisticated, systematically constructed pre-processing procedure for raw measured *I-U* curves which is applicable to any curve regardless of the used measurement device. This forms a research gap, the filling of which is also one of the tasks of this thesis.

In light of the above discussion, the following research questions are raised:

- How to pre-process the measured current-voltage curves in order to remove their discrepancies?
- How to implement a simple single-diode model fitting procedure identifying also the operating irradiance and temperature?
- How the limitation of the measurement range of the current-voltage curves used for fitting affects the fitted parameters?

Addressing these three issues, the achievements of this thesis are the following:

- the development of a universal pre-processing procedure (Kalliojärvi-Viljakainen et al., 2020a; Kalliojärvi-Viljakainen et al.,

2020b) for noisy and discrepant *I-U* curve measurement data to improve the fitting quality

- the development and validation of a novel *I-U* curve fitting procedure (Kalliojärvi-Viljakainen et al., 2022) to identify single-diode model parameters jointly with operating irradiance and temperature from experimental *I-U* curves
- the systematic comparative testing of the developed fitting procedure for partially measured *I-U* curves based on either P_{MPP} or U_{MPP} percentages (Kalliojärvi et al., 2022) from the online condition monitoring point of view, with the main focus on series resistance parameter identification.

This thesis provides a fully mature step-by-step PV module single-diode model parameter identification procedure. The developed procedure can be used for the further design of online condition monitoring applications.

The author wrote this dissertation and all publications related to it. Assistant Prof. Kari Lappalainen implemented the simulation model (Villalva et al., 2009) used for initial testing of the research hypotheses and was responsible for the curation of the experimental measurement data used in this work. Prof. Seppo Valkealahti outlined the scope of the research. Assistant Prof. Lappalainen and Prof. Valkealahti provided guidance throughout the research process and gave fruitful comments on the substance.

The remainder of this thesis is organised as follows. In Chapter 2, the necessary background is revised. Chapter 3 is dedicated to describing the mathematical modelling of the PV systems. In particular, the single-diode model fitting procedure developed for this thesis is presented. Chapter 4 is devoted to the issues related to the *I-U* curve measurement data. In particular, the developed pre-processing procedure is presented. Chapter 5 is dedicated to the validation of the developed single-diode model fitting procedure for entire measured *I-U* curves. Chapter 6 shows the parameter identification results for partial *I-U* curves measured in the vicinity of the MPP. Chapter 7 focuses on showing the ageing detection capabilities of the developed single-diode fitting procedure. Chapter 8 provides discussion and criticism concerning the choices made during the study. Further research topics are also suggested. Chapter 9 summarises the conclusions and significance of the research work.

2 BACKGROUND

2.1 Solar energy

The Sun serves as the primary energy source for the Earth. Its core is mainly composed of hydrogen and helium. Being subjected to high heat and pressure, it allows for the occurrence of a nuclear fusion reaction uniting hydrogen atoms into helium atoms. The obtained helium atom has a mass smaller than that of the original hydrogen atoms. Thus, it follows from the relativity theory that such a loss in mass is released as extra nuclear energy. This nuclear energy then travels through the successive layers of the Sun and becomes converted into thermal energy, which radiates into space in the form of electromagnetic waves. (Häberlin, 2012.)

These electromagnetic waves proceed in empty space at an approximate speed of 300 000 km/s. The wavelength of this radiation varies from 0.3 to 3 μm, its spectrum following that of a black body radiator at 5800 K temperature (Luque and Hegedus, 2003). As explained by Albert Einstein, the electromagnetic radiation originating from the Sun can be alternatively interpreted as minutely small light quanta called photons. Each photon is characterised by its energy and momentum. These two properties depend on the frequency of the corresponding electromagnetic wave. This discretisation of the initially continuous notion of electromagnetic solar radiation helped Einstein to explain the photoelectric effect (Niaz et al., 2010).

The total power of solar radiation is 3.85×10^{26} W (Häberlin, 2012), of which 170 000 TW reaches the Earth (Guerrero-Lemus and Martinez-Duart, 2012). However, 29% of that amount is reflected back into space. Hence, only the remaining 121 000 TW (71%) is absorbed by the Earth's atmosphere and surface (National Aeronautics and Space Administration (NASA), 2009). For comparison, the global annual energy consumption is estimated to be 160 000 TWh (Nuclear Power, 2023). It follows that the solar radiation produced in approximately 1 hour and 20 minutes would suffice to cover annual global energy consumption. Theoretically, the full coverage of the global energy demand could be achieved with a nominal power generation of 18.3 TW having full-time peak-power

operation. The global capacity of the PV installations exceeded the mark of 1 TW in April 2022 (PV Magazine, 2022), whence the contribution of PV power in meeting the demand for energy production is significant.

The averaged irradiance during the year at the edge of the Earth's atmosphere is approximately 1367 W/m^2, with the actual irradiance values varying between 1322 and 1414 kW/m^2. This figure is called the solar constant. Only part of the solar radiation arriving at the edge of the Earth's atmosphere succeeds in reaching the surface of the PV modules of an installed power system. The diminishing of the radiation in the atmosphere occurs via scattering, absorption, and reflection. In this spirit, solar radiation can be divided into direct, diffuse, and reflected components, respectively. (Häberlin, 2012.) The amount of irradiance arriving at the Earth's surface depends strongly on the location, the season, and the time of day. For instance, the irradiance received by the PV modules of the TAU PV power research plant at Tampere University in summertime can reach up to 900 W/m^2 in clear sky conditions. In contrast, the cloud enhancement phenomenon in partially cloudy conditions can raise this figure as high as 1.4 kW/m^2 or even more, with the diffuse irradiance being around 100 W/m^2. (Järvelä et al., 2020; Lappalainen et al., 2022b.).

2.2 Photovoltaic effect and photovoltaic cells

Being composed mainly based on the presentations appearing in the books Fraas and Partain (2010), Häberlin (2012), Kittel (2005), and Luque and Hegedus (2003), this section provides an insight into the operational principle of PV cells. Basically, a PV cell is a semiconductor diode device exploiting the photovoltaic effect to produce electricity. The most commonly used PV cell material is crystalline silicon, dominating the global market with a 95% share (Fraunhofer Institute for Solar Energy Systems (ISE), 2022). Hence the case of a typical silicon PV cell is used as the example below.

In order to understand the background of the photovoltaic effect occurring inside semiconducting material, a short revision of the energy level and energy band structures of such a material is needed. As a familiar example, the energy levels of an atom are typically illustrated as circular orbits around its nucleus according to the model presented by Niels Bohr. It follows from the quantisation of energy that an electron lying in a solid material can only have certain stepwise-located energy levels: no electron can possess an energy between these levels.

Returning to the atom example, an electron cannot be located between two adjacent orbits. The range of the allowed energy levels in material for electrons located in a close proximity to each other can be considered as a sequence and is therefore called an energy band. Any electric current in the material consists of the movement of electrons in its energy bands, in practice in the conduction band. Obeying the minimum energy principle, the electrons tend to occupy the lowest possible energy levels. Hence, the energy bands are filled in order from the bottom to the top. The upper limit for such filling is called the Fermi energy level. In semiconducting materials, the lower and upper energy bands immediately surrounding the Fermi energy level are the valence and conduction bands, respectively. In contrast, the Fermi energy level in conductors lies in the conduction band.

The empty gap appearing between the conduction and valence bands in semiconductors and insulators is called the band gap. It contains no allowed energy levels for electrons. Remarkably, the band gap of a semiconductor is narrow, whence a moderate amount of energy is needed for an electron to surpass it. Such energy is called band gap energy, being 1.121 eV for silicon at the Standard Test Conditions (STC) temperature. The band gap energy has a strong negative temperature dependence. Only those electrons receiving external energy equal to or larger than the band gap energy can be lifted from the valence band to the conduction band and make a positively charged hole appear in the valence band. It is exactly this process which makes semiconducting material conductive.

Like all semiconductor diode devices, PV cells are based on the p-n junction. Such a junction is generated by combining two different types of semiconducting material. The formation of such materials is performed by a process called doping. Therein, specific impurities like boron or phosphorous atoms are added to the crystalline structure of silicon in a controlled manner. Doping regulates the number of charge carriers in the energy bands of the semiconducting material. The usage of different dopants leads to obtaining different types of doped semiconductors. More precisely, the doping can be performed by providing either extra electrons in the conduction band or extra holes in the valence band. The former situation can be achieved, for instance, by using phosphorous as the dopant. Silicon has four valence electrons in the outermost electron shell, whilst phosphorous has five valence electrons. In the doping process, each phosphorous atom donates the extra electron to the conduction band. Such a dopant is therefore called a donor, and the resulting doped material is called a negative type (n-type) semiconductor. The latter situation

is reached, for instance, by using boron as the dopant. Boron has only three valence electrons. Hence each boron atom accepts an extra electron from the valence band, making a hole appear in the valence band. Boron is therefore called an acceptor. The resulting doped material is called a positive type (p-type) semiconductor.

A p-n junction is constructed by joining p- and n-type materials. The attachment of these differently doped materials together makes the electrons in the n-type region diffuse around inside the material. The diffusion of the electrons away from the n-type material creates a space charge zone into the n-type material that includes positively charged donor ions. Accordingly, as the p-type material receives the diffused electrons, a space charge zone characterised by negatively charged acceptor ions appears in the p-type material. Some of the diffused electrons fill holes in the p-type material. It follows that the two space charge zones form together a region called a depletion region. The depletion region is charge-neutral when considered as a whole, but a clear charge distribution is present inside it. Indeed, all the charge carriers lying on the depletion region are fixed and no mobile charge carriers exist there. Thus, the depletion region separates the positive and negative mobile charge carriers from each other. The mobile charge carriers are located outside the depletion region in the so-called quasi-neutral regions. The described process creates an internal electric field across the p-n junction. In particular, a built-in voltage is formed over the depletion region. The built-in voltage is the origin of the open-circuit (OC) voltage (U_{OC}) of a PV cell, which in turn is obtained from the p-n junction by attaching electrical contacts to the edges of the quasi-neutral regions.

Ultimately, the production of current using a PV cell is possible by exposing it to light. The photons received by the semiconducting material possess a certain amount of energy which then becomes absorbed by the electrons lying in the valence band. If the absorbed energy exceeds the band gap energy, the electrons are lifted to the conduction band. Consequently, there appear holes in the valence band. Having arrived at the conduction band, the electrons can diffuse freely. Some of the diffusing electrons find their way into the p-n junction. Therein, the internal electric field accelerates the wandering of the electrons from the p-n junction towards the n-type material. In accordance with the movement of electrons in the conduction band, the holes move in the valence band. This process results in a flow of electric current inside the material. The phenomenon is referred to as the photovoltaic effect. The photovoltaic effect closely resembles the photoelectric effect initially discovered by Becquerel. The difference is that in the

latter case, the electrons spread out to the surrounding space rather than being kept detained inside the material structure.

Individual PV cells are characterised by low output voltage and current. To extract more output power, the PV cells are connected in series to form a larger unit called a PV module. A typical PV module structure consists of series-connected PV cells, divided into blocks of PV cells, each protected by a bypass diode. The purpose of bypass diodes is to protect the PV cell, for example, from localised heating phenomena resulting from partial shading or other sources of mismatch (Vieira et al., 2020). Indeed, such heating can lead to the appearance of hot spots which can damage the PV module permanently. Finally, PV modules can be connected in series and parallel configurations to form an array of the appropriate size. (Petrone et al., 2017b.)

The first silicon PV cell with practical applicability was invented in 1954 by Bell Laboratories in the US with an efficiency of 6%. For reference, the best reported efficiency for silicon PV cells is 27.6% (Green et al., 2022). During the first few decades of PV cell manufacturing, the used material was mono-crystalline silicon. Thereafter, the repertoire was complemented with PV cells fabricated of multi-crystalline silicon (mc-Si). Later, alternative PV cell technologies such as amorphous silicon (a-Si), thin-film cadmium telluride (CdTe), and copper indium gallium selenide (CIGS) have been introduced, each with its own specific features.

2.3 Degradation and ageing of photovoltaic cells

During their lifespan, PV modules are prone to different degradation phenomena occurring in the PV cells. According to Lannoy and Procaccia (2005), degradation can be defined as 'the gradual deterioration of the characteristics of a component or of a system which may affect its ability to operate within the limits of acceptability criteria and which is caused by the operating conditions'. Ageing of PV cells is one such phenomenon. For financial and technical reasons, ageing should be detected reliably and in time. Firstly, Bastidas-Rodriguez et al. (2015) pointed out that the resulting reduction in power output manifests as increments in the payback time of the investment put into the PV system. Secondly, it not only impedes the optimal utilisation of the PV system but also causes additional damage in a cumulative fashion. For instance, Manganiello et al. (2015) highlighted that ageing and mismatching constitute a closed loop; the nonuniform ageing of PV

cells causes mismatching, whilst the thermal effects stemming from mismatching cause ageing.

Given the possible defects and degradation effects during the PV module lifespan, manufacturers have provided two-fold warranties for commercial modules. The product warranty is there to cover material defects as well as those caused by the actual manufacturing process. The length of the warranty period is determined by the PV module manufacturer: the minimum is 10 years, the typical warranty period being 15-25 years. The performance warranty is there to guarantee that the electrical performance does not fall below the acceptable degradation rate. Typically, the PV module performance warranty is 25-30 years. The allowed average annual degradation rate depends on the length of the warranty period, among other factors. However, it has been outlined that annual degradation rates higher than 0.8%/year are too high to meet a 25-year performance warranty. (Prieto-Castrillo et al., 2020)

Regardless of the warranties guaranteed by the manufacturers, premature ageing processes occur in PV cells (Manganiello et al., 2015). In general, defects in PV modules are not rare. Moreover, Fernandes et al. (2016) observed that 25% of the reported defects in actual PV modules occurred during the first operational year. During the second year, the number is still 15%. Consequently, various case studies have verified that the acceptable degradation rate has been exceeded. The mean peak power degradation reported in Lillo-Sanchez et al. (2021) was 30.9% after 22 operational years, which is equivalent to an annual degradation of 1.4%/year. Azizi et al. (2018) also reported that an almost 30% power reduction may occur in 20 operational years. In Sanchez-Friera et al. (2011), the reported peak power loss after 12 operational years was 11.5%. Tan et al. (2022) investigated the lifetime of PV modules in Australia, ending up with practical lifetimes of only 15-20 years. A more optimistic number was provided by Fernandes et al. (2016), stating that PV modules manufactured after 2000 would lose only 12% of their performance in 25 operational years. However, it was strongly emphasised that such an outcome requires sufficient maintenance of the PV system. Such findings reflect the difficulty of predicting the progress of ageing as well as the need to utilise condition monitoring procedures to work out appropriate maintenance measures.

There are several potential causes for premature ageing, such as long periods of outdoor exposure, insufficient maintenance, and problems in the enclosure of the PV module, to name but a few (Bastidas-Rodriguez et al., 2015).

Consequently, there are also many ageing mechanisms occurring in PV modules. Manganiello et al. (2015) summarised the most common ageing mechanisms.

Corrosion is a common ageing mechanism in PV modules occurring in the metallic parts of the PV module. It is strongly accelerated by hot and humid operating conditions. The presence of corrosion is often tied to other defects and ageing phenomena explained in the following.

Discoloration is a term used for the browning and yellowing of PV cells. It follows from the degradation of the encapsulant material (ethylene vinyl acetate, EVA) resulting from ultraviolet (UV) radiation and high operating temperatures. Light yellowing is caused by thermal discoloration, while dark browning results from photothermal processes or penetration of oxygen from the rear of the PV module to the front (Kouadri-Boudjelthia et al., 2021). Wohlgemuth et al. (2013) reported that EVA discoloration is a major cause of power degradation in crystalline silicon PV modules; field-aged modules tend to suffer from browning rather than yellowing (Kaplani, 2012). As a cumulative effect, discoloration causes corrosion in metallic cell busbars (Sinha et al., 2016).

Delamination is defined as weakened adhesion between the structural layers of the PV module. As stated by Manganiello et al. (2015), it has many origins. Firstly, environmental stresses make the PV cells and their interconnectors move apart from each other. Secondly, thermal expansion of humidity and air detained in the PV module burdens the structure of the module. Thirdly, humidity jointly with UV radiation cause solder bond defects. Fourthly, high operating temperatures engender the vaporisation of the encapsulant, which allows for the intrusion of water into the PV module. This in turn leads to corrosion. Delamination also causes dispersion of light, whence the reflective losses increase. A visible sign of PV module frontside delamination is a white or milky pattern (Sanchez-Friera et al., 2011).

The formation of bubbles inside the PV module originates from thermal decomposition and chemical reactions occurring in the material. Such reactions free gases inside the PV module. Having been detained inside the PV module structure, the bubbles create an air chamber characterised by a lower temperature than that of the neighbouring region. This makes it difficult for heat to dissipate from the area surrounding the bubble, making the PV cell overheat. This can lead to the appearance of hot spots which may damage the PV cells permanently. Bubbles located on the front of the PV cell also diminish the irradiance received by the PV cell. This leads to dispersion of light and an increase in reflective losses. If bubbles inside the PV module break, the back sealing surface might become

broken as well. This in turn allows water to intrude into the PV module. (Manganiello et al., 2015.)

The anti-reflective (AR) coating of the PV cell is prone to degradation due to the radiation received during PV system operation and oxidation enabled by the loss of adhesion between the PV cell and its encapsulant. Moreover, AR coating degradation accelerates due to the presence of high voltages with respect to the ground. This degradation type can be observed as colour changes of the coating. (Manganiello et al., 2015.)

The ribbon, solder bonds, and other metallic parts of the PV module are also prone to degradation and possible breakage. Possible causes include thermal expansion stresses. In particular, high temperatures make the metallic parts degrade faster. (Manganiello et al., 2015.)

The silicon wafers of the PV cells can break as well. The breakage can be caused by mechanical or thermal stresses as well as carelessness during treatment such as shipping, installation, or maintenance. Cracks may cause localised heating phenomena such as hot spots and lead to the existence of isolated regions inside the PV cell. Consequently, the *I-U* curves measured from the defective PV module resemble those obtained during partial shading with multiple MPPs. (Manganiello et al., 2015.)

Dust and soiling covering an area of the surface of PV module is a direct cause of partial shading. The shaded PV cells might act as a load, which in turn generates hot spots. Hot spots can also be generated via defects in the junction box and bypass diodes. (Manganiello et al., 2015.)

Light-induced degradation (LID) is a loss in the efficiency of a silicon solar cell due to boron-oxygen defects or copper contamination. However, not all the mechanisms behind LID are clear. LID manifests as decreased diffusion lengths of minority carriers and increased recombination rates. (Lindroos and Savin, 2016; Sopori et al., 2012.)

Potential-induced degradation (PID) originates from leakage currents between the PV cell and the frame of the module that are caused by high voltages. PID is further enhanced by humidity and high temperatures. The different types of PID include the dissolution of the AR coating and the degradation of the metallisation grid, among others. However, the most common PID effect is that of shunting. (Manganiello et al., 2015.)

The occurrence of the different degradation phenomena varies according to the outdoor environment, the material, and the type of PV modules as well as their operational age, among other factors (Manganiello et al., 2015). The authors

reported that the most common degradation mechanism for aged PV modules fabricated of crystalline silicon is EVA encapsulant degradation, with second place held by solder degradation. In similar spirit, Rabii et al. (2003) observed EVA browning to be the main ageing mechanism in field-aged multi-crystalline PV cells. Sanchez-Friera et al. (2011) observed that the most frequent forms of degradation were glass weathering, delamination, and oxidation of the AR coating and PV cell metallisation grid. In turn, the most significant defects found by Lillo-Sanchez et al. (2021) were heavy browning, milky patterns, and the oxidation of the metallisation grid. In particular, these defects seemed to become severe after 20 years of operation. The comprehensive review by Jordan et al. (2017) concluded that older PV systems suffer mostly from EVA discoloration, while new PV systems installed within the last 10 years are especially prone to hot spots.

The aforementioned findings reflect the unpredictability of ageing processes. The situation is further complicated by the fact that ageing is often invisible or at least difficult to quantify. Although effects like discoloration, detachment effects, glass cracks, and burned cells can be visually observed, many others cannot, such as defects in electrical connections, shunting, microcracks, and p-n junction degradation. The need to detect and quantify ageing reliably emphasises the need to use more sophisticated tools, such as electrical measurements of PV modules, for condition monitoring and diagnosis. (Manganiello et al., 2015.)

2.4 Condition monitoring of photovoltaic systems

Condition monitoring needs related to PV power systems can be divided between the alternating (AC) and direct current (DC) sides. Focusing on the latter, the most common condition monitoring approaches are briefly reviewed here. Fitting the scope of this thesis, the condition monitoring methodology based on the measured *I-U* curves is highlighted. *I-U* curve-based condition monitoring and diagnosis is further divided into offline and online approaches. Of these two categories, online condition monitoring is discussed in more detail because of its greater practical applicability. Specific attention is paid to limiting the measured region of a *I-U* curve; a related literature review is also provided to emphasise the importance of the study conducted in the present thesis. Finally, the choice of measurement region of the *I-U* curve is discussed from the viewpoint of ageing detection.

Condition monitoring performed for a PV system is necessary for both the AC and DC sides of the system, the inverter acting as the watershed between them.

The AC side needs to be monitored because of power quality issues, possible interruptions in electricity production, and requirements set by standards related to the grid connection of the PV system. In turn, DC-side condition monitoring is needed to find defective PV modules, perform efficiency calculations, and detect different development trends of the system in either short or long operating periods. In particular, a condition monitoring procedure developed for the AC side does not detect minor changes in the DC side as they are weakly reflected to the power output of the PV system. (Kala et al., 2020.) Hence, ageing detection should be performed on the DC side as well. In addition, the location of defective modules inside the PV system cannot be discovered from the AC side. Azizi et al. (2018) also noted that ageing does not cause significant changes in the total harmonic distortion (THD) on the AC side because the increase in series resistance restricts the fundamental and harmonic components of the current. (Kala et al., 2020.)

The leading condition monitoring methods for the DC side of PV systems are analyses of images or measured *I-U* curves. The most important methods used in image analysis are infrared thermographic (IRT) and electroluminescence (EL) imaging. Unlike IRT imaging, EL imaging cannot be performed during the normal operation of the PV system. However, the diagnostic results obtained by IRT are not as accurate as those obtained by EL imaging. The imaging methods are costly, especially the complex EL imaging. Hence their usage is economically feasible only for large PV systems. Most importantly, these methods provide mostly qualitative diagnostic results, so the degradation of PV modules cannot usually be quantified by these methods. These facts constitute certain limitations from the viewpoint of online condition monitoring. In turn, analysis of measured *I-U* curves is an attractive solution to these problems. The curves can be traced during the operation of the maximum power point tracking (MPPT) algorithm. In particular, the measurement of partial *I-U* curves does not interrupt the electricity supply. As a clear advantage, *I-U* curve tracing combined with single-diode model fitting enables quantitative analysis of degradation. (Ahmad et al., 2019.)

Condition monitoring and diagnosis approaches intended for PV systems based on measured *I-U* curves can be roughly divided into offline and online categories. Conventional offline techniques rely on the measurement of the entire *I-U* curve with its SC and OC ends. The availability of the entire *I-U* curve data for fitting enhances the accuracy of the fitted parameters and the reliability of the diagnosis. However, it requires the disconnection of the investigated PV module or array from the system, causing an interruption in the electricity production. To

address this issue, online condition monitoring approaches have been developed. Such techniques require only the measurement of a partial *I-U* curve in the vicinity of the MPP without reaching the extreme ends. Such measurements can be implemented during the normal operation of the PV system. Online condition monitoring approaches based on reduced *I-U* curve measurement data tend to suffer from lower accuracy and produce fewer diagnostic parameters than offline approaches. (Bastidas-Rodriguez et al., 2017a.)

In the spirit of this discussion, it is necessary to further develop online condition monitoring approaches for PV systems based on measured *I-U* curves. Such a successful approach must both reproduce the fitting parameters with sufficient accuracy and operate in close proximity to the MPP. However, finding the optimal trade-off is not obvious based on the existing knowledge.

Some light has been shed on this discussion by the previous research. Several authors have tested single-diode model fitting procedures for individual partial *I-U* curves as well. Lappalainen et al. (2020) used the partial *I-U* curve obtained by moving the voltage 3 V away from the MPP symmetrically on both sides. Consequently, the OC slope was decently reproduced, while the SC slope of the fitted curve suffered from clear overshoot. To obtain more balanced fitting throughout the *I-U* curve, the authors recommended setting a power limit with respect to MPP power (P_{MPP}). In this light, the fitting procedure was tested with a power limit of 90% of P_{MPP}. This choice led to an increase in the series resistance and decrease in the shunt resistance of the fitted curve. Hachana et al. (2013) constructed their partial *I-U* curves by selecting 30% of the measurement points closest to the MPP for fitting. Fitting to such partial curves at high irradiance conditions produced smaller series resistance values than fitting to entire curves. Tina et al. (2016) developed an analytical parameter identification procedure operating within the voltage limits of usual commercial inverters. As such, it requires the measurement of partial *I-U* curves within the range between U_{OC} and the lower voltage limit such as 60% of U_{OC}. The procedure was able to identify the single-diode model parameters well for irradiance values larger than 500 W/m^2.

As another approach, the use of some special points around the MPP has been considered for fitting. Garrigós et al. (2007) located four points around the MPP in variable positions and investigated the effect of such choices for fitting. The best fit quality was obtained by picking two points from both sides of the MPP. Blanes et al. (2012) and Toledo et al. (2012) chose six measurement points divided into two blocks around the MPP. It was observed in Toledo et al. (2012) that the proper performance of the fitting procedure requires that the voltage

separation of the points belonging to the same block must not exceed 5% of the first selected voltage point. Moreover, the separation between the central points of the blocks must not exceed 20% of the voltage of the central point of the first block. An issue to be observed was also the choice of voltage steps determining the density of the selected points: when such a step was set to 2% of U_{MPP}, the OC and SC ends exhibited a clear overshoot and a slight undershoot, respectively. The fit quality was improved by setting the voltage step to 2.5% of U_{MPP}, which caused only a slight overshoot and undershoot in the OC and SC ends, respectively. Toledo and Blanes (2016) used four arbitrary points on the *I-U* curve jointly with the slopes of the *I-U* curve at these points. The four points were selected differently for different tests. The presented method worked even when restricting the *I-U* curve in the vicinity of the MPP at voltage limits of about 2%-3% of U_{MPP}.

As can be deduced from the above, the different choices of the *I-U* curve measurement region used for single-diode model fitting provide different fitting results. Indeed, the fit quality in each region of the *I-U* curve as well as the reproduction accuracy of each parameter value are not equal but strongly depend on the choice of the *I-U* curve measurement region available for fitting. Hence, the final goal of the fitting must be considered when selecting the measurement region. Having the focus on ageing detection, the most important parameter is the series resistance. Spagnuolo et al. (2019a) emphasised the challenges faced in series resistance identification due to the noise in the *I-U* curve measurement data combined with the difficulty to measure U_{OC}. Indeed, Sera et al. (2011) remarked that the series resistance can be identified mainly from the OC slope of the measured *I-U* curve. Towards this end, the authors suggested selecting the measurement points up to 60%-75% of the maximum power point current (I_{MPP}) on the right side of the MPP. This principle was also adopted in the work by Petrone et al. (2017a), where the authors complemented the choice of the measurement region by using a 15% voltage reduction to the left of the MPP. Indeed, the authors observed such an offset to be sufficient to reproduce the almost linear high-voltage region of the *I-U* curve. As the result, their fitting procedure caused at most only 11% power losses of the P_{MPP}, yet maintaining a good fit quality.

Overall, all the mentioned works constructed partial *I-U* curves only by way of individual examples. The effect of the construction method of partial *I-U* curves on the fitting accuracy has not been systematically studied. To shed some light on this issue, Lappalainen et al. (2022a) constructed partial *I-U* curves using power limits which are certain percentages of P_{MPP}. However, the used dataset consisted

of only 20 curves, whence there are still no statistically plausible results obtained by using a larger dataset. In addition, no other *I-U* curve cutting principle, such as setting cutting limits based on U_{MPP} percentages, has been systematically studied. These issues are addressed in this thesis, as was done in (Kalliojärvi et al., 2022).

2.5 Degradation and ageing indicators

Degradation and ageing of PV modules can be quantified by investigating the PV module's electrical characteristics. Indeed, ageing changes the shape of the *I-U* curve (Manganiello et al, 2015). To distinguish between different degradation and ageing effects, using various indicators helps to identify their source and type. In the following, some widely used indicators from the literature are briefly reviewed. Following the scope of this thesis, only those indicators which are directly based on *I-U* curve measurements and single-diode models are considered here.

Firstly, the reduction in P_{MPP} is only an overall consequence of the weakened state of PV system health. As such, it does not reveal the type of degradation; more specific indicators are needed for that purpose. Indeed, P_{MPP} is a function of I_{SC}, $U_{OC,}$ and fill factor (*FF*). These three indicators provide more detailed information about the state of health of the PV system. (Quansah et al., 2017.)

Reduced I_{SC} levels may indicate the presence of discoloration of the EVA encapsulant, delamination, glass corrosion, LID, and other phenomena that diminish the transmittance of light. In turn, U_{OC} reduction may occur due to LID, PID, or a short-circuited bypass diode, among other reasons. Compared to I_{SC}, U_{OC} tends to exhibit much smaller decreases in the PV modules in practical PV fields (Ahmad et al., 2019; Hrelja et al., 2018, Kaplani, 2012; Lindroos and Savin, 2016; Ndiaye et al., 2014; Quansah and Adaramola, 2018).

The ratio $\gamma_U = U_{MPP}/U_{OC}$ is a degradation indicator affected by increments in series resistance. Higher series resistance levels yield lower γ_U values. For constant series resistance levels, γ_U decreases almost linearly with increasing irradiance and temperature. (Kalliojärvi-Viljakainen et al., 2019; Spagnuolo et al., 2019b). The variation of γ_U with respect to the operating conditions and stage of ageing of the PV module is relatively wide. Indeed, Spagnuolo et al. (2019b) reported γ_U values of 0.57-0.81, the values being around 0.70-0.75 for a non-degraded PV module at high irradiance conditions. Unfortunately, no explicit formulae have been validated yet for γ_U as a function of irradiance, temperature,

and series resistance. Obviously, the γ_U ratio depends on the PV module type as well. Wang et al. (2011) obtained γ_U levels of approximately 0.81, while Di Piazza et al. (2015) and Moballegh and Jiang (2014) summarised that the majority of commercial PV modules exhibit values of 0.75-0.80 and 0.70-0.80, respectively. Hence the experimental values for γ_U serve as a guideline for its correct magnitude.

The ratio $\gamma_I = I_{MPP}/I_{SC}$ is also affected by degradation due to increased series resistance. Indeed, higher R_s levels produce lower γ_I values. In addition, γ_I is a decreasing function of irradiance; in Spagnuolo et al. (2019b), the value varied in the range of 0.80-0.93. At high irradiance conditions, the value can be considered approximately constant (Bastidas-Rodriguez et al., 2017a). Sera (2010) suggested values of 0.91-0.92, while Spagnuolo et al. (2019b) and Wang et al. (2011) reported values around 0.90 and 0.93, respectively.

Fill factor *FF* is defined as the product of $\gamma_U\gamma_I$. It measures the squareness of the *I-U* curve, which is made less steep by degradation. In particular, this may be due to decreased shunt resistance (Carrero et al., 2021; Kebir et al., 2021; Rabii et al., 2003) or increased series resistance (Carrero et al., 2021; Sinha et al., 2016). However, Piliougine et al. (2021) pointed out that some studies detected no decrease in *FF* despite the degradation, while some others revealed considerable *FF* reduction. Obviously, *FF* is affected by operating conditions as well. As a rule of thumb, commercial PV modules have fill factors greater than 0.60 (Di Piazza et al., 2015).

Normalised fill factor (*NFF*) is defined as the ratio FF/FF_{STC}, where the denominator is calculated from the datasheet values at STC. Like *FF*, *NFF* is also sensitive to the detected MPP and thus does not characterise any specific type of fault or degradation. (Bastidas-Rodriguez et al., 2017a.) In particular, *NFF* is affected by operating conditions. In fact, it is a function of irradiance and temperature, and its behaviour depends on the type of PV module technology (Marion, 2002). Bastidas-Rodriguez et al. (2017a) observed that *NFF* behaves approximately linearly as a function of the ratio $I_{SC}/I_{SC,STC}$. An increase in R_s was reflected in a reduced slope of such a line, leading to smaller *NFF* values. They emphasised that since *NFF* acts inversely proportionally to the operating temperature of the PV module, degradation cannot be reliably detected by using *NFF* only.

Among the single-diode model parameters, series resistance is the most prominent indicator of ageing. Increments in R_s usually indicate corrosion and degradation of the metallic parts of the PV module or other bulk defects hindering the current flow. Singh et al. (2018) assessed different series resistance estimation

techniques for silicon-based PV modules. They highlighted that the series resistance identification technique depends on the model and equations used. Change in series resistance ΔR_s is also a direct indicator for ageing detection. ΔR_s can be evaluated as an average increment of fitted series resistance values (Kalliojärvi-Viljakainen et al., 2022; Lappalainen et al., 2022a; Piliougine et al., 2021). Sera and Teodorescu (2009) also provided a method to estimate changes in series resistance rather than the actual series resistance value. A specific approach to define ΔR_s is that presented by Bastidas-Rodriguez et al. (2017a). Therein, ΔR_s is defined as the ratio $\Delta U_{MPP}/I_{MPP}$. Indeed, changes in R_s mainly affect the U_{MPP} value, but their effect on I_{MPP} is negligible. Further, the authors normalised this indicator, denoted by $N\Delta R_s$, by dividing the ΔR_s value by the series resistance value of the non-degraded PV module. Such a choice enables the quantification of ageing. A technical issue to be considered is that fitted R_s values always deviate from each other to some extent. On the other hand, the nonuniform nature of ageing also causes dispersion in fitted R_s values: the levels of corrosion experienced by the modules in a PV system do not usually coincide (Piliougine et al., 2021).

Another single-diode model parameter related to PV module degradation is the shunt resistance, which is connected to shunting-type defects. In particular, a decrease in the R_h value can indicate an early stage of PID before the appearance of considerable power loss (Finsterle et al., 2021). However, the single-diode model is rather insensitive with respect to the R_h parameter, implying that two similar-looking *I-U* curves may have largely different R_h values (Rashel et al., 2016). Hence, it is not always obvious whether the shunt resistance values are exhibiting real variation; such is the case in Piliougine et al. (2021). Change in shunt resistance, denoted by ΔR_h, is defined as $U_{MPP}/\Delta I_{MPP}$ in (Bastidas-Rodriguez et al., 2017a). The choice is justified by the observation that R_h variation has an obvious effect on I_{MPP} but only a negligible effect on U_{MPP}. The normalised value of ΔR_h ($N\Delta R_h$) is obtained by dividing the ΔR_h value by the R_h value of a non-degraded PV module.

The serial-parallel ratio (*SPR*) is an indicator classifying PV modules into two categories according to whether the series resistance or the shunt resistance effect is dominant (Cannizzaro et al., 2014). However, the usage of *SPR* for classification of high-fill-factor PV modules may be problematic (Di Piazza et al., 2015; Petrone et al., 2017b). Piliougine et al. (2021) observed that *SPR* is not a good indicator for the identification of absolute series resistance value or a change of series resistance. However, the authors noted that it can be used as a discrete indicator of degradation.

In conclusion, none of the aforementioned indicators used individually, except series resistance, provide absolute answers describing the state of health of the PV module; instead, the joint use of the indicators gives a better view of the condition of the PV module. It is also evident that the operating conditions must be taken into account when using any of these indicators.

2.6 Current-voltage curve tracing

Experimental *I-U* curve measurements can be performed either by an inverter or by a specific measurement device called the *I-U* curve tracer. The implementations of these two alternatives differ significantly from each other. Inverters are designed for online operation, but *I-U* curve tracers are usually exploited offline (Zhu and Xiao, 2020). By their hardware properties, most PV string inverters could be used to track at least partial *I-U* curves if only such functions were implemented in their control software (Spataru et al., 2015). Instead, *I-U* curve tracers are designed to measure entire *I-U* curves. Only the operation of *I-U* curve tracers falls within the scope of this thesis and is discussed in the remainder of this section.

I-U curve tracing is performed by making the tracer act as a dynamic load between the PV output terminals. In all commercial *I-U* curve tracers, the adjustment of a dynamic load controls the PV output current (voltage), whence the voltage (current) also becomes simultaneously regulated (Pereira et al., 2021; Zhu and Xiao, 2020).

The dynamic load action of an *I-U* curve tracer can be implemented via different methods (Durán et al., 2008a; Zhu and Xiao, 2020), the most used methods relying on resistive load, capacitive load, electronic load, or a DC-DC converter. The resistive load approach is the simplest method to implement the tracing system. However, it has some major limitations. Firstly, Zhu and Xiao (2020) remarked that a passive resistor bank tends to be too bulky. Secondly, the range of resistors limits the allowed measurement range. In particular, the distribution of the measurement points along the *I-U* curve is uneven (Zhu and Xiao, 2020). Indeed, as stated by Campos et al. (2018), there exists no variable resistor component with an ohmic range from zero to infinity. The stepwise behaviour of the resistor connections leads to the appearance of a large gap in the measurement points between the MPP and OC points, which increases with the increasing number of PV modules (Pereira et al., 2021; Zhu and Xiao, 2020). In

addition, Zhu and Xiao (2020) reported difficulties in reaching the OC point. Such issues might become real problems in large PV systems.

The capacitive load method is the most common principle in commercial *I-U* curve tracers (Pereira et al., 2021; Zhu and Xiao, 2020). Therein, a large capacitor is exploited as the dynamic load (Durán et al., 2008a; Zhu and Xiao, 2020). The capacitor is charged during the measurement sweep. The charging makes the current of the measurement circuit decrease and the voltage increase, which in turn produces the *I-U* curve from SC to OC (Zhu and Xiao, 2020). The method is simple, and the measurement time is short. In addition, the capacitive load methodology can be utilised to track the global MPP by measuring the partial power-voltage (*P-U*) curve with an auxiliary external capacitor (Spertino et al., 2015). The constraints of the capacitive load method mainly concern the sizing of the capacitors. Obtaining a sufficient measurement range in large-scale PV systems requires high capacitance, a wide voltage range, and high inrush current tolerance (Zhu and Xiao, 2020). On the other hand, Mahmoud (2006) and Durán et al. (2008a) highlighted that the usage of low capacitance components is mandatory to reach a short measurement time. Pereira et al. (2021) summarised that the measurement time depends largely on the PV system and the behaviour of the capacitors under charging. Durán et al. (2008a) noted that the accurate acquisition of *I-U* curves requires the usage of high-quality capacitors having low equivalent series resistance (ESR) and small losses. Meeting such a requirement obviously increases the costs. From the point of possible online measurements, a new measurement can be started only after the discharge of the capacitor is fully over, whence *I-U* curves cannot be measured partially (Durán et al., 2008a).

Compared to the previously described *I-U* curve tracing methods, the electronic load method is preferred due to its fastness, smoothness, and accuracy (Willoughby and Osinowo, 2018; Zhu and Xiao, 2020). Tracers based on the electronic load method use transistors as the dynamic load. The most common choices for this purpose are metal-oxide-semiconductor field-effect transistors (MOSFETs), but bipolar junction transistors (BJTs) or insulated gate bipolar transistors (IGBTs) are also used. The PV output current is controlled by regulating the transistor gate-source voltage U_{GS} (MOSFET, IGBT) or current (BJT). This modulates the ON-state resistance between the drain and source of the transistor, thus performing the dynamic load action (Zhu and Xiao, 2020; Pereira et al., 2021). The gate-source voltage signal in MOSFETs and IGBTs is easier to generate than the gate-source current signal in BJTs (Zhu and Xiao, 2020). The gate-source voltage (current) signal controls the drain current (I_D), which equals the

PV current. The obtained *I-U* measurement points are therefore determined by the intersection points of the PV module *I-U* curve and the I_D-U_{DS} curve of the transistor, where U_{DS} is the drain-source voltage (Zhu and Xiao, 2020). The current-ramp-based measurement results in the reproduction of the measured *I-U* points with linear spacing in the high-voltage region, where I_D varies almost linearly with U_{DS} (Zhu and Xiao, 2020). In contrast, the flatness of the *I-U* curve of a PV module with respect to voltage in the SC and MPP regions makes the PV output voltage sensitive to small variations in U_{GS}. This forces the measurement points to move too fast in the SC region. (Leite et al., 2012; Zhu and Xiao, 2020.)

Finally, DC-DC converters can be used for *I-U* curve tracing in their continuous conduction mode (CCM), in which condition the current through the inductor is continuous (Durán et al., 2008b). The dynamic load action is performed by regulating the duty cycle, which allows for the emulation of impedance values between zero and infinity and the consequent formation of an entire *I-U* curve (Durán et al., 2008b; Pereira et al., 2021). At this point, not all DC-DC converter topologies are suitable for *I-U* curve tracing because of their inability to measure the entire *I-U* curve. Indeed, a boost converter cannot reach the values near the OC point as this would require the emulation of impedances larger than the inductor resistance, whereas a buck converter fails to measure the values near the SC point, as the capacity to emulate impedances smaller than the inductor resistance is missing. Consequently, a buck-boost derived converter serves as a solution. (Enrique et al., 2005; Durán et al., 2008b; Zhu and Xiao, 2020.) However, as shown in (Zhu, 2018), the distribution of measurement points along the entire *I-U* curve tends to be uneven; although the adaptive *I-U* curve tracing developed in (Zhu, 2018) enables the dense acquisition of points in the MPP region, there are only a few points in other regions of the *I-U* curve. In addition, the high-frequency power switching causes undesired ripple in the output voltage and current and causes the risk of producing noisy measurement data (Zhu and Xiao, 2020; Pereira et al., 2021). Compared to the other *I-U* curve tracing methods, the advantages of the DC-DC converter method are its high efficiency, low cost, short measurement time, good accuracy, and the flexible possibility to modify the measurement sweep direction and speed as well as the measured part of the *I-U* curve (Durán et al., 2008a; Pereira et al., 2021).

The uneven distribution of measurement points on the obtained *I-U* curve produced by all the described *I-U* curve tracing methods is an obvious limitation when fitting a mathematical model to the measured *I-U* data. Indeed, an excellent fit quality is achieved in the regions of the *I-U* curve with densely appearing

measurement points, whereas the regions with sparse points suffer from lower fit quality (Zdanowicz, 1994). One solution for such a problem is proposed by Vega et al. (2019). Their *I-U* curve tracer design is an electronic load tracer with a specific double-sweep property. Therein, the high-voltage and high-current regions are divided into a fixed number of equidistant current and voltage intervals, respectively, which enables the even distribution of the measurement points. However, the developed tracer is unfortunately as yet a prototype. Another possible solution to mitigate the measurement point spacing problem in the case of electronic load tracers is to utilise control circuits to adjust the MOSFET operation (Zhu and Xiao, 2020). However, these solutions are not universal and applicable to all kinds of *I-U* curve tracer designs. This renders the need to develop a generic pre-processing procedure for the *I-U* curve measurement data. To address this issue, the development of such a procedure is presented in this thesis (Kalliojärvi-Viljakainen et al., 2020a).

3 ELECTRICAL MODEL OF PHOTOVOLTAIC SYSTEMS

3.1 Electrical model of photovoltaic module

This section is devoted to the mathematical modelling of a PV system, be it an individual PV cell, module, or larger unit. Firstly, the mathematical double-diode and single-diode models describing the operation of such a system are represented. Secondly, the consequent formation of the *I-U* curve providing the corresponding graphical presentation for the PV system is discussed. Thirdly, the notions of the diode models and the plotted *I-U* curve are tied together by explaining the relation of each of the model parameters to the graphical *I-U* curve. Finally, some general relevant aspects related to parameter identification are highlighted. This section is mainly based on the books Häberlin (2012) and Luque and Hegedus (2003).

The complex process concerning the operation of a PV cell described in Section 2.2 can be modelled via a set of partial differential equations called the semiconductor equations. The actual exact solution is very complicated and thus non-illustrative. However, the complexity of these equations can be mitigated by making certain simplifying assumptions. Firstly, the front and back contacts of the PV cell are assumed to be ideal ohmic contacts. Secondly, the material is assumed to be subject to uniform doping. Thirdly, the steady-state operation of the PV cell is assumed. Fourthly, the drift current of minority carriers, i.e., holes in the n-type and electrons in the p-type material, can be neglected with respect to the diffusion current of these carriers in the quasi-neutral regions.

Such a simplification of the semiconductor equations leads to a pair of differential equations known as the minority-carrier diffusion equations. Indeed, the behaviour of minority carriers determines the behaviour of the PV cell. Basically, the minority-carrier diffusion equations state that the diffusion current of minority carriers summed up with the optical generation rate of current carriers equals the recombination rate of the electron-hole pairs. The solution set in the presence of the boundary constraints given by the above simplifications is the *I-U*

curve of the PV system. Its equation is provided in its initial form for an ideal PV cell

$$I = I_{\mathrm{SC}} - I_{\mathrm{o1}}\left(e^{\frac{qU}{kT}} - 1\right) - I_{\mathrm{o2}}\left(e^{\frac{qU}{2kT}} - 1\right). \tag{1}$$

Equation (1) represents the PV cell output current I as a function of the output voltage U. It can be visualised via a simple equivalent circuit. Firstly, there is an ideal current source corresponding to the short-circuit (SC) current (I_{SC}) of the PV cell. Indeed, it follows from the ideality of the model that all the produced electron-hole pairs are available for the PV output current after the subtraction of the two diode currents appearing in (1). The two forward-biased diodes connected in parallel describe diode properties of the PV cell. The first and second diode terms account for the diode currents in the quasi-neutral and depletion regions, respectively. Therein, I_{o1} and I_{o2} are the respective dark saturation currents arising from the recombination occurring in these regions. The appearance of constants 1 and 2 in the denominators of the two exponential terms indicate the strong nonlinearity of the *I-U* curve. Moreover, k is the Boltzmann constant, q the electron charge, and T the PV cell operating temperature. Equation (1) is called the ideal double-diode model of PV cells. The other more practical electrical models of a PV cell originate from it.

Indeed, the operation of a practical PV cell differs from that of an ideal PV cell. Namely, there occur different loss mechanisms in the PV cells causing ohmic losses to the PV cell output. Some of these loss mechanisms can be viewed as series-type and some as shunting-type when introduced into the equivalent circuit. Hence, equation (1) is corrected by inserting series and shunt resistance parameters R_{s} and R_{h} to model such effects. The series resistance R_{s} originates from sources such as the resistances of the quasi-neutral regions, the lateral current through the quasi-neutral region of the more heavily doped n-type material from well-conditioned regions to those suffering from weaker condition, and the resistance of metal contacts like solder bonds, cell interconnect busbars and the metallisation grid as well as from their contact with the semiconducting material (van Dyk and Meyer, 2004; Hrelja et al., 2018; Meier and Schroder, 1984; Würfel et al., 2007). The shunt resistance R_{h} originates from non-idealities on the PV cell surface, impurities near the p-n junction, damage to the crystal structure, and other factors causing leakage currents across the p-n junction or the edge of the PV cell and partial shorting (Hrelja et al., 2018; van Dyk and Meyer, 2004). Both parasitic resistances limit the current output of the PV cell. Consequently, the current

source parameter I_{SC} must be replaced with another parameter to distinguish between the largest possible practical current output and the ideal current due to the generation of electron-hole pairs in the PV cell. For this purpose, the parameter photocurrent I_{ph} is used. The resulting model (2) is called the (non-ideal) double-diode model of a PV cell

$$I=I_{\mathrm{ph}}-I_{\mathrm{o1}}\left(e^{\frac{q(U+IR_s)}{kT}}-1\right)-I_{\mathrm{o2}}\left(e^{\frac{q(U+IR_s)}{2kT}}-1\right)-\frac{U+IR_{\mathrm{s}}}{R_{\mathrm{h}}}. \tag{2}$$

The double-diode model (2) is characterised by high accuracy, but unfortunately also by high computational complexity due to its implicit nature and large number of parameters. However, (2) can be simplified by observing that the recombination mechanism in the quasi-neutral regions dominates that occurring in the depletion region. This leads to maintaining only one exponential term, replacing the two original factors 1 and 2 with a suitable trade-off between them. The resulting factor is denoted by the ideality factor A. Such a simplification leads to the PV cell single-diode model equation

$$I=I_{\mathrm{ph}}-I_{\mathrm{o}}\left(e^{\frac{q(U+IR_s)}{AkT}}-1\right)-\frac{U+IR_s}{R_{\mathrm{h}}}. \tag{3}$$

The particular choice of an electrical model depends on the practical application. In some cases, the single-diode model is not sufficiently accurate, while some cases can be treated by using a much simpler model. For the purposes of the present work, the single-diode model is observed to be sufficiently accurate and useful because of its computational simplicity.

Equation (3) can be scaled to account for larger PV units such as PV modules, strings, or even entire arrays (Petrone et al., 2017b). The basic PV unit used in this thesis is an individual PV module, whence the single-diode model of a PV module

$$I=I_{\mathrm{ph}}-I_{\mathrm{o}}\left(e^{\frac{U+IR_{\mathrm{s}}}{AU_T}}-1\right)-\frac{U+IR_s}{R_{\mathrm{h}}} \tag{4}$$

is used throughout this thesis. It uses the notation $U_T = N_s kT/q$ for the thermal voltage of the PV module, where N_s is the number of PV cells connected in series in the module.

Obviously, any *I-U* curve can be characterised by the five single-diode model parameters (I_{ph}, I_o, A, R_s, R_h) of (4). Each of these has its impact on the unique shape of an individual *I-U* curve, which can be best understood by considering the practical nature and physical meaning of the parameter. The photocurrent I_{ph} determines the current source capability of the PV device in the ideal situation and is only slightly larger than I_{SC}. Hence, these two quantities are often considered equal (Dittrich, 2015). The saturation current I_o is negligibly small compared to I_{ph}. The magnitude of I_o affects the location of the exponential curvature of the *I-U* curve. The ideality factor A regulates the smoothness of the exponential curvature around the MPP and is essentially a parameter that describes the internal operation of the PV cell. (Petrone et al., 2017b.) The series and shunt resistances R_s and R_h affect the slopes of the *I-U* curve on the high-current and high-voltage regions of the *I-U* curve, respectively. In practice, the shunt resistance has large ohmic values, whereas the magnitude of the series resistance is usually fractions of **Ω**. An increase in series resistance causes a drop in the MPP voltage, while a decrease in the shunt resistance reduces the MPP current (Hrelja et al., 2018, Petrone et al., 2017b).

The importance of the model parameters lies in the mathematical analysis and diagnosis of the PV cell. Indeed, the parameter values can provide valuable information on the PV cell's condition. Unfortunately, these parameters cannot be directly measured but must be identified from a measured *I-U* curve via some mathematical procedure. The literature acknowledges a wide variety of single-diode model parameter identification approaches. Regardless of the clearly distinct effects of individual single-diode model parameters on the shape of the *I-U* curve, the parameters must be identified as a whole. They are strongly interconnected, so that a change in one parameter also affects the others. The issues related to parameter identification are discussed later in Section 3.3.

3.2 Effect of operating conditions on photovoltaic system electrical characteristics

The electrical performance of a PV system is significantly affected by the irradiance G it receives and its temperature T. Indeed, the electrical characteristics such as the MPP voltage and current, OC voltage and SC current provided by the PV system are altered along with the operating conditions. Such changes affect the shape and

location of the obtained *I-U* curve in the coordinate plane. Consequently, the single-diode model parameters identified from the *I-U* curve are affected as well.

To mitigate the effect of varying operating conditions on the electrical and single-diode model parameters, specific formulae for converting the parameters from one operating condition to another have been presented in the literature. Generally, a certain set of conversion formulae is assigned to a specific model depending on the author. A comparison of conversion methods of PV module characteristics can be found in Anani and Ibrahim (2020), for instance. To avoid confusion, only the formulae used in this thesis are presented in this section.

The single-diode model parameter identification procedure developed for this thesis utilises the conversion of two electrical quantities, namely the SC current I_{SC} and the OC voltage U_{OC} of the PV module. I_{SC} is directly proportional to irradiance, since the photon flux arriving at the PV module increases linearly with increasing irradiance. In particular, linear growth concerns the number of photons possessing sufficient energy to overcome the bandgap. These photons become absorbed in the PV cell and generate the electron-hole pairs causing the current flow through the PV cell. (Petrone et al., 2017b.)

In contrast to the irradiance effect, the effect of the temperature on I_{SC} is only minute, being an outcome of two opposite temperature effects. On one hand, the increasing temperature narrows the bandgap. This allows more photons to generate electron-hole pairs, which increases the SC current. On the other hand, the diffusion length and lifetime of electrons and holes as charge carriers decrease with increasing temperature. Hence, the recombination losses increase, which reduces the SC current. The firstly mentioned effect is dominant. It follows that the joint effect of temperature on I_{SC} is positive. (Petrone et al., 2017b.) The dependence of I_{SC} on the operating conditions is obtained in this work as in De Soto et al. (2006) by

$$I_{SC} = \frac{G}{G_{STC}}(I_{SC,STC} + K_I(T\text{-}T_{STC})), \tag{5}$$

where $I_{SC,STC}$, G_{STC} and T_{STC} are the STC values of SC current, irradiance, and temperature, and K_I is the temperature coefficient of SC current at STC.

The OC voltage decreases linearly with increasing temperature because of the narrowing of the bandgap. On the other hand, irradiance affects U_{OC} in a logarithmic manner. Indeed, the recombination of electrons and holes accelerates nonlinearly as the irradiance decreases, especially at low irradiance levels. The

dependence of OC voltage on the operating conditions is provided as in Kratochvil et al. (2004) by

$$U_{\mathrm{OC}}=U_{\mathrm{OC,STC}}+K_U(T-T_{\mathrm{STC}})+AU_T\ln(G_{\mathrm{eff}}), \tag{6}$$

where $U_{\mathrm{OC,STC}}$ is the OC voltage at STC, K_{U} the temperature coefficient of the OC voltage at STC, and G_{eff} the efficient irradiance, which can be calculated as in (Kratochvil et al. 2004) via

$$G_{\mathrm{eff}}=\frac{I_{\mathrm{SC}}}{I_{\mathrm{SC,STC}}+K_I(T-T_{\mathrm{STC}})}. \tag{7}$$

Accordingly, irradiance has a positive linear effect on the PV system's output power. In contrast, the operating temperature has a negative linear impact on the power output of the PV system. (Kratochvil et al., 2004; Skoplaki and Palyvos, 2009.)

The single-diode model parameter conversion formulae presented by De Soto et al. (2006) and Schroder (1998) are adopted in this thesis. Hence, the ideality factor A and series resistance R_{s} are considered invariant from the operating conditions, i.e.,

$$A = A_{\mathrm{STC}} \tag{8}$$

and

$$R_{\mathrm{s}}=R_{\mathrm{s,STC}}, \tag{9}$$

where A_{STC} and $R_{\mathrm{s,STC}}$ are the STC values for the ideality factor and series resistance, respectively. However, the shunt resistance R_{h} is considered to be inversely proportional to irradiance (Schroder, 1998), i.e.,

$$R_{\mathrm{h}}=\frac{G_{\mathrm{STC}}}{G}R_{\mathrm{h,STC}}, \tag{10}$$

where $R_{\mathrm{h,STC}}$ is the STC value of shunt resistance. The dependence of the photocurrent I_{ph} on the operating conditions is modelled via

$$I_{\mathrm{ph}} = \frac{G}{G_{\mathrm{STC}}}(I_{\mathrm{ph,STC}} + K_I(T\text{-}T_{\mathrm{STC}})), \tag{11}$$

where $I_{\mathrm{ph,STC}}$ is the photocurrent at STC.

The saturation current I_o has a strong positive dependence on the PV module's operating temperature (De Soto et al., 2006) and has been found to have only a minor, negligible, or unclear dependence on the irradiance depending on the used model (Ruschel et al., 2021). The conversion of I_o has not been considered in this thesis, because it has minor diagnostic value in practice.

It should be noted that despite the existence of the conversion formulae, operating conditions cannot be neglected in the analysis. As a simplification of the double-diode model, the single-diode model performs improperly under low irradiance conditions (Chaibi et al., 2019). However, this well-known limitation can be simply overcome by analysing the single-diode model parameters at high irradiance levels (Bastidas-Rodriguez et al., 2017a).

3.3 Parameter identification from measured current-voltage curves

Single-diode model parameters cannot be directly measured from a PV module but must be identified via some mathematical procedure from its *I-U* curve instead. The identification of single-diode model parameters is not a trivial task because of the nonlinear and implicit nature of the single-diode model equation. Jointly with these properties, the parameters are of very different orders of magnitude, which makes finding the correct solution yet more complicated (Bastidas-Rodriguez et al., 2017b). Indeed, solving the single-diode model equation is a non-convex optimisation problem with multiple local minima, i.e., the solution is not unique but there may be several sets of parameters that satisfy the equation. (Laudani et al., 2014; Rhouma et al., 2017.) The risk of failing to find the correct parameters increases when the number of parameters to be identified is large (Chin and Salam, 2019; Humada et al., 2020; Laudani et al., 2014).

Single-diode model parameter identification relies on fitting the model to empirical data. Fitting is an optimisation process that aims to minimise the difference between the theoretical model and empirical data. The fitted single-diode model equation can be expressed in either an implicit or explicit form. The different optimisation techniques used in single-diode model fitting can be roughly divided into three main categories. Iterative approaches utilise numerical

techniques to find the parameters. Analytical approaches provide a symbolic or analytical solution directly without iterations. Stochastic approaches employ metaheuristic algorithms to fit the mathematical model to empirical data. Each of these techniques has its advantages and disadvantages. Iterative approaches exhibit good accuracy. However, they require a proper initial guess solution in order to converge towards the correct solution. In addition, their computational cost is high. Analytical approaches are often more straightforward to implement and have a lower computational cost. However, the simplicity of such procedures reduces the accuracy of the results and makes the identification procedure prone to noise. Stochastic algorithms are usually accurate and capable of finding the correct solution. Naturally, this occurs at the expense of computational cost. From the point of view of developing the fitting procedure, the correct performance of fitting requires that the problem-specific control parameters are properly adjusted and the consistency issues arising from the variety of candidate solutions are overcome. (Batzelis, 2019; Chin and Salam, 2019; Jordehi, 2016.)

Every such parameter identification category has gained wide attention in the literature. However, almost each of the proposed approaches can only identify the single-diode model parameters without providing any information about irradiance and temperature of the operating conditions. Such approaches are insufficient for practical condition monitoring and diagnostic purposes, as the identified parameter values depend on the operating conditions. The lack of information on the operating conditions makes a reliable diagnosis based on the *I-U* curves measured from the PV system virtually impossible, unless the operating conditions are identified jointly with the single-diode model parameters.

To participate in this discussion, this thesis introduces a novel single-diode model parameter identification approach that simultaneously provides information on the PV module's operating irradiance and temperature (Kalliojärvi-Viljakainen et al., 2022). In addition, there exist only a few published studies such as Lappalainen et al. (2020) and Lappalainen et al. (2022a) that introduce single-diode model fitting procedures with the capability of identifying the operating conditions as well. These three approaches differ from each other by the following properties.

The presentation of the single-diode model is explicit in Lappalainen et al. (2020) and implicit in Kalliojärvi-Viljakainen et al. (2022) and Lappalainen et al. (2022a). The work of Lappalainen et al. (2020) relies on the usage of the popular Lambert *W* function (Ghani and Duke, 2011; Accarino et al., 2013). Such a choice converts the implicit single-diode model equation into an explicit form. However, the implementation of the Lambert *W* function is practically based on

approximations (Batzelis et al., 2020; Lappalainen et al., 2022a). The different methods of implementing the Lambert *W* function in PV cell modelling were evaluated in Batzelis et al. (2020). It was concluded that the most accurate Lambert *W* function implementation (i.e., the MATLAB function *lambertw.m*) has the largest computational cost. In this light, a single-diode model parameter identification based on the implicit equation is recommended when possible. In the studies of Lappalainen et al. (2022a) and Kalliojärvi-Viljakainen et al. (2022), the implicit form of the single-diode model equation has been used to maintain the accuracy.

The approaches (Kalliojärvi-Viljakainen et al., 2022; Lappalainen et al., 2020; Lappalainen et al., 2022a) differ also in their choice of auxiliary equations to set up the single-diode model. The expression for saturation current I_o is based in Lappalainen et al. (2020) and Lappalainen et al. (2022a) on bandgap- and temperature-based expression as in De Soto et al. (2006). Such an approach introduces extra coefficients which must be calculated before fitting. In turn, Kalliojärvi-Viljakainen et al. (2022) employs the saturation current expression obtained from the single-diode model equation by using only one auxiliary equation. The small number of equations used in this case simplifies the calculation.

The third difference between the methods (Kalliojärvi-Viljakainen et al., 2022; Lappalainen et al., 2020; Lappalainen et al., 2022a) lies in the initial guess solution provided for the fitting algorithm, as the initial guess must be set for each output parameter directly produced by the fit. In Lappalainen et al. (2020) and Lappalainen et al. (2022a), the set of direct output parameters of the fit is $\{G, T, R_s, R_h\}$ and, therefore, the initial guess for the parameters of the first *I-U* curve of the dataset is $\{G_{STC}, T_{STC}, R_{s,STC}, R_{h,STC}\}$. In both works, the Lambert *W* function is utilised to calculate $R_{s,STC}$ and $R_{h,STC}$. The following *I-U* curves in the used dataset utilise the previous fitted values as the initial guess. However, the irradiance value may vary rapidly from curve to curve. In Kalliojärvi-Viljakainen et al. (2022), the set of direct output parameters of the fit is $\{I_{ph}, T, R_s, R_h\}$. The initial guess for the parameters of the first curve is $\{I_{MPP}/\gamma_I, T_{STC}, R_{s,STC}, R_{h,STC}\}$, where γ_I is an experimental approximation for the ratio I_{MPP}/I_{SC} calculated from the PV module's electrical characteristics at STC and hence assumed constant in the present study. Remarkably, the SC current of the *I-U* curve does not need to be measured, but can be provided via a reasonable approximation of γ_I. The initial guess for I_{ph} is calculated separately for each *I-U* curve in the dataset. Such a choice captures rapid irradiance variations more effectively than the use of the previously fitted I_{ph} value. The STC values for parasitic resistances are calculated by the fully iterative

procedure of Villalva et al. (2009). Hence no explicit approach has been utilised. The following curves after the first one in the dataset utilise the previously calculated values of T, $R_{s,}$ and R_h as the initial guess. Such a choice is justified because these parameters change slowly as environmental conditions change.

Finally, the choice of a suitable single-diode model fitting procedure depends on the situation. When the focus is on ageing and detection of series resistance, the Lambert W function fails to perform properly for highly degraded PV modules (Piliougine et al., 2021). Hence the usage of the implicit single-diode model equation is preferred for such purposes.

3.4 Developed single-diode model fitting procedure

The developed fitting procedure takes the measured I-U curves as its inputs. In addition, the values for $I_{SC,STC}$, $U_{OC,STC}$, $I_{MPP,STC}$, $U_{MPP,STC}$, K_I, K_U, N_s and A of the PV module are required. This makes the fitting procedure easily applicable in real-case PV systems: the electrical characteristics at STC are reported for any commercial PV module in its datasheet provided by the manufacturer. The fitting procedure returns the single-diode model parameters I_{ph}, I_o, R_s and R_h jointly with the operating irradiance G and temperature T as its outputs. This enables the interpretation of the fitted parameter values in relation to the operating conditions.

The simultaneous presence of all these six parameters of interest in the fitting equation might cause a fitting algorithm to be trapped in a local optimum instead of the correct solution with a physical meaning (Laudani et al., 2014). To prevent this, the set of parameters directly obtained from the fit is reduced to I_{ph}, T, R_s and R_h. The value of I_o is calculated inside the fitting objective function called by the *fit.m* function in MATLAB via the expression

$$I_o = \frac{I_{ph} - \frac{U_{OC}}{R_h}}{e^{\frac{U_{OC}}{AU_T}} - 1}, \tag{12}$$

which is obtained from (4) at OC. A successful estimation of I_o requires an accurate estimation of U_{OC}. Indeed, U_{OC} is not directly measured but calculated in a point-by-point manner inside the fitting objective function to adjust the fitting parameters. Such an approach also enables partial I-U curves to be analysed, leaving the extreme ends of the curves unmeasured. The estimate for U_{OC} inside (12) is provided by (6)-(7).

After the actual curve fitting, the SC current of the fitted curve is calculated as

$$I_{\mathrm{SC}} = \frac{I_{\mathrm{ph}}}{1 + \frac{R_{\mathrm{s}}}{R_{\mathrm{h}}}}, \tag{13}$$

and further the irradiance is calculated via

$$G = \frac{G_{\mathrm{STC}} I_{\mathrm{SC}}}{I_{\mathrm{SC,STC}} + K_I (T - T_{\mathrm{STC}})}. \tag{14}$$

Fig. 1 describes the entire parameter identification process for a set of measured *I-U* curves. The stopping criteria determined for the actual fitting algorithm are as follows. Suitable maximum numbers of iterations and objective function evaluations were found to be 3000 and 10000, respectively. The tolerances for the step size and differences in fitted parameter values between two iterations were both set to MATLAB's default values of 1e-6.

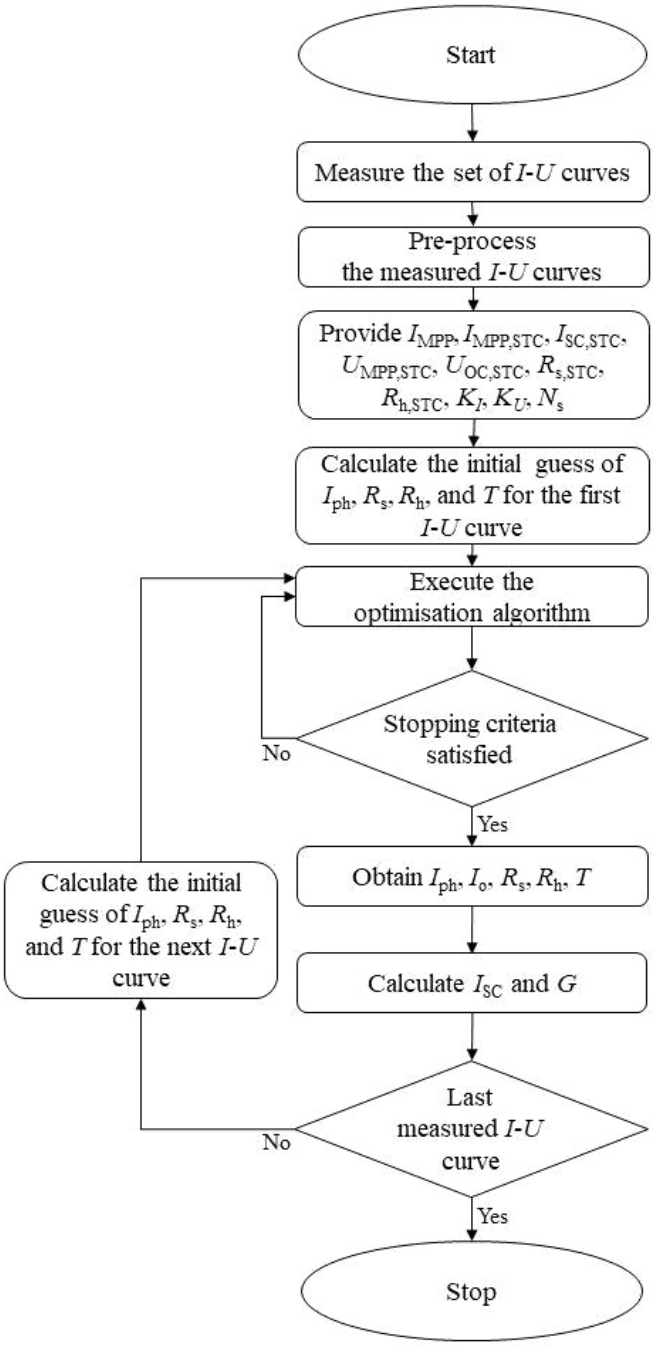

Figure 1. Flowchart of the parameter identification process.

4 MEASUREMENT DATA AND ITS PRE-PROCESSING

4.1 Measurement data

The measurement data used in this thesis was gathered from the TAU PV power research plant of Tampere University located on the rooftop of the Sähkötalo building on the Hervanta campus. The detailed configuration of the PV installation is described in Torres Lobera et al. (2013a). The PV power plant consists of 69 PV modules (NAPS NP190GK) fabricated of multi-crystalline silicon, the total nominal peak power being 13.1 kWp. An individual PV module follows the typical PV module structure consisting of 54 series-connected PV cells and is protected by three bypass diodes, each connected in antiparallel with a block of 18 cells. The PV modules are installed with a tilt angle of 45 degrees with respect to the horizon, facing nearly due south. (Torres Lobera et al., 2013a.)

The PV power plant has been equipped with climatic and electrical measurements. Ambient temperature and relative air humidity are measured by a HMP155 sensor (Vaisala). Wind speed and direction are registered by an ultrasonic WS425 sensor (Vaisala). Global irradiance is measured by a pyranometer CMP22 (Kipp & Zonen), and the diffuse component of irradiance is captured with a pyranometer CMP21 equipped with a shadow ring. In addition, a mesh of 24 pairs of SPLite2 and Pt100 sensors register the irradiance received by individual PV modules and their backplate temperature. The irradiance measurements are in good agreement with the actual irradiance received by the PV modules, the measurement accuracy having been discussed in Torres Lobera et al. (2013a). The backplate temperature measurements were observed to correlate closely with the actual PV cell temperatures (Torres Lobera et al., 2013b) and can thus be used as a reference for the PV cell temperature by taking into account the heat capacity of the PV module and other possible factors affecting the PV cell temperature. The sampling frequency of the climatic measurements is 10 Hz, which is sufficient to capture even the fastest climatic phenomena affecting power generation. The acquired

climatic measurements are stored in a SQL (Structured query language) database. (Torres Lobera et al., 2013a)

The electrical *I-U* curve measurements are implemented by an *I-U* curve tracer utilising eight parallel-connected IGBTs as the electronic load. The sampling frequency for the measured *I-U* curves has been set to 1 Hz.

The *I-U* curve data used in this thesis was measured from PV module 19. The corresponding irradiance and temperature values were measured with SPLite2 and Pt100 sensors connected to module 19. The choice of an individual module for analysis well met the need for the development and performance verification of the proposed *I-U* curve fitting procedure. It was experimentally observed in Lappalainen et al. (2020) that the values of SC current, OC voltage, and MPP current and voltage ($I_{SC,STC}$, $U_{OC,STC}$, $I_{MPP,STC}$, $U_{MPP,STC}$) of module 19 at STC differ slightly from their nominal datasheet values reported in Torres Lobera et al. (2013a). Therefore, their values had to be redetermined to ensure a reliable analysis. The exploited redetermination process is described in detail in the Appendix. Using the obtained values, the STC values for the parasitic resistances ($R_{s,STC}$, $R_{h,STC}$) were determined by exploiting the procedure of Villalva et al. (2009), the used MATLAB code having been initially presented in Mäki (2013). The temperature coefficients for SC current and OC voltage at STC (K_I, K_U) were obtained from the manufacturer datasheet. The ideality factor A was kept constant (Stornelli et al., 2019). The key parameters of PV module 19 at STC are provided in Table 1.

Table 1. The electrical characteristics of PV module 19 at STC.

Parameter	Value
$I_{SC,\,STC}$	8.72 A
$U_{OC,\,STC}$	32.8 V
$I_{MPP,\,STC}$	7.94 A
$U_{MPP,\,STC}$	22.9 V
$R_{h,\,STC}$	354 Ω
$R_{s,\,STC}$	0.768 Ω
K_I	0.0047 A/K
K_U	-0.124 V/K
A	1.1
N_s	54

The used measurement datasets are described in Table 2. Dataset A was used for testing the curve fitting procedure developed in this thesis in different

operating conditions. Therefore, it contains conditions of stable high irradiance and temperature, as well as sharp irradiance transitions with a significant drop in temperature. The stable high-irradiance part was thereafter separated into its own dataset B to analyse the model performance with partial *I-U* curves. Indeed, measurements made in low irradiance conditions are not meaningful for the goals of this thesis. Datasets C, D and E were used for the ageing analysis. All were measured under high irradiance conditions. Different stages of ageing were emulated by connecting different-sized resistors with additional series resistances ($R_{s,add}$) in series with PV module 19. In this way, it could be shown quantitatively that the used fitting procedure is able to identify the series resistance correctly. Datasets C, D and E were measured over less than two months, so real ageing effects did not have time to occur between measurements. This enabled the reliable quantification of series resistance increments.

Table 2. The used measurement datasets.

Dataset	$R_{s,add}$ (Ω)	Date	Start time	Length (s)
A	0.00	2020-08-25	12:57:26	3600
B	0.00	2020-08-25	12:57:26	2400
C	0.00	2020-08-25	12:57:26	1300
D	0.22	2020-07-18	11:06:02	1300
E	0.69	2020-07-31	12:16:39	1300

All the measured *I-U* curves share some common characteristics. Firstly, the direction of an *I-U* curve measurement sweep is from OC to SC, which was also strongly preferred in the earlier literature (Chayavanich et al., 2006). Indeed, using the opposite direction produces distortion in the measured *I-U* curves at high voltage values close to the MPP. As explained in Chayavanich et al. (2006), the reason for that is the charging and discharging current of the PV cell resultant capacitance consisting of the transition and diffusion capacitances appearing in the reduced AC equivalent circuit model of the PV module. However, this problem is mitigated by the appropriate measurement sweep direction.

Secondly, each *I-U* curve contains 4000 measurement points obtained by changing the system current step by step, resulting in current-voltage points at equal time intervals. The measurements were performed with a 100 ms ramp controlling the gate signal, and the actual duration of the measurement sweep was less than 40 ms. However, such a short ramp might be prone to circulation of current due to resonance inside the system. This may cause distortion on the

tracked *I-U* curves. Both current and voltage vectors suffer from unintentional abnormalities, similar observations having been made in Hao et al. (2021) and Nilsson (2014). In addition, approximately 80% of the measurement points are accumulated to the OC region of the *I-U* curve. In contrast to the densely located measurement points in the high-voltage region, there are fewer of them in the high-current region. Consequently, the over-weighted OC region becomes strongly emphasised in the single-diode model fitting. Such a superior fit quality in the OC region compromises the fit quality in the SC region (Zdanowicz, 1994).

The aforementioned data quality problems make it necessary to eliminate the abnormal measurement points as well as to redistribute the remaining measurement points before the actual fitting of the single-diode model. One possibility is to perform the fitting as soon as the most obvious abnormalities have been eliminated and try to improve the fit quality by issuing the Bisquare method jointly with the *fit*.m function in MATLAB. The Bisquare method minimises a weighted sum of squares, where the furthest points are given the least weights in fitting. However, using this method increases the computational time significantly. Several pre-processing procedures have been presented in the literature. These procedures can be roughly divided into those for eliminating abnormalities and those for redistributing the measurement data. Meng et al. (2023) smoothed the *I-U* curve data by applying a first-order Kalman filtering algorithm separately to the current and voltage measurement vectors of the *I-U* curve. Sun et al. (2019) smoothed the time series data of U_{MPP} and I_{MPP} by a physics-based filtering method. The algorithm divides the data into time intervals. The data of each interval is subject to fitting. The relative error of fitting is calculated point by point. Those points with an error of at least 50% are considered outliers and discarded. Thereafter, the algorithm examines the number of the remaining data points in the time interval. If the points are less than 80% of their original number, all the points in the interval are discarded. However, it should be noted that the authors did not apply the method for *I-U* curves. If the procedure were so applied, the use of time intervals might not provide a straightforward solution at least for the problem of the uneven weighting of measurement points between different parts of the *I-U* curve. Another approach, used in Lappalainen et al. (2022a), utilised the observation that the measured *I-U* curves contain several points with redundant voltage values. Points with similar voltage values were treated as a single point by averaging the corresponding current values. Although such a procedure reduced the unintentional weighting and was also adopted in Kalliojärvi-Viljakainen et al. (2022), it is not the most systematic, as the exact location of the remaining points

depends on the measured *I-U* curve. Lappalainen et al. (2021) smoothed the *I-U* curve measurement data as follows. The previously mentioned procedure (Lappalainen et al., 2022a) was applied first. Thereafter, the abnormal measurement points were removed by comparing the power of each measurement point to its neighbouring points. If the power difference to the neighbouring points was larger than 1.3 times the mean power difference of the previous and next nine measurement points, then the point was discarded as abnormal. Chen and Zhang (2021) redistributed the *I-U* curve measurement data by sampling data points by equidistant current intervals in the high-voltage region and equidistant voltage intervals in the high-current region. However, the number of points remaining on the *I-U* curve is based on a trial-and-error manner, hence varies from curve to curve.

In this light, a pre-processing procedure is needed to both remove abnormalities and mitigate the uneven weighting among the measurement points of the *I-U* curve. Towards this end, a pre-processing procedure for the raw *I-U* curve measurement data developed in Kalliojärvi-Viljakainen et al. (2020a) was exploited in this thesis. The developed pre-processing procedure has two steps: 1) elimination of abnormal measurement points, and 2) removal of measurement point weighting.

4.2 Elimination of abnormal measurement points

The proposed *I-U* curve pre-processing procedure is initiated by determining the maximum power point. Indeed, the MPP divides the *I-U* curve into high-current and high-voltage parts that need to be treated differently during the developed pre-processing procedure, so the MPP must be determined. The goal is to find the dominant MPP point among the noisy measurement data, because the maximum measured power value can be an abnormal measurement point caused by measurement error or noise.

For the MPP estimation, only the topmost part of the measured *P-U* curve is of interest. The investigated region is limited to an experimentally validated percentage of 95% of the maximum value of the measured power. Thereafter, the power distance of each *P-U* point to its adjacent points is determined. If the measured power of a point deviates from the power values of its adjacent points more than the standard deviation of all the measured power values of the limited interval, the point is considered an abnormal measurement point and discarded

from the set of possible maximum power point estimates. It should be noted that such a criterion for identifying abnormalities is rather loose compared to several other statistical criteria; it excludes only the most obvious measurement errors. However, the usage of this simple method is justified in the case of the sharply sawing nonlinear *P-U* measurement data. The exclusion of the largest measurement errors leaves behind less heterogeneous *P-U* data, which is further smoothed by applying moving average filtering with an interval of 20 points. Finally, the estimate for the MPP is retrieved from the smoothed *P-U* measurement data.

Fig. 2 illustrates the performance of the MPP estimation step. As can be seen, there is a clear difference between the measured and estimated MPP power. The estimation step is easy to implement as part of the pre-processing procedure. In addition, it has low computational burden, and its accuracy is sufficient for the *I-U* curve fitting purposes of the present work.

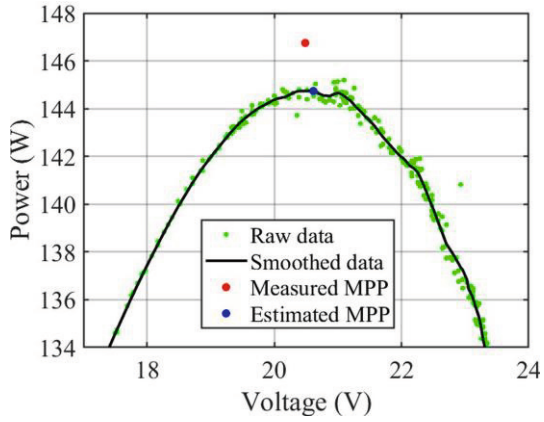

Figure 2. Estimation of MPP from the raw measured *P-U* data before the elimination of abnormal measurement points.

The MPP estimation is followed by the actual elimination of the abnormal measurement points, where the entire measured *I-U* curve is subjected to the developed sequential elimination algorithm (Kalliojärvi-Viljakainen et al., 2020a). Basically, the algorithm follows the dominant shape of the *I-U* curve by short piecewise linear approximations and evaluates the distance of measurement points from the fitted lines. Measurement points having the longest distance to the fitted line are regarded as abnormal, utilising the statistical interquartile range (IQR) method.

Initiating from the OC end of the raw measured *I-U* curve, the algorithm provides a progressive partition of the measurement points into short intervals of

appropriate lengths. The length of each interval is pre-determined and tied to the voltage value of the determined MPP. The interval lengths of piecewise linear approximations are experimentally adjusted so that they follow well the shape of the original measured *I-U* curve. Fig. 3 illustrates the division of the raw measured *I-U* curve into voltage regions, each having its specific length for the intervals. The lengths of intervals in different voltage regions of the *I-U* curve are reported in Table 3.

The voltage intervals partially overlap, so that the last 20% of the points of the previous interval provide the beginning of the next interval. This is to enhance the operation of the elimination algorithm. For any individual interval, the scanning of the interval is immediately followed by line fitting. The fitted lines are of the form $U = aI + b$ and $I = cU + d$ on the high-voltage and high-current regions of the *I-U* curve, respectively. These choices are justified as the independent variable on either side of the MPP is mainly responsible for the occurrence of the abnormalities. Indeed, abnormalities in the high-voltage region are mostly due to current offsets and vice versa. The elimination algorithm calculates the distance of every measurement point of the interval from the fitted line. When the calculated distance of a point from the fitted line exceeds the widely used statistical threshold of 1.5 times the IQR, the point is considered an abnormal measurement point and is removed. A detailed example illustrating the operation of the elimination algorithm is shown in Fig. 4.

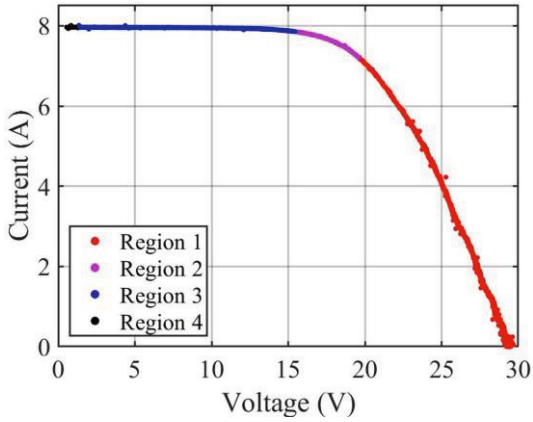

Figure 3. Division of the raw measured *I-U* curve into voltage regions for the elimination of abnormal measurement points.

Table 3. Division of the raw measured *I-U* curve into voltage regions for the elimination of abnormal measurement points.

Region	Voltage limits	Interval length
1	$0.8U_{MPP}$ - OC	$0.05U_{MPP}$
2	$0.5…0.8U_{MPP}$	$0.1U_{MPP}$
3	$0.2…0.5U_{MPP}$	$0.2U_{MPP}$
4	SC – $0.2U_{MPP}$	one interval

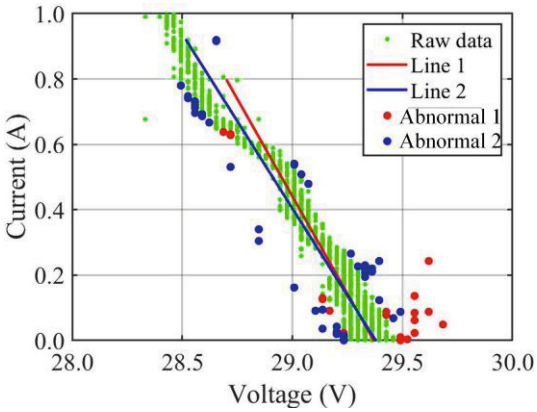

Figure 4. Elimination of abnormal measurement points illustrated by two successive steps at the beginning of the OC end of the *I-U* curve.

The elimination algorithm must be tested for *I-U* curves measured at high, medium, and low irradiance conditions, because the shape of the measured *I-U* curve changes with changing irradiance. Figs. 5-7 illustrate the excellent performance of the algorithm in such irradiance conditions. Remarkably, *I-U* curves measured in low irradiance conditions (Fig. 7) include more abnormalities than curves measured in high or medium irradiance conditions (Figs. 5 and 6) (Kalliojärvi-Viljakainen et al., 2020a). Using the measurement data provided by the *I-U* curve tracer, the algorithm finds 100-250 abnormal measurement points from high-irradiance curves and 100-300 abnormal measurement points from medium-irradiance curves. The corresponding figure for low irradiance curves is 100-450. (Kalliojärvi-Viljakainen et al., 2020a.) Such a difference is mainly explained by the measurement accuracy of the *I-U* curve tracer, its effect on the measurement results being amplified at low irradiance levels. Nonetheless, the presented numbers of eliminated abnormalities are not universal but depend on the used *I-U* curve measurement data. A significant result is that the elimination algorithm

retains the original shape of the measured *I-U* curve under all irradiance conditions. Consequently, the algorithm can be used to improve the quality of any measured *I-U* curve before curve fitting.

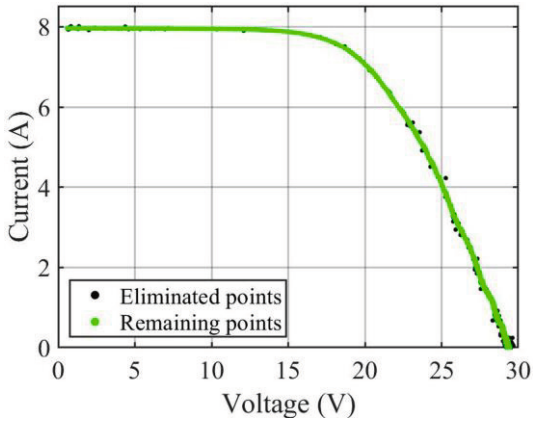

Figure 5. Raw *I-U* curve measured at high irradiance conditions (G = 1008 W/m²) before and after the elimination of abnormal measurement points.

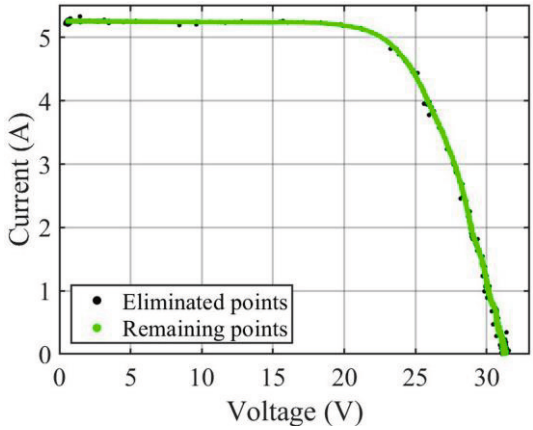

Figure 6. Raw *I-U* curve measured at medium irradiance conditions (G = 589 W/m²) before and after the elimination of abnormal measurement points.

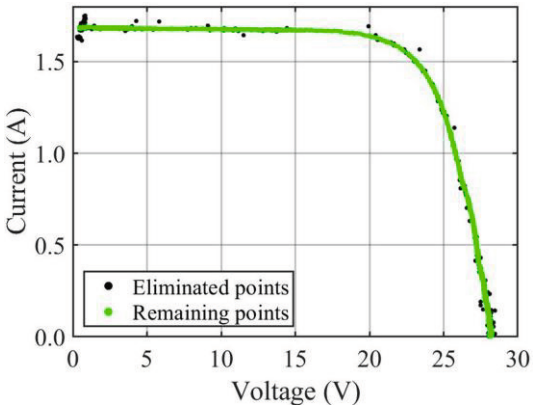

Figure 7. Raw *I-U* curve measured at low irradiance conditions (G = 176 W/m²) before and after the elimination of abnormal measurement points.

4.3 Removal of weighting from measurements

Unfortunately, the issue of the unintentional weighting of the measurement points still exists after the elimination of abnormal measurement points. To address this issue, a computationally systematic approach for the removal of the undesired weighting of measurement points is presented in Kalliojärvi-Viljakainen et al. (2020a). Therein, the *I-U* curve is first split into high-current and high-voltage regions, separated by the estimated MPP. Both regions are then divided into an equal number of short and evenly distributed intervals. In the spirit of Vega et al. (2019) and Wolf and Benda (2013), the even distribution of these intervals is reached by dividing the high-current region into equidistant voltage intervals and the high-voltage region into equidistant current intervals. Finally, the current and voltage values of each interval are averaged to form one current-voltage point representing the entire interval. The points obtained in this manner are called the representative points. The representative point approach is utilised in Kalliojärvi et al. (2022).

The choice of an appropriate number of representative points per an *I-U* curve is an important issue which must be addressed to guarantee successful fitting. Figs. 8-11 show the direct output parameters I_{ph}, R_h, R_s and T of the developed single-diode model fitting procedure described in Chapter 3 as a function of the number of the representative points used for fitting. The first 300 successive *I-U* curves of dataset A have been used for the analysis. Such a number of measured *I-*

U curves is expected to be sufficiently large to show the real behaviour of the fitted parameters, and sufficiently small to maintain stable operating conditions.

Fig. 8 shows that the fitted photocurrent values are stable when at least 40 representative points are used for fitting. A smaller number of representative points leads to difficulties capturing the MPP curvature correctly, whence the SC end of the fitted *I-U* curve clearly overshoots. This becomes visible as increased I_{ph} values.

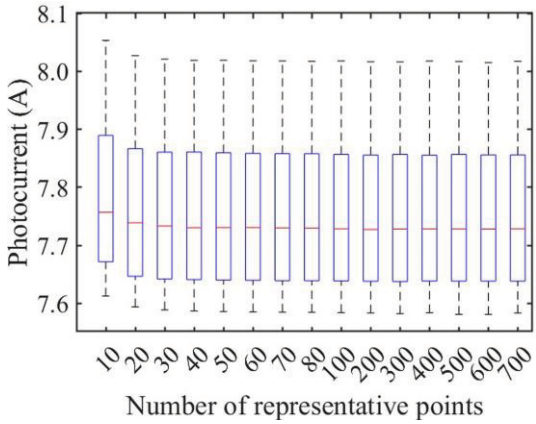

Figure 8. The fitted photocurrent values obtained from 300 successive *I-U* curves measured at stable high irradiance conditions as a function of the number of representative points used for fitting. The blue boxes represent the fitted values between the 25th and 75th percentiles, the red line is the median, and the dashed lines indicate the extreme data points.

Fig. 9 shows that the fitted shunt resistance values are not as stable as the fitted I_{ph} values when using a small number of representative points. Such a finding was expected, as the single-diode model is not particularly sensitive to the value of R_h. If only a few tens of representative points are used for the fitting, the obtained R_h values are too small, but settle when using a larger number of representative points. This behaviour follows again from the failure to repeat the curvature around the MPP; the overshooting I_{ph} values and the undershooting R_h values are directly linked to each other.

Fig. 10 shows that the fitted series resistance values are relatively stable when at least 100 representative points are used for fitting. Below that, the R_s values fluctuate somewhat, which is a natural consequence of the variations of I_{ph} and R_h parameters shown in Figs. 8-9.

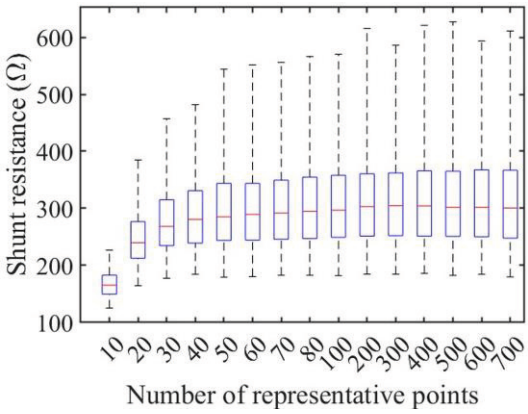

Figure 9. The fitted shunt resistance values obtained from 300 successive *I-U* curves measured at stable high irradiance conditions as a function of the number of representative points used for fitting. The blue boxes represent the fitted values between the 25th and 75th percentiles, the red line is the median, the dashed lines indicate the extreme data points.

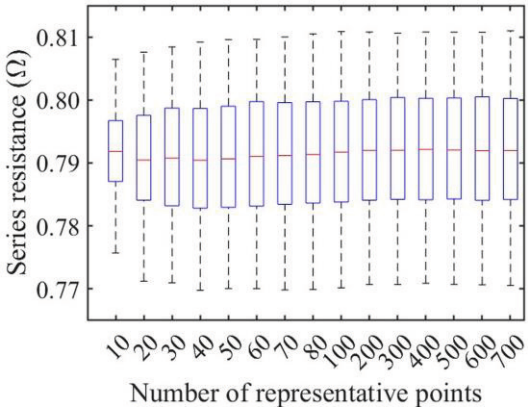

Figure 10. The fitted series resistance values obtained from 300 successive *I-U* curves measured at stable high irradiance conditions as a function of the number of representative points used for fitting. The blue boxes represent the fitted values between the 25th and 75th percentiles, the red line is the median, and the dashed lines indicate the extreme data points.

Fig. 11 shows that the fitted temperature stabilises quickly as the number of representative points increases. This follows from the correct repetition of the OC end of the *I-U* curve in fitting, even when using a small number of representative points.

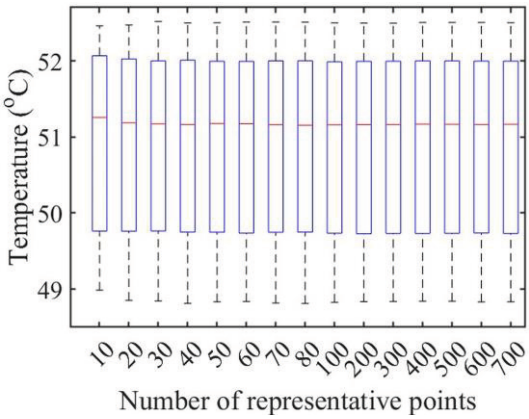

Figure 11. The fitted temperature values obtained from 300 successive *I-U* curves measured at stable high irradiance conditions as a function of the number of representative points used for fitting. The blue boxes represent the fitted values between the 25th and 75th percentiles, the red line is the median, and the dashed lines indicate the extreme data points.

In conclusion, 100-200 representative points seem to be enough for fitting the single-diode model reliably to *I-U* curves. However, if the single-diode model is fitted to partial *I-U* curves, a number of representative points closer to 100 is preferable to avoid high computational costs and exceeding the number of original measurement points. The last-mentioned issue is especially important when dealing with partial *I-U* curves measured in very close proximity to the MPP.

4.4 Generation of partial current-voltage curves

Since the online condition monitoring approaches based on the measured entire *I-U* curves significantly disturb the operation of the PV systems, the use of partial *I-U* curves is highly desirable. However, the measurement range of the *I-U* curve cannot be arbitrarily limited, as its choice certainly affects the overall quality of the fit and the accuracy of the parameters of the fitted single-diode model. A systematic investigation of such effects is thus needed. To address this issue, this thesis applies two easily applicable *I-U* curve cutting principles (Kalliojärvi et al., 2022), both of which limit the measurement range of the *I-U* curve to the vicinity of the MPP.

The first *I-U* curve cutting principle is based on the MPP power. The cutting points are defined as a certain percentage of the P_{MPP}. Points on the *I-U*

curve with a power higher than or equal to the power limit are taken into account when fitting. Fig. 12 shows an example of P_{MPP}-based cutting with a 50% cutting limit of P_{MPP}.

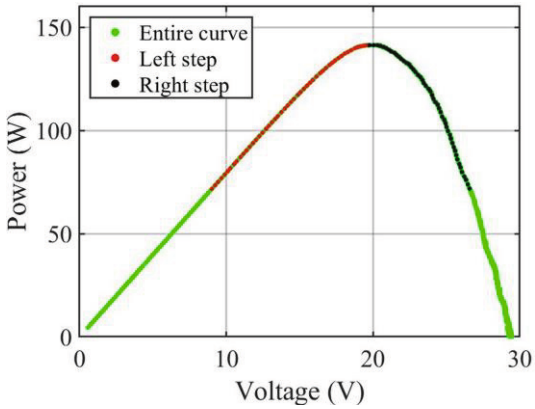

Figure 12. Measured *P-U* curve (green) jointly with 50% cutting limits of P_{MPP} on the left (red) and right (black) side of the MPP.

The second *I-U* curve cutting principle is based on the MPP voltage. Points on the *I-U* curve having a voltage difference from the MPP smaller than or equal to a fixed percentage of U_{MPP} are taken into account when fitting. Such a cutting principle is justified because the voltage is typically used as a reference quantity for the operation of the inverter. Fig. 13 shows an example of U_{MPP}-based cutting with a 35% cutting limit on either side of the MPP.

In contrast to the P_{MPP}-based cutting, the U_{MPP}-based cutting needs special attention when choosing the cutting limits, since the difference from U_{MPP} must not exceed U_{OC}. The ratio γ_U defines the maximum allowed percentage p_{max} for such a difference via the equation

$$p_{\max} = \frac{1}{\gamma_U} - 1. \tag{15}$$

There is no risk of exceeding the end of the *I-U* curve on the SC side of the curve. This is due to the wide high-current region of the *I-U* curve.

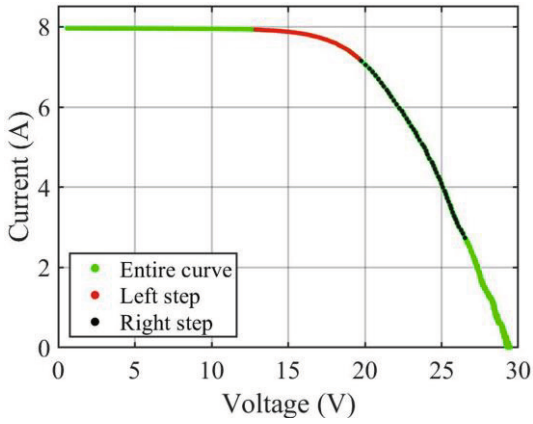

Figure 13. Measured *I-U* curve (green) jointly with cutting limits of 35% of U_{MPP} on the left (red) and right (black) side of the MPP.

It is also possible to set different cutting limits on either side of the MPP. Such a choice might come into question when, for instance, you want to determine only the series resistance, which is mainly determined by the OC slope of the *I-U* curve. Fig. 14 shows an example where the cutting percentage is 10% of P_{MPP} to the left of the MPP and 60% to the right.

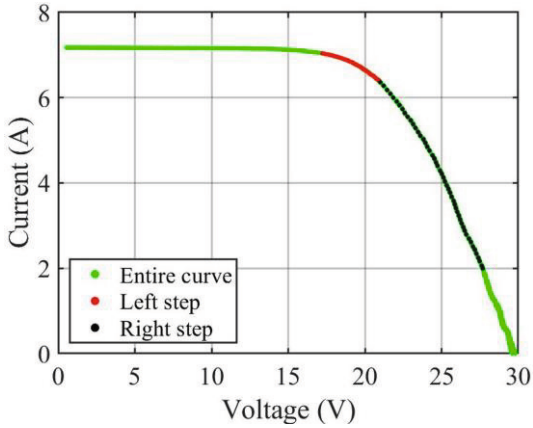

Figure 14. Measured *I-U* curve (green) jointly with the left (red) and right (black) cutting limits of 10% and 60% of P_{MPP}.

5 VALIDATION OF THE FITTING PROCEDURE

This chapter is devoted to verifying the operation of the developed single-diode model fitting procedure. Its performance was evaluated for each fitted parameter and the analysis is based on dataset A. The raw measured *I-U* curves were pre-processed as follows. The abnormal measurement points were removed as described in Section 4.2. Thereafter, the redundant voltage values were replaced with a single voltage value, and the corresponding current values were averaged to form a single current value. Such an approach was computationally faster than generating representative points when dealing with entire measured *I-U* curves.

5.1 Identification of operating conditions

Fig. 15 shows the calculated and measured irradiance values of PV module 19 as a function of time during the measurement period. The first 2500 seconds comprise a period of stable high irradiance. Thereafter, sharp irradiance transitions appear at 2600-3400 seconds. After 3400 seconds, the irradiance reaches a high level again and remains so for the rest of the measurement period.

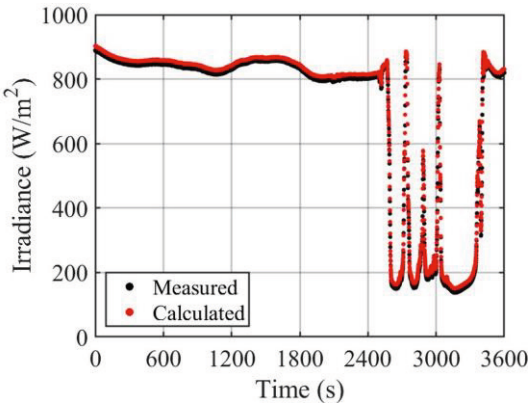

Figure 15. Calculated and measured irradiance received by module 19 as a function of time during the one-hour measurement period.

It is evident from Fig. 15 that the calculated irradiance values agree well with the measured irradiance values during stable high irradiance conditions as well as during sharp irradiance transitions. The calculated irradiance values lie slightly above the measured values, being in line with Lappalainen et al. (2020). There is an approximate difference of 10 W/m^2 between the calculated and measured irradiance values. The accurate reproduction of irradiance by the proposed fitting procedure results from the accurate fitting at the SC end, which was particularly improved by the redetermination of the $I_{SC,STC}$ value (Appendix).

The good recognition of irradiance in all operating conditions is of primary importance in terms of the usability of the developed *I-U* curve fitting procedure and enables the irradiance-based classification of the measured *I-U* curves into those used in diagnostics or excluded. Indeed, only curves measured under high irradiance conditions are valid for analysis based on the single-diode model. The possibility to classify the measured *I-U* curves enhances the usability of the fitting procedure at practical PV sites.

Fig. 16 shows the fitted operating temperature of PV module 19 jointly with its measured backplate temperature as a function of time during the one-hour measurement period. Obviously, the irradiance conditions are strongly reflected in the temperature of the PV module. For the first 2500 seconds of the measurement period, the temperature is high and relatively stable with small variations. Thereafter, a period shaded by clouds with sharp irradiance transients causes a deep drop in temperature. Finally, the return of irradiance to a high level raises the temperature again.

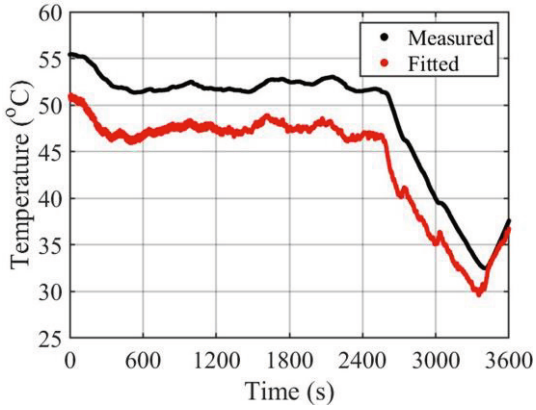

Figure 16. Fitted and measured operating temperature of PV module 19 as a function of time during the one-hour measurement period.

Fig. 16 reveals that the fitted temperature values closely follow the variation of the measured temperature. The gap between the measured and fitted temperature is in line with previous work (Lappalainen et al., 2022a). The main reason for the gap is the cooling effect of wind blowing towards the front surface of the PV module during the measurement period. The thermal inertia of the PV module is shown as a delay between the fitted and measured temperature; the heat transfer from the PV cell to the sensor located on the backplate of the PV module takes time. Taking these phenomena into account using the developed procedure would require separate wind measurements (Torres Lobera and Valkealahti, 2014), which is not in accordance with the original goals of the work to identify the examined variables only from the measured *I-U* curves. In addition, the measured temperature curve looks thinner and smoother than the fitted one. This results from two facts. Firstly, the measured *I-U* curves respond to sudden changes in the PV module temperature faster and more accurately than the temperature sensor. Secondly, it is characteristic that the parameter values calculated by the fitting procedure vary slightly around the average value.

In conclusion, the developed fitting procedure reproduces the PV module temperature consistently in all operating conditions. Such a finding is a consequence of the correct fitting of the single-diode model at the OC end of the measured *I-U* curve, regardless of the irradiance level.

5.2 Identification of series resistance

Fig. 17 shows the series resistance values identified from PV module 19 during the one-hour measurement period as a function of measurement time. During the stable high irradiance period comprising the first 2400 seconds of the measurement period, the fitted series resistance exhibits good stability, varying only slightly around 0.794 Ω. This is in line with previous studies (Lappalainen et al., 2020). The basic statistical characteristics of the fitted series resistance during the first 2400 seconds of the measurement period are given in Table 4 and the histogram in Fig. 18. The median and mean values of the series resistance are approximately equal. Such a result supports the observation that the fitted series resistance values tend to be normally distributed whenever their number is sufficiently large and the operating conditions are stable. These findings are expected, as the single-diode model performs best under stable high irradiance conditions.

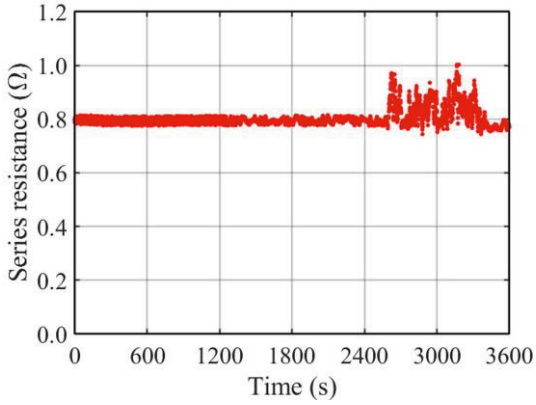

Figure 17. Fitted series resistance of PV module 19 as a function of time during the one-hour measurement period.

Table 4. Basic statistical quantities of series resistance identified from PV module 19 in stable condition of high irradiance during the first 2400 seconds of the measurement period.

Statistical quantity	Value
Mean (Ω)	0.7941
Median (Ω)	0.7942
Standard deviation (Ω)	0.0090
Interquartile range (Ω)	0.0145

The period of low irradiance with sharp transients following the high irradiance period causes the fitted series resistance to vary strongly to higher values. The increment in R_s reaches 25%, in accordance with Lappalainen et al. (2020). Generally, changes in the fitted R_s values originate from the fact that decreasing irradiance changes the shape of the *I-U* curve. Indeed, the curvature around the MPP as well as the slope of the *I-U* curve in the high-voltage region are changed. Fig. 19 shows the fitted series resistance during the one-hour measurement period as a function of measured irradiance. It is evident from Fig. 19 that as the irradiance decreases, the fitted R_s values increase considerably and their dispersion increases.

The direction of the change in the fitted series resistance values depends on the selected value of the ideality factor. The value $A = 1.1$ utilised in the present study makes the series resistance shift upwards from the main trend of R_s under stable high irradiance condition. It was experimentally observed that setting $A = 1.3$ produces downward shifts in the fitted R_s values at low irradiances which are

even larger than those shown in Fig. 17. This phenomenon is explained by the role of the ideality factor for the curvature of the *I-U* curve in the MPP region. Indeed,

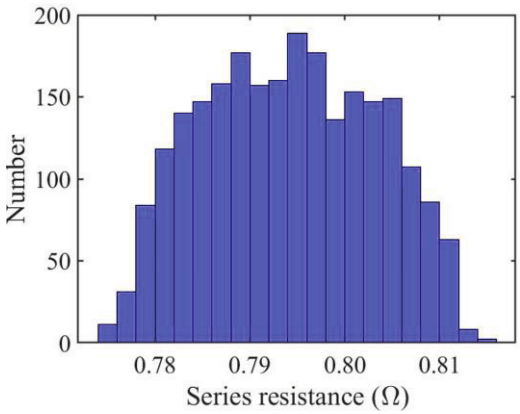

Figure 18. Histogram of fitted series resistance values obtained during the stable high irradiance condition of the first 2400 seconds of the measurement period.

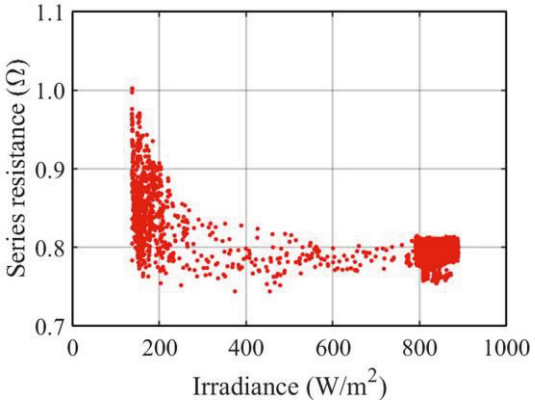

Figure 19. Fitted series resistance of PV module 19 as a function of measured irradiance during the one-hour measurement period.

all the single-diode model parameters are strongly interconnected; any change in one parameter affects the others as well.

The series resistance is again stable at the end of the measurement period because the irradiance coming to the module is also consistently high. However, it is slightly smaller than at the beginning of the measurement period. The difference stems from the fact that the PV module's operating temperature is significantly lower after shading at the end of the measurement period. Such a finding suggests

a slight positive temperature dependence of R_s (De Soto et al., 2006; Piliougine et al., 2020).

These findings confirm the functionality of the developed single-diode model fitting procedure for the reliable identification of series resistance in stable high irradiance conditions. In contrast, low irradiance conditions are unsuitable for series resistance analysis as expected.

5.3 Identification of other single-diode model parameters

Fig. 20 shows the fitted photocurrent values obtained during the one-hour measurement period as a function of measured irradiance. The identified I_{ph} value increases linearly as the irradiance increases, as expected. The small deviation of the obtained values around the linear trend stems mostly from the minor temperature dependence of the photocurrent, since the measured temperature varies by more than 20 °C during the measurement period. It should be noted that I_{ph} is correctly identified even at low irradiance levels. This is because the fitting procedure correctly follows the SC end of the measured *I-U* curve at any irradiance level.

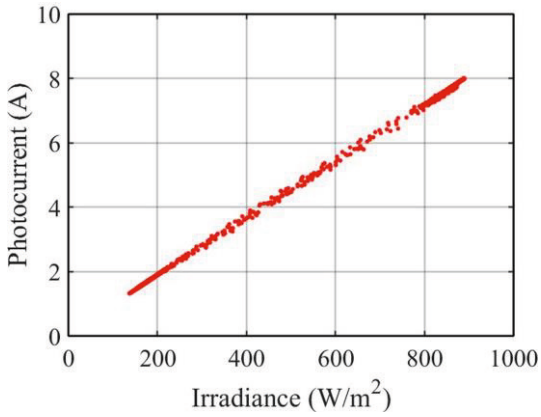

Figure 20. Fitted photocurrent of PV module 19 as a function of measured irradiance during the one-hour measurement period.

Fig. 21 shows the fitted shunt resistance values during the one-hour measurement period as a function of the measurement time. The obtained shunt resistance values deviate largely from each other even at stable high irradiance conditions. The appearance of deviation in fitted R_h values is expected, as the single-diode model is not sensitive to the value of this parameter (Rashel et al.,

2016). However, the deviation is larger than that obtained in Lappalainen et al. (2022a). The R_h values obtained under high irradiance conditions are in the order of a few hundred **Ω**, being well above 200 **Ω**. These findings are in accordance with a previous study (Lappalainen et al. 2020).

Fig. 22 shows the fitted R_h values converted to STC via (10) during the one-hour measurement period as a function of the measurement time. The conversion of fitted shunt resistance to STC reduces the deviation of the R_h values. However, the deviation is still too large for these values to be used for reliable diagnosis, even in high irradiance conditions. The poor performance of the single-diode model at low irradiance conditions is visible in Figs. 21-22 between 2600 and 3400 s.

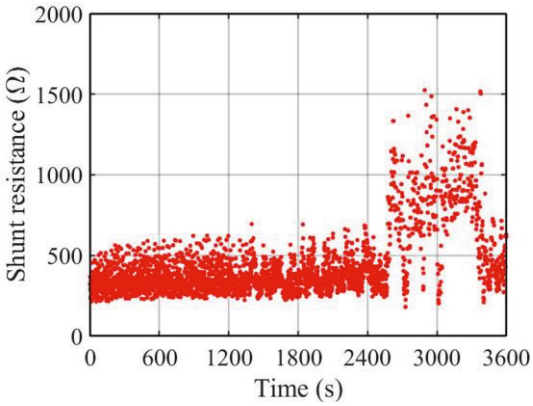

Figure 21. Fitted shunt resistance as a function of time during the one-hour measurement period.

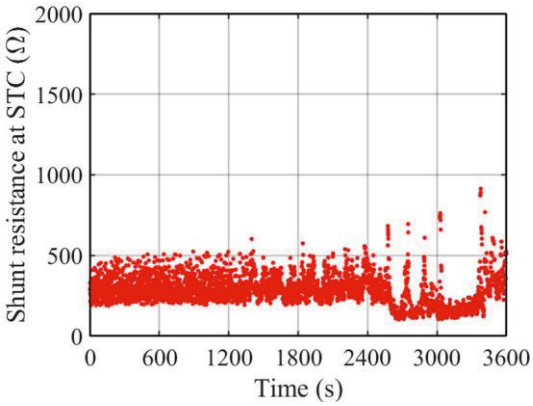

Figure 22. Fitted shunt resistance converted to STC as a function of time during the one-hour measurement period.

Figs. 23-24 show the fitted dark saturation current during the one-hour measurement period as functions of the measurement time and measured PV module operating temperature, respectively. The magnitude of the identified I_o values is some fractions of μA, which is in line with a previous study (Meyer, 2017). The strong dependence of I_o on the operating conditions is visible in both figures (compare Figs. 15-16).

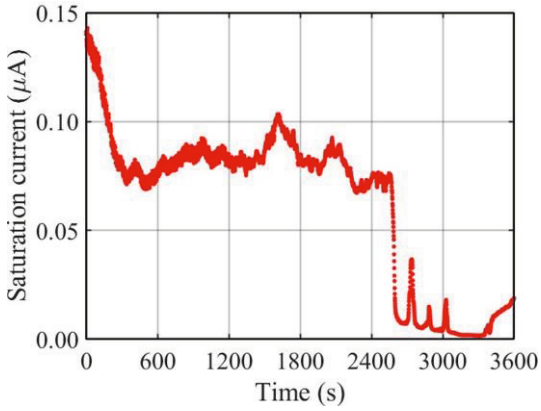

Figure 23. Fitted dark saturation current of PV module 19 as a function of time during the one-hour measurement period.

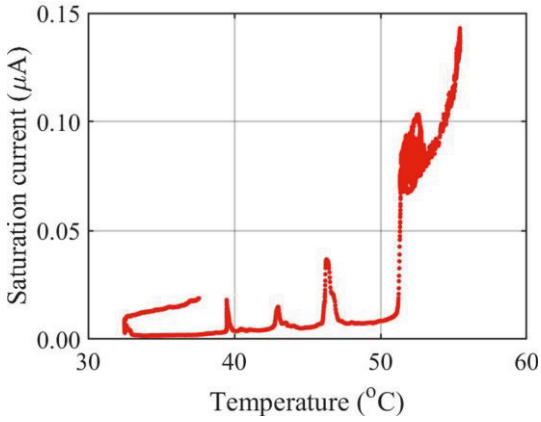

Figure 24. Fitted dark saturation current of PV module 19 during the one-hour measurement period as a function of the measured operating temperature of the PV module.

The observed behaviour of the fitted parameters I_{ph}, R_h and I_o shows that the developed fitting procedure also works for them and they behave as expected

under varying operating conditions. However, more detailed analysis of I_{ph}, R_h and I_o is out of scope of the present work.

6 FITTING TO PARTIAL CURRENT-VOLTAGE CURVES

This chapter is devoted to investigating the performance of the developed single-diode model fitting procedure for partial *I-U* curves. Its performance was evaluated in terms of I_{ph}, R_s, and T, as these three parameters provide the most important diagnostic information. Where necessary, the fitted parameters are converted to STC in order to eliminate the effect of operating conditions from the obtained parameters. Since the possible use of the measured partial *I-U* curves is related to online condition monitoring, the analysis is performed in the best operating range of the single-diode model. Hence the analysis is based on dataset B measured under stable conditions of high irradiance.

The raw measured *I-U* curves are pre-processed as follows. The abnormal measurement points are removed as described in Section 4.2. Thereafter, the measurement range of the *I-U* curve used for fitting is divided into 100 representative points as described in Section 4.3. This number of points is large enough to preserve the original shape of the measured *I-U* curve regardless of the measurement range, but at the same time small enough to be used with the smallest measured partial *I-U* curves. The representative points are equally distributed along the measured parts of the *I-U* curve as described in Section 4.3, which ensures the comparability of the results.

6.1 Fitting to partial current-voltage curves based on the MPP power limit

Throughout this section, the *I-U* curve cutting principle is symmetrical with respect to the MPP power estimated as described in Section 4.4. This means that the same power limit is applied for either side of the MPP.

Fig. 25 shows the fitted photocurrents converted to STC during the 40-minute measurement period as a function of the P_{MPP}-based cutting limit. The

corresponding statistical quantities are presented in Table 5. Obviously, a cutting limit of 60% or more provides accurate results with a small deviation; the scatter of the calculated $I_{ph,STC}$ values increases significantly with smaller cutting limits. Such a finding is of practical significance, showing that 60% of the top of the *P-U* curve is sufficient for a reliable analysis of $I_{ph,STC}$. The mean $I_{ph,STC}$ values in that region are in excellent agreement with the real $I_{SC,STC}$ value of PV module 19 (Table 1) being only some fractions of a per cent higher. Table 5 reveals that the deviation from the mean photocurrent of the entire curve first slightly increases as the cutting limit of the curve decreases and more quickly after 60%. Also, the standard deviation increases first slightly and then faster with a decreasing cutting limit, being finally ten-fold for the cutting limit of 10% of P_{MPP}. An interesting finding is also that the calculated $I_{ph,STC}$ values share a common lower threshold of around 8.71 A, which corresponds closely to the real $I_{SC,STC}$ value of PV module 19. This is because the fitted *I-U* curve either always exactly matches the SC end of the measured curve or exceeds it but never falls below it.

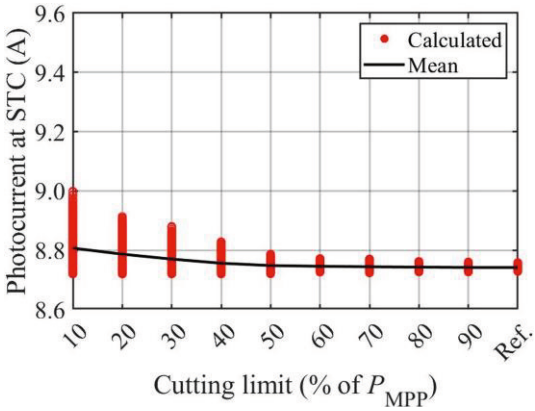

Figure 25. Fitted photocurrents at STC as a function of the P_{MPP}-based *I-U* curve cutting limit during the 40-minute measurement period.

Table 5. Basic statistical quantities of photocurrent converted to STC during the 40-minute measurement period for different P_{MPP}-based *I-U* curve cutting limits.

Cutting limit (% of P_{MPP})	Mean (A)	Median (A)	Standard deviation (A)	Interquartile range (A)
Entire curve	8.7417	8.7416	0.0054	0.0080
90	8.7418	8.7418	0.0060	0.0085
80	8.7429	8.7429	0.0062	0.0087
70	8.7442	8.7439	0.0094	0.0148
60	8.7459	8.7455	0.0085	0.0118
50	8.7483	8.7486	0.0150	0.0261
40	8.7561	8.7462	0.0305	0.0581
30	8.7700	8.7554	0.0471	0.0927
20	8.7867	8.7836	0.0603	0.1226
10	8.8071	8.8151	0.0702	0.1363

Fig. 26 shows the fitted series resistances as a function of the P_{MPP}-based cutting limit during the 40-minute measurement period. The corresponding statistical quantities are provided in Table 6. The mean series resistance increases only marginally, being almost constant when the cutting limit decreases. This indicates that series resistance can be determined by analysing partial *I-U* curves measured very close to the MPP. However, the standard deviation increases strongly when the cutting limit is below 50%, increasing the uncertainty of the fitted parameter.

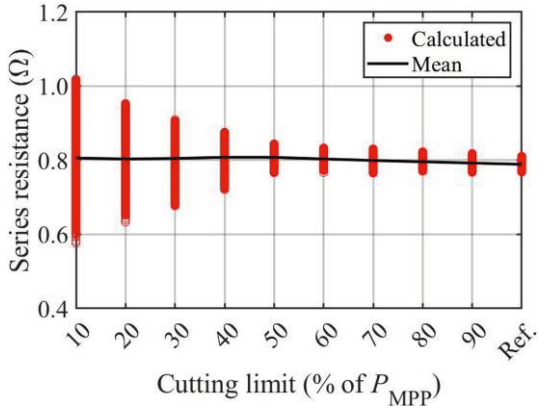

Figure 26. Fitted series resistances as a function of the P_{MPP}-based *I-U* curve cutting limit during the 40-minute measurement period.

Table 6. Basic statistical quantities of series resistances during the 40-minute measurement period for different P_{MPP}-based *I-U* curve cutting limits.

Cutting limit (% of P_{MPP})	Mean (Ω)	Median (Ω)	Standard deviation (Ω)	Interquartile range (Ω)
Entire curve	0.7892	0.7892	0.0098	0.0161
90	0.7925	0.7924	0.0126	0.0219
80	0.7960	0.7961	0.0132	0.0248
70	0.7995	0.8000	0.0156	0.0244
60	0.8036	0.8040	0.0150	0.0248
50	0.8079	0.8079	0.0169	0.0253
40	0.8081	0.8131	0.0367	0.0605
30	0.8050	0.8137	0.0620	0.1104
20	0.8035	0.7984	0.0841	0.1563
10	0.8060	0.7888	0.1055	0.1800

Fig. 27 shows the fitted temperature values obtained during the 40-minute measurement period as a function of the P_{MPP}-based *I-U* curve cutting limit. The calculated mean temperature decreases slightly as the cutting limit decreases. The reason is that the high-voltage region of the *I-U* curve is not completely linear but curves downwards, resulting in an increase in U_{OC} values and a decrease in temperature as the cutting limit increases. The same reason also leads to an increase in series resistance as the cutting limit decreases. The scatter of the temperature is almost constant above the cutting limit of 50% of P_{MPP}. For cutting

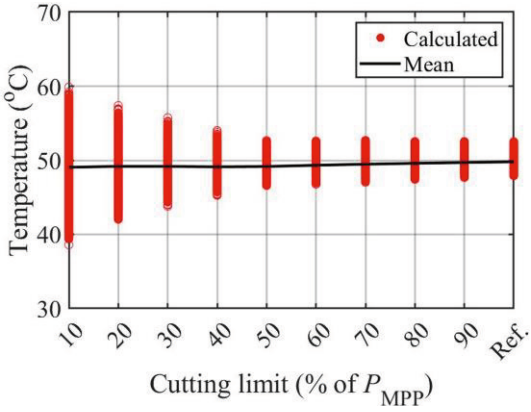

Figure 27. Fitted temperatures as a function of the P_{MPP}-based *I-U* curve cutting limit during the 40-minute measurement period.

limits smaller than 50% of P_{MPP}, the scatter of the fitted temperature clearly increases with the decreasing cutting limit. Such a finding reflects the instability of the fitting procedure if the *I-U* curve is cut too much.

Fig. 28 shows the number of iterations and Fig. 29 the number of objective function evaluations per one *I-U* curve fit as a function of the P_{MPP}-based cutting limit during the 40-minute measurement period. The number of iterations is smallest when fitting the single-diode model to the measured full *I-U* curves, and remained small up to the cutting limit of 50% of P_{MPP}. If the cutting limit is further reduced, the scatter in the number of iterations increases significantly. Such a finding results from the instability of the fitting procedure when the *I-U* curve is

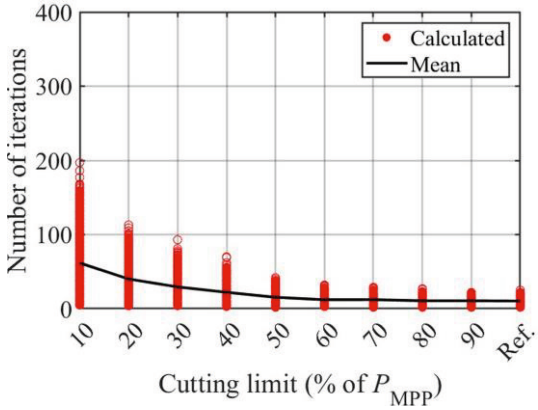

Figure 28. Number of iterations needed for fitting as a function of the P_{MPP}-based *I-U* curve cutting limit during the 40-minute measurement period.

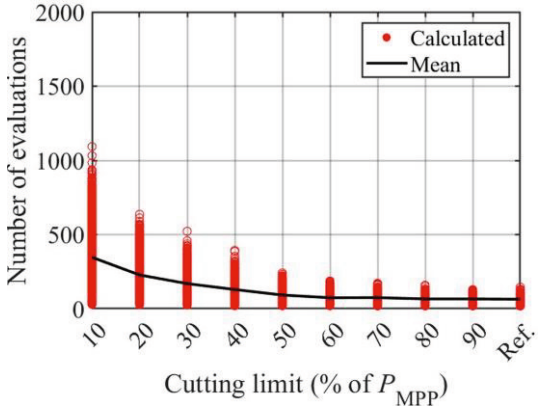

Figure 29. Number of objective function evaluations needed for fitting as a function of the P_{MPP}-based *I-U* curve cutting limit during the 40-minute measurement period.

cut too much. The findings related to Fig. 28 are also directly visible in Fig. 29. The objective function is evaluated on average five times during one iteration.

6.2 Fitting to partial current-voltage curves based on the MPP voltage limit

Throughout this section, the *I-U* curve cutting principle is symmetrical with respect to the MPP voltage estimated as described in Section 4.4. This means that an equal voltage limit is applied either side of the MPP. Due to the nonlinear shape of the *I-U* curve, the high-voltage side of the curve is covered more than the high-current side. This causes a different distance between adjacent representative points on the left and right sides of the MPP. There are 50 representative points on both sides of the MPP, and they are denser in the high-current region than in the high-voltage region.

As earlier explained, the maximum cutting percentage is defined by the quantity γ_U. Its minimum value for dataset B is slightly above 0.7, requiring the upper limit for the cutting percentage to be 0.39. The maximum cutting percentage is chosen to be 35% in the present work. The entire measured *I-U* curves serve as the reference in this case as well.

Fig. 30 shows the calculated $I_{ph,STC}$ values during the 40-minute measurement period as a function of the U_{MPP}-based cutting limit. The related statistical quantities are reported in Table 7. The scatter compared to the reference case is large for all the studied cutting limits and significantly exceeds the scatters of the P_{MPP}-based cutting limits. This results from the fact that the SC slope of the measured partial *I-U* curve is less covered than the OC slope and has less weight during the fitting. The more the *I-U* curve is cut, the more the calculated $I_{ph,STC}$ values deviate. The calculated mean $I_{ph,STC}$ value increases considerably with the increasing cutting limit. However, all the $I_{ph,STC}$ values lie over a common threshold of around 8.71 A, meaning that the fitted curves never underestimate the SC current but can overestimate it strongly. It can be concluded that the U_{MPP}-based symmetrical cutting limit is not a viable approach for online condition monitoring applications that analyse parameters related to the SC slope of the *I-U* curve.

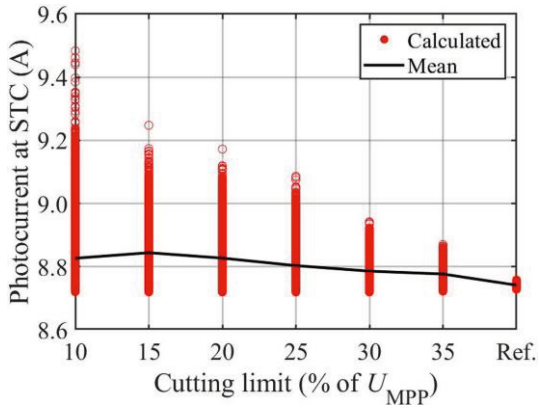

Figure 30. Fitted photocurrent values converted to STC as a function of the U_{MPP}-based *I-U* curve cutting limit during the 40-minute measurement period.

Table 7. Basic statistical quantities of photocurrent converted to STC during the 40-minute measurement period for different U_{MPP}-based *I-U* curve cutting limits.

Cutting limit (% of U_{MPP})	Mean (A)	Median (A)	Standard deviation (A)	Interquartile range (A)
Entire curve	8.7417	8.7416	0.0054	0.0080
35	8.7769	8.7753	0.0303	0.0467
30	8.7861	8.7680	0.0573	0.1035
25	8.8035	8.7420	0.0936	0.1667
20	8.8272	8,7843	0.1103	0.2040
15	8.8444	8.8479	0.1122	0.2058
10	8.8269	8.7433	0.1379	0.1771

Fig. 31 shows the fitted series resistance values of the partial *I-U* curves as a function of the U_{MPP}-based cutting limit obtained during the 40-minute measurement period. The corresponding statistical quantities are reported in Table 8. The deviation of the fitted series resistances at any studied cutting limit is much larger than the deviation of the series resistance obtained utilising the entire measured *I-U* curves. This is also the case for the largest cutting limit of 35%, although most of the OC slope is covered. The deviation increases strongly with the decreasing cutting limit. Such findings indicate that U_{MPP}-based symmetrical cutting is not an optimal choice for series resistance identification either. This problem is not alleviated even by the mean value of R_s, which is nearly constant regardless of the cutting limit, because the deviation of the fitted values around the mean is too large for a reliable diagnosis.

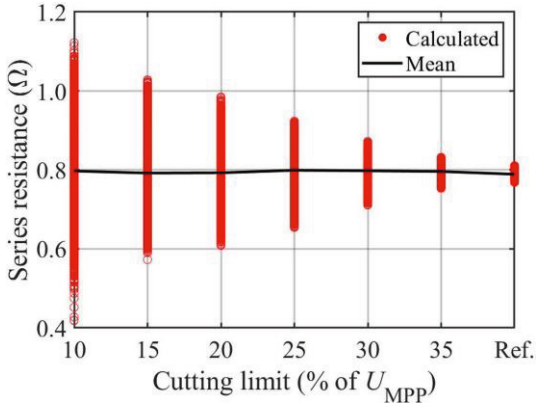

Figure 31. Fitted series resistances as a function of the U_{MPP}-based *I-U* curve cutting limit during the 40-minute measurement period.

Table 8. Basic statistical quantities of series resistances during the 40-minute measurement period for different U_{MPP}-based *I-U* curve cutting limits.

Cutting limit (% of U_{MPP})	Mean (Ω)	Median (Ω)	Standard deviation (Ω)	Interquartile range (Ω)
Entire curve	0.7892	0.7892	0.0098	0.0161
35	0.7962	0.7963	0.0173	0.0266
30	0.7979	0.8000	0.0303	0.0441
25	0.7992	0.8094	0.0667	0.1148
20	0.7929	0.7883	0.0969	0.1811
15	0.7922	0.7708	0.1133	0.1937
10	0.7973	0.7862	0.1247	0.1770

Fig. 32 shows the fitted temperature values obtained during the 40-minute measurement period as a function of the U_{MPP}-based cutting limit. The fitted temperature values vary strongly around the average values and a larger cutting of the *I-U* curve leads to larger variation in the fitted temperature. When the average series resistance of Fig. 31 slightly increases, the average temperature of Fig. 32 decreases. Such a result is a natural consequence of the combined effect of temperature and series resistance on the OC slope of the *I-U* curve. An increment in fitted temperature value is associated with a decrease in fitted U_{OC} value, which in turn causes the fitted R_s to decrease.

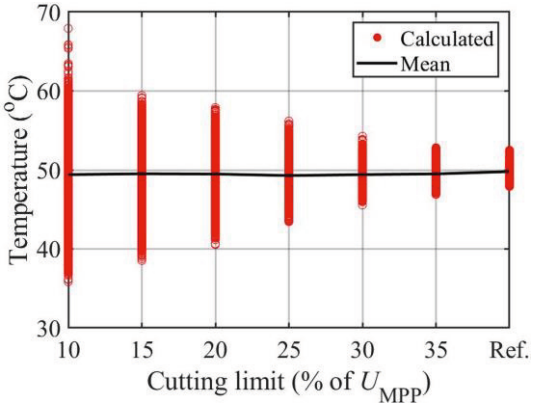

Figure 32. Fitted temperatures as a function of the U_{MPP}-based *I-U* curve cutting limit during the 40-minute measurement period.

Fig. 33 shows the number of iterations and Fig. 34 the number of objective function evaluations per one *I-U* curve fit as a function of the U_{MPP}-based *I-U* curve cutting limit during the 40-minute measurement period. Remarkably, the numbers of iterations and objective function evaluations needed in the U_{MPP}-based cutting are significantly larger than those in the P_{MPP}-based cutting. This is because the algorithm has an obvious difficulty in fitting the single-diode model to partial *I-U* curves that cover only a small part of the SC slope.

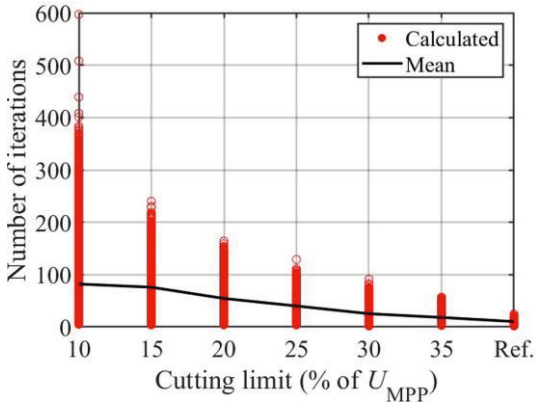

Figure 33. Number of iterations needed for fitting as a function of the U_{MPP}-based *I-U* curve cutting limit during the 40-minute measurement period.

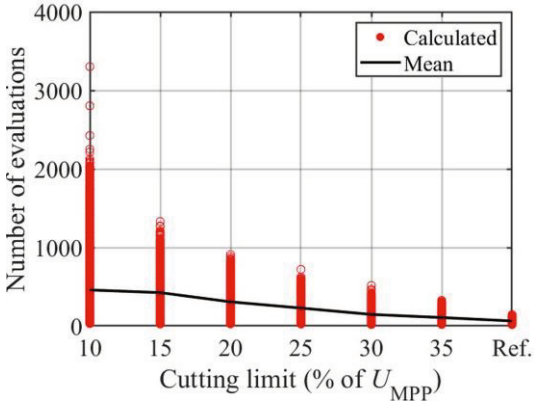

Figure 34. Number of objective function evaluations needed for fitting as a function of the U_{MPP}-based *I-U* curve cutting limit during the 40-minute measurement period.

7 AGEING DETECTION

This chapter is devoted to investigating the ageing detection capability of the developed single-diode model fitting procedure. The analysis focuses fully on the identification of the series resistance parameter.

In practical condition monitoring applications, no reliable diagnostic conclusions can be drawn based only on few randomly measured *I-U* curves. Instead, a sufficiently large number of successive *I-U* curves measured at stable high irradiance conditions must be analysed. However, there are no previous studies of a sufficient number of measured *I-U* curves for this purpose. This issue has been addressed in Section 7.1 (Kalliojärvi et al., 2022).

The capability of the single-diode model fitting procedure to quantify ageing from entire and partial measured *I-U* curves is investigated in Sections 7.2 and 7.3. Ageing was modelled by adding two resistors of different sizes, each in turn, in series with the PV module, and then identifying the series resistance from the measured *I-U* curves. One resistor (0.22 Ω) emulates moderate ageing, while the other (0.69 Ω) emulates severe ageing. Datasets C, D, and E described in Chapter 4 were used for the analysis. In Section 7.2, the *I-U* curves are cut symmetrically based on the P_{MPP} percentages. The investigation of the symmetrical U_{MPP}-based cutting of *I-U* curves is omitted due to its weak capability to produce series resistance correctly (Section 6.2). However, since series resistance is a key quantity in ageing detection, it is reasonable to ask whether it could be better identified by focusing the measurement range of the *I-U* curve on the OC slope (Sera et al., 2008). Compromising the correctness of other fitting parameters, the P_{MPP}- and U_{MPP}-based *I-U* curve cutting principles can be applied by setting different cutting limits on either side of the MPP. This issue is investigated in Section 7.3.

7.1 Number of current-voltage curves needed for series resistance analysis

The analysis is based on the fact that the fitted R_s values obtained under stable operating conditions have a characteristic deviation around the average value due to the fitting and measurement methods of the *I-U* curve. If the number of analysed *I-U* curves is too small, the entire deviation range is not reached and the statistical reliability of the analysis suffers. Hence the behaviour of the R_s deviation as a function of the number of *I-U* curves was analysed. Entire measured *I-U* curves were used in the analysis, so that the deviation of the fitted R_s values due to cutting the curves did not affect the results.

Two non-overlapping subsets of dataset B are analysed. The corresponding measurement periods are 1-600 s (Case A) and 1201-1800 s (Case B). These periods were measured under stable high-irradiance conditions. However, their temperature profiles differ from each other, as shown in Fig. 35. In case A, the temperature is clearly higher at the beginning than in case B, but then drops by about 4 ºC. Such differences in temperature are expected to have an impact on the obtained series resistance values because of the slight temperature dependence of the series resistance.

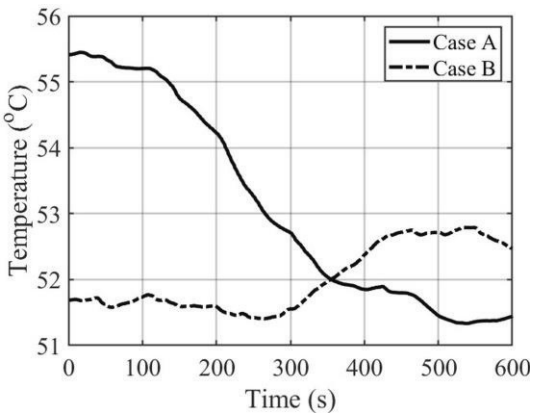

Figure 35. Measured PV module temperatures during the 10-minute measurement periods selected for the analysis of the scatter in fitted series resistances.

Figs. 36-37 show the fitted series resistance values of Case A and Case B as a function of the number of the analysed *I-U* curves. The corresponding key statistical quantities are reported in Table 9. The series resistances have slightly

larger values in Case A than in B, partly because of the higher temperatures in Case A. The deviation of the fitted R_s values reaches stability in a shorter time in Case B than in Case A. This difference is explained by the smaller deviation of the PV module's temperature during the measurement period of Case B. Fig. 36 and Table 9 reveal that the obtained mean series resistance decreased about 0.4% when the temperature decreased by 4 °C. Such a finding is to be noted when designing real-case condition monitoring applications. Nevertheless, neither the mean of the fitted series resistance nor its standard deviation was especially sensitive to the number of analysed *I-U* curves. In this light, a measurement period of few minutes is sufficient for reliable series resistance analysis.

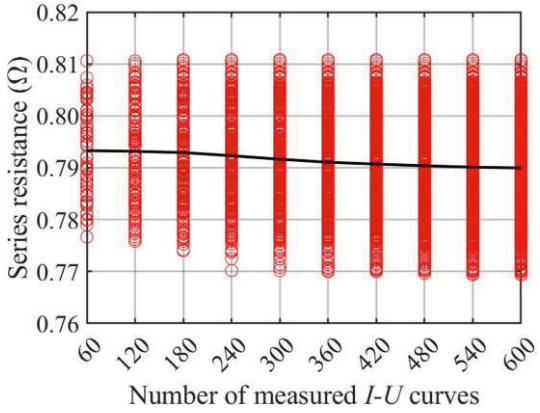

Figure 36. Fitted series resistance values and their mean value (black line) as a function of the number of measured *I-U* curves used for analysis in Case A.

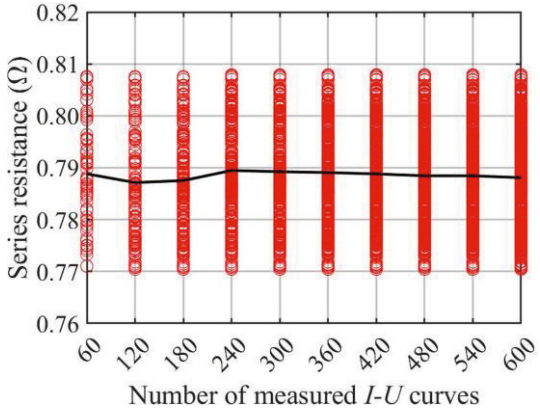

Figure 37. Fitted series resistance values and their mean value (black line) as a function of the number of measured *I-U* curves used for analysis in Case B.

Table 9. Basic statistical quantities of fitted series resistances for different numbers of analysed *I-U* curves in Cases A and B.

	A		B	
Number of *I-U* curves	Mean (Ω)	Standard deviation (Ω)	Mean (Ω)	Standard deviation (Ω)
60	0.7933	0.0085	0.7888	0.0102
120	0.7932	0.0093	0.7871	0.0105
180	0.7929	0.0095	0.7875	0.0100
240	0.7923	0.0096	0.7895	0.0101
300	0.7916	0.0097	0.7892	0.0099
360	0.7911	0.0098	0.7891	0.0096
420	0.7907	0.0099	0.7888	0.0094
480	0.7904	0.0098	0.7884	0.0091
540	0.7901	0.0099	0.7884	0.0091
600	0.7900	0.0100	0.7881	0.0091

The analysis reveals that a measurement period of few minutes with a 1 Hz sampling frequency is sufficient for the reliable determination of the series resistance of the PV module. However, a reliable analysis seems to require sufficiently stable high irradiance conditions. These findings have a practical meaning when designing the condition monitoring procedures for PV systems and also serve as guidelines for future research.

7.2 Ageing detection based on entire and symmetrically limited partial current-voltage curves

It is reasonable to ask whether the identification of series resistance performs equally well for differently aged PV modules, since an increase in the series resistance changes the shape of the *I-U* curve. Hence the performance of the fitting procedure must be tested for PV modules exhibiting different stages of ageing. This was modelled by adding two resistors of different sizes, each in turn, in series with the PV module. The issue is addressed in this section by analysing entire measured *I-U* curves as well as curves symmetrically cut with respect to the P_{MPP}, as it proved to be a promising online parameter identification approach (Section 6.1).

Fig. 38 shows the fitted series resistances obtained from the entire measured *I-U* curves of non-aged ($R_{s,add}$ = 0.00 Ω), moderately aged ($R_{s,add}$ = 0.22 Ω), and severely aged ($R_{s,add}$ = 0.69 Ω) PV modules as a function of time during 1300-second measurement periods of stable high irradiance. The identified resistances are very stable with a small deviation around the average value in each studied case of emulated ageing. This indicates that the developed identification procedure is also stable for aged PV modules. The fitting procedure also reproduces the emulated ageing of the PV module with additional series resistors well. Hence, the fitting procedure seems to be a reliable diagnostic tool at least for entire measured *I-U* curves.

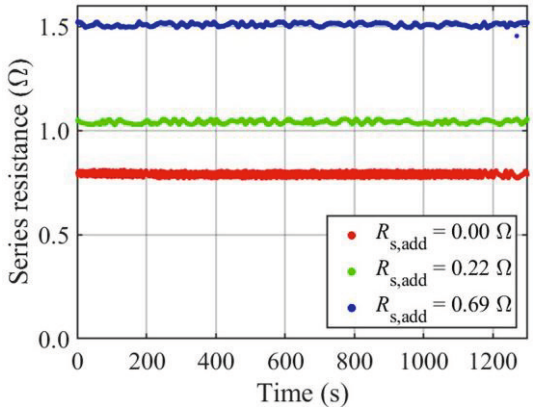

Figure 38. Fitted series resistances as a function of time during the 1300-second measurement periods obtained from entire *I-U* curves.

Figs. 39-40 show the series resistance values for partial *I-U* curves obtained using cutting limits of 50% and 20% of P_{MPP}. The developed fitting procedure produces stable series resistances with a relatively small deviation around the average identified R_s value when the 50% cutting limit is used. As is expected, the scatter in the fitted R_s is slightly larger than for entire measured *I-U* curves. Remarkably, the series resistance value is identified equally well for aged and non-aged PV modules. Hence, *I-U* curves symmetrically cut at down to 50% of P_{MPP} can be well-utilised in ageing analysis using the developed fitting procedure. In contrast, Fig. 40 serves as an example of a too small cutting limit. Although the fitted series resistances exhibit equally large scatter in each studied ageing case, the scatter seems to be too large for reliable diagnosis. Maybe they, too, could be utilised using suitable statistical analysis, as the values seem to fluctuate around the same averages as when using entire *I-U* curves.

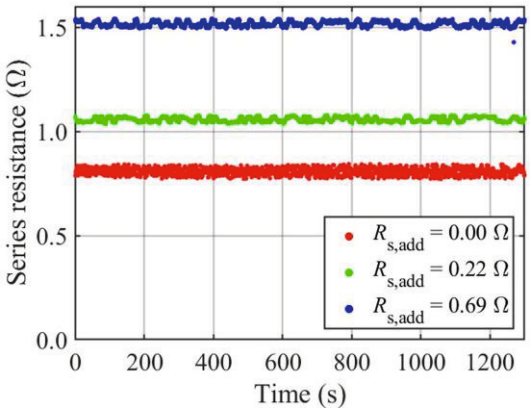

Figure 39. Fitted series resistances as a function of time for partial *I-U* curves with a cutting limit of 50% of P_{MPP} during the 1300-second measurement periods.

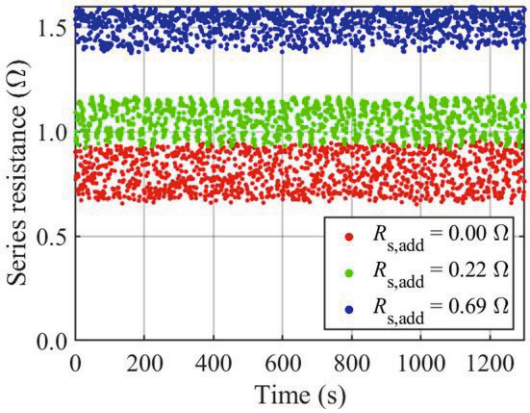

Figure 40. Fitted series resistances as a function of time for partial *I-U* curves with a cutting limit of 20% of P_{MPP} during the 1300-second measurement periods.

In order to provide a more systematic quantitative analysis, Tables 10-12 provide the key statistical quantities of the fitted series resistances as a function of the P_{MPP}-based cutting limits for the non-aged, moderately aged, and severely aged PV module. The figures in Table 10 are well in line with Table 6. Such a result is expected because it has been previously shown that a few hundred measured *I-U* curves are sufficient for reliable analysis of R_s. Figs. 41-42 visualise the results of Tables 11-12, showing the fitted R_s values as a function of the P_{MPP}-based cutting limit for the moderately aged and the severely aged PV module, respectively.

Table 10. Basic statistical quantities of fitted series resistances obtained from 1300 measured *I-U* curves without using additional series resistance with the PV module for different P_{MPP}-based cutting limits.

Cutting limit (% of P_{MPP})	Mean (Ω)	Median (Ω)	Standard deviation (Ω)	Interquartile range (Ω)
Entire curve	0.7894	0.7896	0.0101	0.0167
90	0.7926	0.7926	0.0130	0.0225
80	0.7959	0.7963	0.0134	0.0247
70	0.7994	0.7999	0.0156	0.0247
60	0.8032	0.8035	0.0151	0.0246
50	0.8075	0.8077	0.0166	0.0246
40	0.8087	0.8148	0.0362	0.0592
30	0.8059	0.8141	0.0620	0.1103
20	0.8040	0.7988	0.0841	0.1584
10	0.8080	0.7912	0.1016	0.1712

Table 11. Basic statistical quantities of fitted series resistances obtained from 1300 measured *I-U* curves using additional series resistance of 0.22 Ω with the PV module for different P_{MPP}-based cutting limits.

Cutting limit (% of P_{MPP})	Mean (Ω)	Median (Ω)	Standard deviation (Ω)	Interquartile range (Ω)
Entire curve	1.0401	1.0396	0.0079	0.0130
90	1.0436	1.0427	0.0101	0.0172
80	1.0465	1.0456	0.0110	0.0185
70	1.0496	1.0484	0.0112	0.0200
60	1.0533	1.0532	0.0136	0.0209
50	1.0568	1.0540	0.0111	0.0203
40	1.0593	1.0588	0.0219	0.0336
30	1.0598	1.0672	0.0453	0.0809
20	1.0596	1.0672	0.0690	0.1280
10	1.0560	1.0428	0.0968	0.1768

Table 12. Basic statistical quantities of fitted series resistances obtained from 1300 measured *I-U* curves using additional series resistance of 0.69 Ω with the PV module for different P_{MPP}-based cutting limits.

Cutting limit (% of P_{MPP})	Mean (Ω)	Median (Ω)	Standard deviation (Ω)	Interquartile range (Ω)
Entire curve	1.5077	1.5079	0.0079	0.0139
90	1.5103	1.5103	0.0101	0.0183
80	1.5119	1.5113	0.0112	0.0195
70	1.5134	1.5128	0.0109	0.0214
60	1.5147	1.5141	0.0129	0.0196
50	1.5159	1.5131	0.0125	0.0221
40	1.5181	1.5182	0.0154	0.0231
30	1.5180	1.5244	0.0317	0.0511
20	1.5086	1.5251	0.0580	0.0988
10	complex	complex	complex	complex

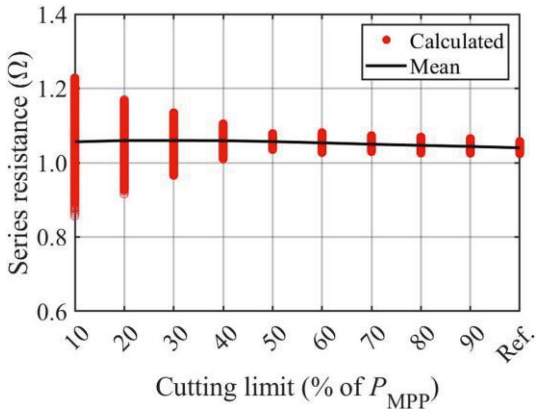

Figure 41. Series resistances obtained during the 1300-second measurement period of *I-U* curves as a function of the P_{MPP}-based cutting limit for module 19 with $R_{s,add}$ = 0.22 Ω.

Table 12 shows that the fitting procedure encountered a problem when the cutting limit was reduced to 10% of P_{MPP} for the severely aged PV module. Indeed, the algorithm then occasionally returned complex parameter values without a physical meaning. Such a result stems from the fact that the MPP curvature of the *I-U* curve of a severely aged PV module is levelled off. Hence it is difficult to fit the single-diode model to such a curve when only a very limited region around the MPP is used for fitting. However, this is not a serious limitation, as the parameter

values of successfully fitted *I-U* curves with small cutting limit are already known to deviate too strongly for reliable diagnosis.

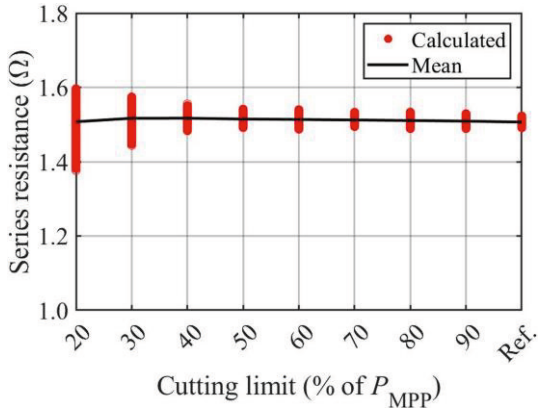

Figure 42. Fitted series resistances obtained during the 1300-second measurement period of *I-U* curves as a function of the P_{MPP}-based cutting limit for module 19 with $R_{s,add}$ = 0.69 Ω.

Tables 10-12 reveal that P_{MPP}-based *I-U* curve cutting behaves similarly for all stages of ageing. The mean of the fitted series resistances increases only slightly the more the curves are cut, and the same is true with the standard deviation down to a 50% cutting limit. When the *I-U* curves are cut below the cutting limit of 50%, the standard deviation increases faster. In addition, the standard deviation and interquartile range behave approximately similarly in Tables 10-12 as functions of the cutting limit. The minor differences are explained by slightly different operating conditions and the scattered nature of the fitted parameters resulting from the optimisation procedure.

In conclusion, the cutting limits of 50-100% of P_{MPP} provide stable values of identified series resistance for all stages of ageing. Hence, the measurement range of the *I-U* curve can be selected freely within these limits. Such a finding provides a practical guideline for the development of the proposed approach towards a full online condition monitoring approach. In contrast, the usage of smaller cutting limits does not allow for reliable diagnostic results by using the parameter identification approach presented in this thesis.

7.3 Ageing detection based on asymmetrically limited partial current-voltage curves

As series resistance is mainly determined by the OC slope of the *I-U* curve, the question arises primarily of using that range for fitting the single-diode model. Therefore, the capability of the developed fitting procedure to identify R_s is tested by using asymmetrically measured *I-U* curves with the major emphasis on the high-voltage region. In this section, the symmetrical P_{MPP}-based cutting method serves as an appropriate reference.

Tables 13-15 report the basic statistical quantities of the identified series resistances during 300-second high-irradiance measurement periods of *I-U* curves cut based on the P_{MPP} percentages for differently aged PV modules. The measurement periods are the first 5 minutes of datasets C, D, and E. The main emphasis in fitting is on the OC slope of the *I-U* curve. The cutting limits on the left and right side of the MPP are varied within the ranges of 10%-40% and 40%-60% of P_{MPP}, respectively. These choices are based on the observation that a symmetrical cutting limit of 50% of P_{MPP} still performed well in detecting series resistance.

Tables 13-15 show the behaviour of the fitted series resistance when the cutting limits are varied. If the cutting limit on one side of the MPP is fixed, a decrease of the cutting limit on the other side weakens the accuracy of R_s detection. This occurs at all stages of PV module ageing. If only the left cutting limit is decreased, then the average fitted R_s values decrease. This effect is caused by the increased emphasis of the OC slope in fitting, while the weight of the SC slope decreases. If only the right cutting limit is decreased, then the average fitted R_s values increase. Correspondingly, this effect originates from the increased emphasis of the SC slope.

For all the cutting cases reported in Tables 13-15, the deviation of the fitted R_s values is larger than that obtained by using a symmetrical P_{MPP}-based cutting limit of 50%. However, the smallest cutting percentages still producing a tolerable deviation in the identified R_s values seem to be 20% on the left side of MPP and 50%-60% on the right side.

Table 13. Basic statistical quantities of fitted series resistances obtained from 300 measured *I-U* curves without using additional series resistance with the PV module for different P_{MPP}-based cutting limits.

Limit (%)		Quantity (Ω)			
Left	Right	Mean	Median	St. deviation	IQR
40	60	0.8027	0.8033	0.0149	0.0217
	50	0.8086	0.8096	0.0165	0.0277
	40	0.8123	0.8181	0.0344	0.0566
30	60	0.8009	0.8015	0.0153	0.0220
	50	0.8066	0.8071	0.0176	0.0276
	40	0.8091	0.8176	0.0369	0.0617
20	60	0.7988	0.7997	0.0160	0.0231
	50	0.8042	0.8056	0.0195	0.0293
	40	0.8043	0.8163	0.0413	0.0679
10	60	0.7961	0.7973	0.0166	0.0233
	50	0.8000	0.8017	0.0238	0.0296
	40	0.7951	0.8138	0.0538	0.0846

Table 14. Basic statistical quantities of fitted series resistances obtained from 300 measured *I-U* curves using additional series resistance of 0.22 Ω with the PV module for different P_{MPP}-based cutting limits.

Limit (%)		Quantity (Ω)			
Left	Right	Mean	Median	St. deviation	IQR
40	60	1.0484	1.0488	0.0130	0.0190
	50	1.0541	1.0516	0.0112	0.0202
	40	1.0578	1.0560	0.0227	0.0349
30	60	1.0457	1.0462	0.0138	0.0211
	50	1.0514	1.0493	0.0119	0.0215
	40	1.0544	1.0530	0.0255	0.0419
20	60	1.0421	1.0423	0.0156	0.0229
	50	1.0479	1.0465	0.0135	0.0226
	40	1.0485	1.0490	0.0305	0.0510
10	60	1.0342	1.0354	0.0192	0.0276
	50	1.0394	1.0412	0.0191	0.0287
	40	1.0345	1.0439	0.0450	0.0793

Table 15. Basic statistical quantities for fitted series resistances obtained from 300 measured *I-U* curves using additional series resistance of 0.69 **Ω** with the PV module for different P_{MPP}-based cutting limits.

Limit (%)		Quantity (Ω)			
Left	Right	Mean	Median	St. deviation	IQR
40	60	1.5092	1.5088	0.0143	0.0222
	50	1.5132	1.5092	0.0130	0.0223
	40	1.5165	1.5160	0.0152	0.0232
30	60	1.5070	1.5072	0.0158	0.0251
	50	1.5115	1.5067	0.0141	0.0247
	40	1.5145	1.5151	0.0170	0.0252
20	60	1.5024	1.5035	0.0186	0.0267
	50	1.5076	1.5039	0.0160	0.0281
	40	1.5095	1.5126	0.0210	0.0298

Figs. 44-45 illustrate such cases where the left cutting limit is 20% and the right cutting limits are 60% and 50%, respectively. The interquartile ranges of the fitted R_s values in Fig. 44 are close to the case of having a symmetrical P_{MPP}-based cutting limit of 50% but are clearly larger in Fig. 45. The deviation increases even more if the cutting limit on the right side of the MPP is set to 40%. However, the average R_s values remain almost unchanged. When the left cutting limit is set to 10% for the severely aged module, the fitting algorithm occasionally produces complex numbers as the fitted parameter values.

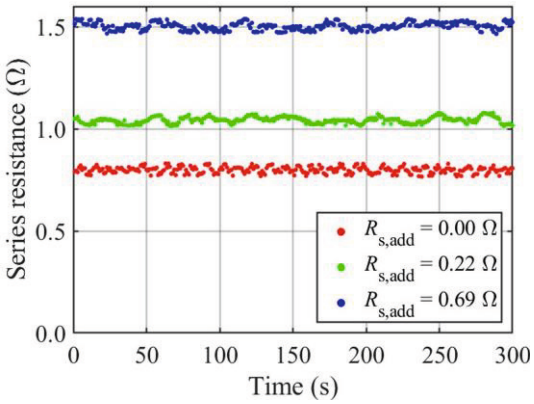

Figure 44. Identified series resistances during the 300-second *I-U* curve measurement periods for different cases of ageing by using a P_{MPP}-based cutting limit of 20% on the left side of MPP and 60% on the right side.

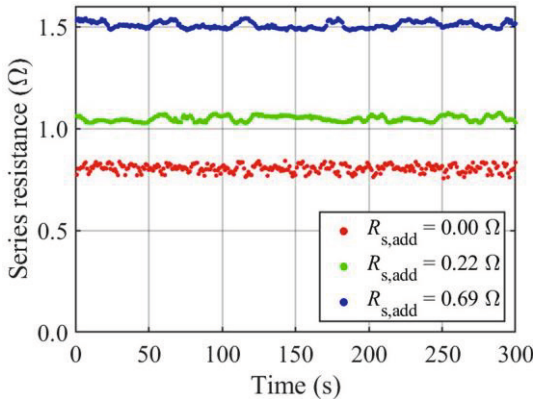

Figure 45. Identified series resistances during the 300-second *I-U* curve measurement periods for different cases of ageing by using a P_{MPP}-based cutting limit of 20% on the left side of MPP and 50% on the right side.

These results show that asymmetrical cutting emphasising the OC slope of the *I-U* curve can be used at least for finding the correct order of magnitude of series resistance. If exceptionally high R_s values are then identified, a more accurate diagnosis can be obtained by increasing the measurement range in the SC slope region of the *I-U* curve. It should be noted that emphasising the OC slope in fitting leads to the weakened fitting accuracy of the other single-diode model parameters. This, in turn, complicates the identification of irradiance.

8 DISCUSSION

The methods developed in this thesis are based on certain choices made during the research process. In the following, the most relevant of these choices are raised for discussion. The consequent motivation for considering alternative choices is based on the existing literature. As a result, interesting topics for future research are provided which could possibly help to further improve the proposed methodology.

The first observations are related to the formation of the initial guess values of parameter needed by the developed single-diode model fitting procedure. The parasitic resistances at STC calculated via the iterative procedure by Villalva et al. (2009) served as their initial guess for the first current-voltage curve of the dataset. Ayodele et al. (2016) reported that the Villalva algorithm is quite immune to changes in the initial guess values. This property justifies its usage in initialising the fitting procedure: even if the values of the SC current, OC voltage, MPP current, and MPP voltage at STC needed in the initialisation were not exactly known, the identified STC values for the parasitic resistances are not expected to change much. As a possible development idea, the modules do not have to be assumed to be in STC conditions at the beginning of the fitting procedure: the MPP tracking algorithm of the inverter finds the MPP current and voltage and the first initial guess for parasitic resistances could also be provided by using these values.

The initial guess for the photocurrent was calculated based on the ratio I_{MPP}/I_{SC}, which was assumed to be constant in this thesis. The used constant value was derived from experimentally determined values of MPP and SC currents at STC. The obtained constant (0.91) is in line with previous studies (Bastidas-Rodriguez et al., 2017a; Sera, 2010; Sera et al., 2011; Spagnuolo et al., 2019b; Wang et al., 2011). The observation by Spagnuolo et al. (2019b) that higher irradiance levels lead to larger differences in the I_{MPP}/I_{SC} ratio for different series resistance additions could be considered when applying the developed fitting procedure for PV module ageing detection in practice.

In contrast to the utilisation of the I_{MPP}/I_{SC} ratio in the present work, the proposed fitting procedure in its existing form does not make any assumptions

based on the ratio U_{MPP}/U_{OC}. This simplifies the procedure in the sense that U_{MPP}/U_{OC}, which is a decreasing function of irradiance and temperature and also depends on series resistance (Spagnuolo et al., 2019b), has a much larger dispersion than I_{MPP}/I_{SC}. If a fixed estimate were needed for U_{MPP}/U_{OC} in the proposed fitting procedure, the cumulation of the ageing and irradiance effects on the U_{MPP}/U_{OC} value would possibly lead to the presence of scarce errors in the estimate of U_{OC} and hence in the estimate of the PV module temperature. This situation has been avoided by introducing the irradiance-dependent formula for OC voltage in the expression of saturation current.

The second observations are related to the actual fitting procedure. The combined use of the formulae for the saturation current and OC voltage enables the consistent repetition of the PV module's operating temperature at all irradiance levels. This is in accordance with the findings by Boyd et al. (2011), who observed that I_o adjusts the predicted voltage at all points of the *I-U* curve: this observation has been emphasised by Nassar-Eddine et al. (2016). In turn, the correctly estimated OC voltage is directly linked to the fitted temperature value. Ibrahim and Anani (2017b) compared several conversion formulae in terms of performance and observed that the expression of saturation current depending on OC voltage is the most accurate of the compared methods. Moreover, Ibrahim and Anani (2017a) observed that the best results for the OC voltage are obtained when its irradiance and temperature dependencies are considered simultaneously. These observations further support the observations made during the present study.

The choice of ideality factor is perhaps an even more influential issue. Indeed, the actual ideality factor of the used PV module is not known, and this is also the case in the real-case PV applications. In this work, the ideality factor was set to 1.1. However, treating the ideality factor as a fixed constant is an obvious limitation in the usage of the proposed fitting procedure. The fitting procedure could be fine-tuned by removing the assumption of a constant ideality factor. Indeed, Ruschel et al. (2021) emphasised that although the majority of authors treat the ideality factor as a constant with respect to irradiance and temperature, there is no full consensus on this independence.

Considering these facts, the choice of the ideality factor is relevant, as its correctness affects the fit quality and the reliability of the diagnosis. This gives rise to new research questions, such as finding the actual ideality factor of the PV module or the introduction of a non-constant ideality factor in the proposed fitting procedure. The latter issue could be addressed by using a conversion formula for the ideality factor, or possibly tuning the fitting procedure so that the ideality factor

is one of the fitted parameters. However, adding a new fitting parameter complicates the fitting procedure considerably.

The third observations are related to the ageing detection of the proposed fitting procedure based on series resistance. Piliougine et al. (2021) analysed the capability of four explicit single-diode model parameter identification methods to detect ageing and degradation. They found that the *SPR* method did not detect degradation when series resistance is low. Piliougine et al. (2021) also found that the Lambert *W* function based method always underestimated the changes in series resistance, which became even worse for higher additional resistances. In this light, Lambert *W* based methods are not the best choice for highly degraded PV modules. The iterative identification method provided in this thesis also slightly underestimated the change in series resistance, as observed in Kalliojärvi et al. (2022). However, Lappalainen et al. (2022a) showed that such an underestimation originates from the root mean square error (RMSE) based minimisation in terms of current and could be corrected by the introduction of the voltage as the quantity to be minimised. Indeed, Hao et al. (2021) emphasised that the current-based approach, although the most common choice, does not entirely account for the deviation between the fitted and measured *I-U* curves; the measurement errors of each measurement point concern the voltage as well as the current. The minimisation of RMSE in terms of voltage could be a further improvement for the present work.

The positive temperature dependence of series resistance is a phenomenon recognised in the analysis of the present study as well as in the existing literature (Piliougine et al., 2020; Humada et al., 2016; van Dyk and Meyer, 2004). In addition, the temperature dependence of series resistance at the beginning of the PV module's lifespan and after 8 operational years in was investigated in Hrelja et al. (2018) via a linear model. The slope of the line showing the series resistance as a function of temperature exhibited no considerable changes in terms of time. In contrast, Ibrahim and Anani (2017b) stated that series resistance has only little sensitivity to changes in temperature. Attivissimo et al. (2012) provided an uncertainty analysis in PV cell parameter estimation by using the double-diode model. The authors considered series resistance to be invariant regardless of operating conditions. However, the fitting procedure developed in this thesis exhibits a slight positive temperature dependence which must be taken into account in real-case applications. One interesting topic for future research is to find out the temperature coefficient of series resistance of the PV module used in this work.

An important aspect is the stability of the fitting procedure for differently aged PV modules. Guejia-Burbano et al. (2021) observed that their procedure provides stable parameters for a healthy PV module, whereas the parameters deviate in the case of a PV module with degraded series resistance. The results presented in this thesis show that the series resistance detection performs well for non-aged and aged PV modules. This is a certain advantage which enhances the usability of the proposed fitting procedure in real-case ageing detection.

The fourth observations are related to the overall performance of the fitting procedure. The accuracy of the fitted parameters is definitely a measure of the performance of any fitting procedure. Humada et al. (2016) emphasised that the accuracy of a fitting procedure depends on the actual fitting algorithm, but also the initial guess and the confidence interval of the parameters affect. In addition, the accuracy of a PV model is also affected by the dataset, the number of selected parameters, and their accuracy (Humada et al., 2020). However, Ayodele et al. (2016) remarked that no model is absolutely the most accurate; it depends on the identified parameter in question. In addition, the authors pointed out that the identification performance of the single-diode model is too often compared only based on the model accuracy. However, other relevant metrics include the robustness of the algorithm, computational speed, memory requirement, and ease of implementation (Ayodele et al., 2016). Humada et al. (2020) highlighted that regardless of the PV model under investigation, the accuracy and complexity of a model, including the number of fitting parameters, should be considered as a whole. In light of this discussion, it would be interesting to compare the accuracy of the obtained parameters and the overall performance of the proposed procedure to the two procedures (Lappalainen et al., 2020; Lappalainen et al., 2022a) that can identify the operating irradiance and temperature jointly with the single-diode model parameters.

The fifth observation is related to the quality and amount of the measurement data. Indeed, Mellit et al. (2018) pointed out that the measurement accuracy is a significant part of the effectiveness of a monitoring system. The authors highlighted that inverters fail to produce accurate measurement data. This might be a challenge when performing diagnosis based on *I-U* curves measured by inverter instead of specific *I-U* curve tracers. The quality of the measurement data is also expected to affect the need to pre-process the data and the choice of a suitable pre-processing procedure. It would be interesting to investigate the performance of the developed fitting procedure by using current-voltage measurement data produced by an inverter instead of an *I-U* curve tracer.

Remarkably, the fitting procedure was tested only by using an individual PV module, while Lappalainen et al. (2020; 2022a) tested their developed fitting procedures with different PV modules.

9 CONCLUSIONS

This thesis focused on showing the functionality of the developed novel single-diode model fitting procedure for current-voltage curves measured from a PV system. The main emphasis was on investigating the parameter identification capabilities of the developed fitting procedure for online analyses of the PV system and ageing detection. The procedure was developed in a stepwise manner. Firstly, a pre-processing procedure for measured current-voltage curves was developed. Secondly, a suitable theory for developing the single-diode model fitting was sought, whereafter the actual model was developed. Thirdly, the functionality of the developed single-diode model fitting procedure was demonstrated for the measured current-voltage curves of a PV module. Fourthly, the fitted parameters were converted into reference conditions to obtain comparable results. Fifthly, the effects on the fitted parameters were investigated when the measurement range of the current-voltage curves was limited to the vicinity of the MPP. The main focus was on developing a method for fitting the single-diode model to the measured *I-U* curves of a PV module and verifying its functionality, especially for online ageing detection based on the determined series resistance.

The pre-processing of measured current-voltage curves was implemented by using a statistical method, the application of which was accompanied by a suitable reconstruction of points used for fitting. The developed pre-processing procedure eliminated the measurement noise and other abnormal measurement points as desired. In addition, the unintentional weighting of measurement points caused by the measurement device was effectively removed by using the representative point approach developed for this thesis. The developed pre-processing procedure can be applied for current-voltage curves obtained by any commercial current-voltage curve tracer following a similar operating principle.

An appropriate approach to constructing a single-diode model fitting procedure with the desired capability to identify the operating conditions was observed to be one with iterative equations and a small number of direct fitting parameters. Indeed, no approximate explicit equations were used. There were only

four direct fitting parameters, which enhanced the convergence towards the correct solution.

The developed single-diode model fitting procedure identified the PV module's operating irradiance and temperature well, especially when the PV module was operating under high irradiance conditions. Hence, there is no need for external measurements of operating conditions at practical PV sites. The reliable identification of operating conditions enables the classification of the measured current-voltage curves based on the operating conditions, i.e., whether an individual curve can be used in diagnosis or not. It was observed that the entire developed single-diode model performs best in stable high irradiance conditions. This was an expected result.

The performance of the fitting procedure with respect to each single-diode model parameter was separately analysed by using entire measured current-voltage curves. Series resistance identification performed in a stable way under high irradiance conditions, whereas low irradiance conditions produced excessively high values that deviated strongly. As expected, shunt resistance values identified under high irradiance conditions lay above a certain threshold and varied relatively widely but around a nearly constant mean value. Low irradiance conditions gave rise to excessively high shunt resistance values as was anticipated. Photocurrent was identified correctly in all irradiance conditions, increasing linearly with irradiance. Series resistance and photocurrent had slight positive temperature dependences.

The effect of the operating conditions on the fitted parameters was eliminated by converting the parameters to Standard Test Conditions. Widely used formulae from the literature were exploited for that purpose. It was observed that photocurrent and parasitic resistances obtained from entire measured curves at high irradiance conditions remained nicely within a narrow range when converted to STC. In contrast, the conversion applied to the parameters obtained at low irradiance conditions performed improperly as expected.

The effect of limiting the measurement range of current-voltage curves to the vicinity of the MPP for fitting the single-diode model parameters was systematically studied for the developed fitting procedure. It was found that the cutting limit clearly affects the accuracy of the parameters. A significant observation was that appropriately chosen partial current-voltage curves can be well-used to identify the parameters of the single-diode model. It was found that the current-voltage curves could be cut in different ways to identify the series resistance. Symmetrical cutting with respect to the MPP power performed well when at least half of the power-voltage curve was measured for fitting. However,

symmetrical cutting with respect to the MPP voltage performed much more weakly and is not an accurate choice for ageing detection. It was also found that the curve does not necessarily need to be cut symmetrically with respect to the MPP if the focus is determining the series resistance. Indeed, the MPP power-based cutting principle was also investigated by setting different cutting limits on either side of the MPP. Some examples of such cutting were shown to be suitable for series resistance identification. Such a choice helps to avoid unnecessary measurements in the high-current region of the current-voltage curve, but naturally this happens at the expense of the accuracy of determining other parameters. However, further research is needed in order to find practically applicable solutions.

The methods developed in this thesis provide a theoretical and practical background for designing a full online condition monitoring approach for ageing detection of PV systems. The obtained results also serve as a reference for future works.

REFERENCES

J. Accarino, G. Petrone, C.A. Ramos-Paja, and G. Spagnuolo. "Symbolic algebra for the calculation of the series and parallel resistances in PV module model". In: Proceedings of International Conference on Clean Electric Power, pp. 62-66, 2013.

J. Ahmad, A. Ciocia, S. Fichera, A.F. Murtaza, and F. Spertino. "Detection of typical defects in silicon photovoltaic modules and application for plants with distributed MPPT configuration". Energies, vol. 12(23), 4547, 2019.

N. Anani, and H. Ibrahim. "Adjusting the single-diode model parameters of a photovoltaic module with irradiance and temperature". Energies, vol. 13(12), 3226, 2020.

F. Attivissimo. A. Di Nisio, M. Savino, and M. Spadavecchia. "Uncertainty analysis in photovoltaic cell parameter estimation". IEEE Transactions on Instrumentation and Measurement, vol. 61(5), pp. 1334-1342, 2012.

T.R. Ayodele, A.S.O. Ogunjuyigbe, and E.E. Ekoh. "Evaluation of numerical algorithms used in extracting the parameters of a single-diode photovoltaic model". Sustainable Energy Technologies and Assessments, vol. 13, pp. 51-59, 2016.

A. Azizi, P. Logerais, A. Omeiri, A. Amiar, A. Charki, O. Riou, F. Delaleux, and. J. Durastanti. "Impact of the aging of a photovoltaic module on the performance of a grid-connected system". Solar Energy, vol. 174, pp. 445-454, 2018.

J.D. Bastidas-Rodriguez, E. Franco, G. Petrone, C.A. Ramos-Paja, and G. Spagnuolo. "Model-based degradation analysis of photovoltaic modules through series resistance estimation". IEEE Transactions on Industrial Electronics, vol. 62(11), pp. 7256-7265, 2015.

J.D. Bastidas-Rodriguez, E. Franco, G. Petrone, C.A. Ramos-Paja, and G. Spagnuolo. "Quantification of photovoltaic module degradation using model based indicators". Mathematics and Computers in Simulation, vol. 131, pp. 101-113, 2017a.

J.D. Bastidas-Rodriguez, G. Petrone, C.A. Ramos-Paja, and G. Spagnuolo. "A genetic algorithm for identifying the single diode model parameters of a photovoltaic panel". Mathematics and Computers in Simulation, vol. 131, pp. 38-54. 2017b.

E. Batzelis. "Non-iterative methods for the extraction of the single-diode model parameters of photovoltaic modules: a review and comparative assessment". Energies, vol. 12(3), 358, 2019.

E. Batzelis, G. Anagnostou, C. Chakraborty, and B. Pal. "Computation of the Lambert W function in photovoltaic modeling". In: ELECTRIMACS 2019, Springer, Cham, pp. 583-595, 2020.

J.M. Blanes, F.J. Toledo, S. Montero, and A. Garrigós. "In-site real-time photovoltaic I-V curves and maximum power point estimator". IEEE Transactions on Power Electronics, vol. 28(3), pp. 1234-1240, 2012.

R.E. Campos, E.Y. Sako, M.V.G. dos Reis, and M.G. Villalva. "A review of the main methods to trace the I-V characteristic curve of PV sources". In: 13th IEEE International Conference on Industry Applications, pp. 24-30, 2018.

S. Cannizzaro, M.C. Di Piazza, M. Luna, and G. Vitale. "Generalized classification of PV modules by simplified single-diode models". In: IEEE 23rd International Symposium on Industrial Electronics, pp. 2266-2273, 2014.

C. Carrero, D. Ramirez, J. Rodriguez, and R. Castillo-Sierra. "Sensitivity analysis of loss resistances variations of PV generators applied to the assessment of maximum power point changes due to degradation". Renewable Energy, vol. 173, pp. 351-361, 2021.

Y. Chaibi, A. Allouhi, M. Malvoni, M. Salhi, and R. Saadani. "Solar irradiance and temperature influence on the photovoltaic cell equivalent-circuit models". Solar Energy, vol. 188, pp. 1102-1110, 2019.

T. Chayavanich, C. Limsakul, N. Chayavanich, D. Chevindhya, C. Jivacate, and K. Kirtikara. "Describing dynamic behavior of static IV characteristics of PV modules using dynamic impedance". In: 21st European Photovoltaic Solar Energy Conference, Dresden, Germany, pp. 4-8, 2006.

D. Chen, and S. Zhang. "A novel initial value prediction of curve-fitting algorithm for single-diode model of photovoltaic modules". In: IOP Conference Series: Earth and Environmental Science, vol. 632(3), p. 032060, 2021.

V.J. Chin, and Z. Salam. "A new three-point-based approach for the parameter extraction of photovoltaic cells". Applied Energy, vol. 237, pp. 519-533, 2019.

A.W. Copeland, O.D. Black, and A.B. Garrett. "The photovoltaic effect". Chemical Reviews, vol. 31(1), pp. 177-226, 1942.

W. De Soto, S.A. Klein, and W.A. Beckman. "Improvement and validation of a model for photovoltaic array performance". Solar Energy, vol. 80(1), pp. 78-88, 2006.

M.C. Di Piazza, M. Luna, G. Petrone, and G. Spagnuolo. "About the identification of the single-diode model parameters of high-fill-factor photovoltaic modules". In: International Conference on Clean Electrical Power, pp. 85-91, 2015.

T. Dittrich. Materials concepts for solar cells. World Scientific Publishing, Helmholz, Germany, 2015.

S.A.A. dos Santos, J.P.N. Torres, C.A. Fernandez, and R.A.M. Lameirinhas. "The impact of aging of solar cells on the performance of photovoltaic panels". Energy Conversion and Management: X, 11, 100082, 2021.

E. Durán, M. Piliougine, M. Sidrach-de-Cardona, J. Galán, and J.M. Andujar. "Different methods to obtain the I-V curve of PV modules: a review". In: 33rd IEEE Photovoltaic Specialists Conference, pp. 1-6, 2008a.

E. Durán, M. Sidrach-de-Cardona, J. Galán, and J.M. Andújar. "Comparative analysis of buck-boost converters used to obtain I-V characteristic curves of photovoltaic modules". In: IEEE Power Electronics Specialists Conference. pp. 2036-2042, IEEE, 2008b.

Energy Information Administration. "Renewable energy explained". https://www.eia.gov/energyexplained/renewable-sources/, 2022.

J.M. Enrique, E. Durán, M. Sidrach-de-Cardona, J.M. Andújar, M.A. Bohórquez, and J. Carretero. "A new approach to obtain I-V and P-V curves of photovoltaic modules using DC-DC converters". In: Conference Record of the Thirty-first IEEE Photovoltaic Specialists Conference, pp. 1769-1772, 2005.

S. Fadhel, C. Delpha, D. Diallo, I. Bahri, A. Migan, M. Trabelsi, and M.F. Mimouni. "PV shading fault detection and classification based on I-V curve using principal component analysis: Application to isolated PV system". Solar Energy, vol. 179, pp. 1-10, 2019.

C.A.F. Fernandes, J.P.N. Torres, M. Morgado, and J.A.P. Morgado. "Aging of solar PV plants and mitigation of their consequences". In: IEEE International Power Electronics and Motion Control Conference, pp. 1240-1247, 2016.

T. Finsterle, L. Černá, P. Hrzina, D. Rokusek, and V. Benda. "Diagnostics of PID early stage in PV systems". Energies, vol. 14(8), 2155, 2021.

L.M. Fraas, and L.D. Partain. Solar cells and their applications. John Wiley & Sons, Hoboken, 2010.

Fraunhofer Institute for Solar Energy Systems, Photovoltaics report. Freiburg, 22 September 2022.

A. Garrigós, J.M. Blanes, J.A. Carrasco, and J.B. Ejea. "Real time estimation of photovoltaic modules characteristics and its application to maximum power point operation". Renewable Energy, vol. 32, pp. 1059-1076, 2007.

F. Ghani, and M. Duke. "Numerical determination of parasitic resistances of a solar cell using the Lambert W-function". Solar Energy, vol. 85, pp. 2386-2394, 2011.

M.A. Green, E.D. Dunlop, J. Hohl-Ebinger, M. Yoshita, N. Kopidakis, K. Bothe, D. Hinken, M. Rauer, and X. Hao. "Solar cell efficiency tables (Version 60)". Progress in Photovoltaics: Research and Applications, vol. 30, pp. 687-701, 2022.

R.A. Guejia-Burbano, G. Petrone, and P. Manganiello. "Early detection of photovoltaic panel degradation through artificial neural network". Applied Sciences, vol. 11(19), 8943, 2021.

R. Guerrero-Lemus, and J.M. Martinez-Duart. "Biomass". In: Renewable Energies, and CO_2, pp. 37-62, Springer, London, 2012.

O. Hachana, K.E. Hemsas, and G.M. Tina. "Comparison of different metaheuristic algorithms for parameter identification of photovoltaic cell/module". Journal of Renewable and Sustainable Energy, vol. 5(5), 053122, 2013.

P. Hao, Y. Zhang, H. Lu, and Z. Lang. "A novel method for parameter identification and performance estimation of PV module under varying operating conditions". Energy Conversion and Management, vol. 247, 114469, 2021.

N. Hrelja, M. van Iseghem, E. Lajoie-Mazenc, E. Moulines, and E. Vernet. "Single diode model applied to PV module aging". In 35th European Photovoltaic Solar Energy Conference and Exhibition, pp. 1290-1293, 2018.

A.M. Humada, S.Y. Darweesh, K.G. Mohammed, M. Kamil, S.F. Mohammed, N.K. Kasim, T.A. Tahseen, O.I. Awad, and S. Mekhilef. "Modeling of PV system and parameter extraction based on experimental data: review and investigation". Solar Energy, vol. 199, pp. 742-760, 2020.

A.M. Humada, M. Hojabri, S. Mekhilef, and H.M. Hamada. "Solar cell parameters extraction based on single and double-diode models: A review". Renewable and Sustainable Energy Reviews, vol. 56, pp. 494-509, 2016.

H. Häberlin. Photovoltaics: System design and practice. John Wiley & Sons, Chichester, 2012.

H. Ibrahim, and N. Anani. "Evaluation of analytical methods for parameter extraction of PV modules". Energy Procedia, vol. 134, pp. 69-78, 2017a.

H. Ibrahim, and. N. Anani. "Variations of PV module parameters with irradiance and temperature". Energy Procedia, vol. 134, pp. 276-285, 2017b.

International Energy Agency. "Global energy review 2021", https://www.iea.org/reports/global-energy-review-2021/renewables, 2021.

International Renewable Energy Agency. "Renewable capacity statistics 2022", Abu Dhabi, www.irena.org/Publications, 2022.

D.C. Jordan, T.J. Silverman, J.H. Wohlgemuth, S.R. Kurtz, and K.T. VanSant. "Photovoltaic failure and degradation modes". Progress in Photovoltaics: Research and Applications, vol. 25(4), pp. 318-326, 2017.

A.R. Jordehi. "Parameter estimation of solar photovoltaic PV cells: A review." Renewable and Sustainable Energy Reviews, vol. 61, pp. 354-351, 2016.

M. Järvelä, K. Lappalainen, and S. Valkealahti. "Characteristics of the cloud enhancement phenomenon and PV power plants". Solar Energy, vol. 196, pp. 137-145, 2020.

P. Kala, P. Joshi, S. Agrawal, L.K. Yadav, and M. Joshi. "Introduction to condition monitoring of PV system". In: Soft Computing in Condition Monitoring and Diagnostics of Electrical and Mechanical Systems, Springer, Singapore, pp. 169-187, 2020.

H. Kalliojärvi, K. Lappalainen, and S. Valkealahti. "Feasibility of photovoltaic module single-diode model fitting to the current-voltage curves measured in the vicinity of the maximum power point for online condition monitoring purposes." Energies, vol. 15(23), 9079, 2022.

H. Kalliojärvi-Viljakainen, K. Lappalainen, and S. Valkealahti. "A novel procedure for identifying the parameters of the single-diode model and the operating conditions of a photovoltaic module from measured current-voltage curves". Energy Reports, vol. 8, pp. 4633-4640, 2022.

H. Kalliojärvi-Viljakainen, K. Lappalainen, and S. Valkealahti. "Preprocessing of PV panel measured current-voltage characteristics before curve fitting". Proceedings of 47th IEEE Photovoltaic Specialists Conference, pp. 0117-0123, 2020a.

H. Kalliojärvi-Viljakainen, K. Lappalainen, and S. Valkealahti. "Fitting procedure for PV panel measured current-voltage characteristics". In: Proceedings of 37th European Photovoltaic Solar Energy Conference and Exhibition, pp. 1506-1511, 2020b.

H. Kalliojärvi-Viljakainen, G. Spagnuolo, and S. Valkealahti. "Identification of series resistance from the measured PV panel electrical characteristics". In: Proceedings of 36th European Photovoltaic Solar Energy Conference and Exhibition, Marseille, France, pp. 1593-1599, 2019.

E. Kaplani. "Detection of degradation effects in field-aged c-Si solar cells through IR thermography and digital image processing". International Journal of Photoenergy, vol. 2012, 396792, 2012.

S.T. Kebir, N. Cheggaga, M.S. Ait Cheikh, M. Haddadi, and H. Rahmani. "A comprehensive study of diagnosis faults techniques occurring in photovoltaic generators". Engineering Review, vol. 41(3), pp. 124-141, 2021.

C. Kittel. "Introduction to solid state physics". 8th ed., John Wiley & Sons, Singapore, 2005.

E. Kouadri-Boudjelthia, F. Chekired, N. Belhaouas, Z. Smara, and F. Mehareb. "Bubbles formation on the photovoltaic cells fingers: Visual inspection of 30-year-old modules". Solar Energy, vol. 230, pp. 1013-1019, 2021.

J.A. Kratochvil, W.E. Boyson, and D.L. King. "Photovoltaic Array Performance Model (No. SAND2004-3535)". Sandia National Laboratories, 2004.

A. Lannoy, and H. Procaccia. Evaluation et maîtrise du vieillissement industriel. Edition Lavoisier, Paris, 2005.

K. Lappalainen, P. Manganiello, M. Piliougine, G. Spagnuolo, and S. Valkealahti. "Virtual sensing of photovoltaic module operating parameters". IEEE Journal of Photovoltaics, vol. 10(3), pp. 852-862, 2020.

K. Lappalainen, M. Piliougine, and G. Spagnuolo. "Experimental comparison between various fitting approaches based on RMSE minimization for photovoltaic module parametric identification". Energy Conversion and Management, vol. 258, 115526, 2022a.

K. Lappalainen, and S. Valkealahti. "Experimental observations about the cloud enhancement phenomenon on PV strings." In: 8th World Conference on Photovoltaic Energy Conversion, pp. 1354-1358, 2022b.

K. Lappalainen, and S. Valkealahti. "Experimental study of the maximum power point characteristics of partially shaded photovoltaic strings". Applied Energy, vol. 301, 117436, 2021.

A. Laudani, F.R. Fulginei, and A. Salvini. "High performing extraction procedure for the one-diode model of a photovoltaic panel from experimental *I-V* curves by using reduced forms". Solar Energy, vol. 103, pp. 316-326, 2014.

V. Leite, F. Chenlo, and J. Afonso. "Low-cost instrument for tracing current-voltage characteristics of photovoltaic modules". In: International Conference on Renewable Energies and Power Quality, Santiago de Compostela, Spain, pp. 1012-1017, 2012.

L. Lillo-Sánchez, G. López-Lara, J. Vera-Medina, E. Pérez-Aparicio, and I. Lillo-Bravo. "Degradation analysis of photovoltaic modules after operating for 22 years. A case study with comparisons". Solar Energy, vol. 222, pp. 84-94, 2021.

J. Lindroos, and H. Savin. "Review of light-induced degradation in crystalline silicon solar cells". Solar Energy Materials & Solar Cells, vol. 147, pp. 115-126, 2016.

A. Luque, and S. Hegedus (ed). Handbook of photovoltaic science and engineering. John Wiley & Sons, Chichester, 2003.

M.M. Mahmoud. "Transient analysis of a PV power generator charging a capacitor for measurement of the I-V characteristics". Renewable Energy, vol. 31, pp. 2198-2206, 2006.

P. Manganiello, M. Balato, and M. Vitelli. "A survey on mismatching and aging of PV modules: The closed loop". IEEE Transactions on Industrial Electronics, vol. 62(11), pp. 7276-7286, 2015.

B. Marion. "A method for modeling the current-voltage curve of a PV module for outdoor conditions". Progress in Photovoltaics: Research and Applications, vol. 10, pp. 205-214, 2002.

D.L. Meier, and D.K. Schroder. "Contact resistance: Its measurement and relative importance to power loss in a solar cell". IEEE Transactions on Electron Devices, vol. 31(5), pp. 647-653, 1984.

A. Mellit, G.M. Tina, and S.A. Kalogirou. "Fault detection and diagnosis methods for photovoltaic systems: A review". Renewable and Sustainable Energy Reviews, vol. 91, pp. 1-17, 2018.

Y. Meng, Z. Chen, H. Cheng, E. Wang, and B. Tan. "An efficient variable step solar maximum power point tracking algorithm". Energies, vol. 16, 1299, 2023.

E.L. Meyer. "Extraction of saturation current and ideality factor from measuring V_{oc} and I_{sc} of photovoltaic modules". International Journal of Photoenergy, vol. 2017, 8479487, 2017.

R.A. Millikan. "A direct determination of *h*". Physical Review, vol. 4(1), pp. 73-75, 2014.

A. Mäki. Effects of partial shading conditions on maximum power points and mismatch losses in silicon-based photovoltaic power generators. Doctoral thesis, Tampere University of Technology, 2013.

I. Nassar-Eddine, A. Obbadi, Y. Errami, A. El Fajri, and M. Agunaou. "Parameter estimation of photovoltaic modules using iterative method and the Lambert W function: A comparative study". Energy Conversion and Management, vol. 119, pp. 37-48, 2016.

National Aeronautics and Space Administration. "Earth's energy budget". https://earthobservatory.nasa.gov/features/EnergyBalance/page4.php, 2009.

A. Ndiaye, C.M.F. Kébé, A. Charki, P.A. Ndiaye, V. Sambou, and A. Kobi. "Degradation evaluation of crystalline-silicon photovoltaic modules after a few operation years in a tropical environment". Solar Energy, vol. 103, pp. 70-77, 2014.

M. Niaz, S. Klassen, B. McMillan, and D. Metz. "Reconstruction of the history of the photoelectric effect and its implications for general physics textbooks". Science Education, vol. 94(5), pp. 903-931, 2010.

D. Nilsson. Fault detection in photovoltaic systems. Master's thesis, Kungliga Tekniska Högskolan, 2014.

Nuclear Power. "How much energy does the world consume?", https://www.nuclear-power.com/how-much-energy-does-the-world-consume/, 2023.

T.A. Pereira, L. Schmitz, W.M. dos Santos, D.C. Martins, and R.F. Coelho. "Design of a portable photovoltaic I-V curve tracer based on the DC-DC converter method.". IEEE Journal of Photovoltaics, vol. 11(2), pp. 552-560, 2021.

G. Petrone, M. Luna, G. La Tona, M.C. Di Piazza, and G. Spagnuolo. "Online identification of photovoltaic source parameters by using a genetic algorithm". Applied Sciences, vol. 8(1), 9, 2017a.

G. Petrone, C.A. Ramos-Paja, and G. Spagnuolo. Photovoltaic sources modeling. John Wiley & Sons, Hoboken, 2017b.

M. Piliougine, R.A. Guejia-Burbano, G. Petrone, F.J. Sánchez-Pacheco, L. Mora-López, and M. Sidrach-de-Cardona. "Parameters extraction of single diode model

for degraded photovoltaic modules". Renewable Energy, vol. 164, pp. 674-686, 2021.

M. Piliougine, G. Spagnuolo, and M. Sidrach-de-Cardona. "Series resistance temperature sensitivity in degraded mono-crystalline silicon modules". Renewable Energy, vol. 162, pp. 677-684, 2020.

F. Prieto-Castrillo, N. Núñez, and M. Vázquez. "Warranty assessment of photovoltaic modules based on a degradation probabilistic model". Progress in Photovoltaics: Research and Applications, vol. 28(12), pp. 1308-1321, 2020.

PV Magazine, "World has installed 1TW of solar capacity", https://www.pv-magazine.com/2022/03/15/humans-have-installed-1-terawatt-of-solar-capacity/, 15 March 2022.

D.A. Quansah, M.S. Adaramola, G. Takyi, and I.A. Edwin. "Reliability and degradation of solar PV modules – Case study of 19-year-old polycrystalline modules in Ghana". Technologies, vol. 5(2), 22, 2017.

D.A. Quansah, and M.S. Adaramola. "Ageing and degradation in solar photovoltaic modules installed in northern Ghana". Solar Energy, vol. 173, pp. 834-847, 2018.

A.B. Rabii, M. Jraidi, and A.S. Bouazzi. "Investigation of the degradation in field-aged photovoltaic modules". In: Proceedings of IEEE 3rd World Conference on Photovoltaic Energy Conversion, vol. 2, pp. 2004-2006, 2003.

M.R. Rashel, A. Albino, T. Gonçalves, and. M. Tlemcani. "Sensitivity analysis of parameters of a photovoltaic cell under different conditions". In: 10th International Conference on Software, Knowledge, Information Management & Applications, pp. 333-337, 2016.

M.B.H. Rhouma, A. Gastli, L.B. Brahim, F. Touati, and M. Benammar. "A simple method for extracting the parameters of the PV cell single-diode model". Renewable Energy, vol. 113, pp. 885-894, 2017.

C.S. Ruschel, F.P. Gasparin, and A. Krenzinger. "Experimental analysis of the single-diode model parameters dependence on irradiance and temperature". Solar Energy, vol. 217, pp. 134-144, 2021.

P. Sanchez-Friera, M. Piliougine, J. Peláez, J. Carretero, and M. Sidrach de Cardona. Analysis of degradation mechanisms of crystalline silicon PV modules after 12 years of operation in Southern Europe. Progress in Photovoltaics: Research and Applications, vol. 19, pp. 658-666, 2011.

D.K. Schroder. Semiconductor material and device characterization. John Wiley & Sons, Hoboken, 1998.

D. Sera. "Series resistance monitoring for photovoltaic modules in the vicinity of MPP". In: Proceedings of the 25th European Photovoltaic Solar Energy Conference and Exhibition, pp. 4506-4510, 2010.

D. Sera, L. Mathe, T. Kerekes, and R. Teodorescu. "A low-disturbance diagnostic function integrated in the PV arrays' MPPT algorithm". In: 37th Annual Conference of the IEEE Industrial Electronics Society, pp. 2456-2460, 2011.

D. Sera, and R. Teodorescu. "Robust series resistance estimation for diagnostics of photovoltaic modules". In: 35th Annual Conference of IEEE Industrial Electronics, pp. 800-805, 2009.

D. Sera, R. Teodorescu, and P. Rodriguez. "Photovoltaic module diagnostics by series resistance monitoring and temperature and rated power estimation". In: Proceedings of 34th Annual Conference of IEEE Industrial Electronics, pp. 2195-2199, 2008.

R. Singh, M. Sharma, R. Rawat, and C. Banerjee. "An assessment of series resistance estimation techniques for different silicon based SPV modules". Renewable and Sustainable Energy Reviews, vol. 98, pp. 199-216, 2018.

A. Sinha, O.S. Sastry, and R. Gupta. "Nondestructive characterization of encapsulant discoloration effects in crystalline-silicon PV modules". Solar Energy Materials & Solar Cells, vol. 155, pp. 234-242, 2016.

E. Skoplaki, and J.A. Palyvos. "On the temperature dependence of photovoltaic module electrical performance: A review of efficiency/power correlations". Solar Energy, vol. 83, pp. 614-624, 2009.

Solar Power Europe, "Global market outlook for solar power 2018-22", https://resources.solarbusinesshub.com/solar-industry-reports/item/global-market-outlook-2018-2022, June 2018.

B. Sopori, P. Basnyat, S. Devayajanam, S. Shet, V. Mehta, J. Binns, and J. Appel. "Understanding light-induced degradation of c-Si solar cells". In: 38th IEEE Photovoltaic Specialists Conference, pp. 001115-001120, 2012.

G. Spagnuolo, K. Lappalainen, S. Valkealahti, and P. Manganiello. "Identification and diagnosis of a photovoltaic module based on outdoor measurements". In: Milan Power-Tech, pp. 1-6, 2019a.

G. Spagnuolo, K. Lappalainen, S. Valkealahti, and P. Manganiello. "Photovoltaic module parametric identification". In: International Conference on Clean Electrical Power, pp. 302-305, 2019b.

S. Spataru, D. Sera, T. Kerekes, and R. Teodorescu. "Monitoring and fault detection in photovoltaic systems based on inverter measured string I-V curves". In: 31st European Photovoltaic Solar Energy Conference and Exhibition. WIP Wirtschaft und Infrastruktur GmbH & Co Planungs KG; pp. 1667-1674, 2015.

F. Spertino, J. Ahmad, A. Ciocia, P. Di Leo, A.F. Murtaza, and M. Chiaberge. "Capacitor charging method for I-V curve tracer and MPPT in photovoltaic systems". Solar Energy, vol. 119, pp. 461-473, 2015.

V. Stornelli, M. Muttillo, T. de Rubeis, and I. Nardi. "A new simplified five-parameter estimation method for single-diode model of photovoltaic panels". Energies, vol. 12(22), 4271, 2019.

X. Sun, R.V.K. Chavali, and M.A. Alam. "Real-time monitoring and diagnosis of photovoltaic system degradation only using maximum-power-point-the Suns-Vmp method". Progress in Photovoltaics: Research and Applications, vol. 27, pp. 55-66, 2019.

V. Tan, P.R. Dias, N. Chang, and R. Deng. "Estimating the lifetime of solar photovoltaic modules in Australia". Sustainability, vol. 14(9), 5336, 2022.

G.M. Tina, F. Cosentino, and C. Ventura. "Monitoring and diagnostics of photovoltaic power plants". In: Sayigh, A. (ed) Renewable Energy in the Service of Mankind Vol. II: Selected Topics from the World Renewable Energy Congress 2014. Springer, Cham, pp. 505-516, 2016.

F.J. Toledo, and J.M. Blanes. "Analytical and quasi-explicit four arbitrary point method for extraction of solar cell single-diode model parameters". Renewable Energy, vol. 92, pp. 346-356, 2016.

F.J. Toledo, J.M. Blanes, A. Garrigós, and J.A. Martínez. "Analytical resolution of the electrical four-parameters model of a photovoltaic module using small perturbation around the operating point". Renewable Energy, vol. 43, pp. 83-89, 2012.

D. Torres Lobera, A. Mäki, J. Huusari, K. Lappalainen, T. Suntio, and S. Valkealahti. "Operation of TUT solar PV power station research plant under partial shading caused by snow and buildings". Photovoltaics Materials and Devices, vol. 2013, 837310, 2013a.

D. Torres Lobera, and S. Valkealahti. "Dynamic thermal model of solar PV systems under varying climatic conditions". Solar Energy, vol. 93, pp. 183-194, 2013b.

D. Torres Lobera, and S. Valkealahti. "Inclusive dynamic thermal and electric simulation model of solar PV systems under varying atmospheric conditions". Solar Energy, vol. 105, pp. 632-647, 2014.

United Nations, "What is climate change?" https://www.un.org/en/climatechange/what-is-climate-change, accessed 5 March 2023.

E.E. van Dyk, and E.L. Meyer. "Analysis of the effect of parasitic resistances on the performance of photovoltaic modules". Renewable Energy, vol. 29, pp. 333-344, 2004.

A. Vega, V. Valiño, E. Conde, A. Ramos, and P. Reina. "Double-sweep tracer for I-V curves characterization and continuous monitoring of photovoltaic facilities". Solar Energy, vol. 190, pp. 622-629, 2019.

R.G. Vieira, F.M.U de Araújo, M. Dhimish, and M.I.S. Guerra. "A comprehensive review on bypass diode application on photovoltaic modules". Energies, vol. 13, 2472, 2020.

M.G. Villalva, J.R. Gazoli, and E.R. Filho. "Comprehensive approach to modeling and simulation of photovoltaic arrays". IEEE Transactions on Power Electronics, vol. 24(5), pp. 1198-1208, 2009.

J.-C. Wang, Y.-L. Su, J.-C. Shieh, and J.-A. Jiang. "High-accuracy maximum power point estimation for photovoltaic arrays". Solar Energy Materials & Solar Cells, vol. 95, pp. 843-851, 2011.

A.A. Willoughby, and M.O. Osinowo. "Development of an electronic load IV curve tracer to investigate the impact of Harmattan aerosol loading on PV module performance in southwest Nigeria". Solar Energy, vol. 166, pp. 171-180, 2018.

J.H. Wohlgemuth, M.D. Kempe, and D.C. Miller. "Discoloration of PV encapsulants". In: 39th IEEE Photovoltaic Specialists Conference, pp. 3260-3265, 2013.

P. Wolf, and V. Benda. "Identification of PV solar cells and modules parameters by combining statistical and analytical methods". Solar Energy, vol. 93, pp. 151-157, 2013.

World Health Organization, "Climate change and health", https://www.who.int/news-room/fact-sheets/detail/climate-change-and-health, 2021.

P. Würfel, T. Trupke, T. Puzzer, E. Schäffer, W. Warta, and S. Glunz. "Diffusion lengths of silicon solar cells from luminescence images". Journal of Applied Physics, vol. 101(12), 123110, 2007.

T. Zdanowicz. "The interactive computer program to fit IV curves of solar cells". In: Proceedings of 12th European Photovoltaic Solar Energy Conference, pp. 1311-4, 1994.

Y. Zhu. "An adaptive I-V curve detecting method for photovoltaic modules". In: IEEE International Power Electronics and Application Conference and Exposition, Shenzhen, China, pp. 1-6, 2018.

Y. Zhu, and W. Xiao. "A comprehensive review of topologies for I-V curve tracer". Solar Energy, vol. 196, pp. 346-357, 2020.

APPENDIX. DETERMINATION OF THE PV MODULE ELECTRICAL CHARACTERISTICS AT STC

Practical experiments have shown that the STC characteristic values ($I_{SC,STC}$, $I_{MPP,STC}$, $U_{OC,STC}$, $U_{MPP,STC}$) of the NAPS NP190GK PV module 19 differ from the values provided in the module's datasheet and thus must be redefined so that they can be utilised in the proposed curve fitting procedure applied to the current-voltage measurement data. For this purpose, among the measurements of the *I-U* curves performed for PV module 19, curves measured under stable environmental conditions close to the STC were searched. In total, 11 consecutive curves were accepted for the analysis. These curves were measured on 24 August 2020, which is close to the measurement dates of the experimental datasets used in this thesis. This guarantees that the redefined STC characteristic values are up to date for this thesis.

The PV module operating conditions of the investigated 11 *I-U* curves belong to the irradiance range of 980-1000 W/m² and PV cell temperature range of 24-25 °C. One should note that STC irradiance and PV cell temperature seldom occur in Finland. Usually, such conditions occur only during the irradiance transient following cloud shading, when the cloud enhancement phenomenon increases the irradiance received by the PV module. Therefore, the available operating conditions closest to STC were selected.

The 11 *I-U* curves accepted for analysis were treated as follows. First, the developed fitting procedure was applied to each curve using the initial PV module datasheet values as initial guesses for the fitted parameters. The actual I_{SC} and U_{OC} of the fitted curve were determined as the y- and x-axis intercepts, and the $I_{MPP,STC}$ and $U_{MPP,STC}$ were determined at the MPP of the fitted curve. Secondly, because of the strong irradiance dependence of the current quantities, the formulae

$$I_{\mathrm{MPP,STC}} = \frac{G_{\mathrm{STC}}}{G} I_{\mathrm{MPP}} \tag{A1}$$

and

$$I_{\mathrm{SC,STC}} = \frac{G_{\mathrm{STC}}}{G} I_{\mathrm{SC}} \tag{A2}$$

were employed to scale the determined currents with the measured irradiance to obtain the first estimates for the STC values to be discovered. In contrast, the obtained OC and MPP voltage were left unscaled, since the irradiance dependence of these quantities at high irradiance levels is negligible, so these values themselves served as the first STC estimates. Moreover, no temperature scaling was performed for the other four quantities, since the measured PV module backplate temperatures were very close to the STC temperature. After obtaining these first estimates of $I_{\mathrm{SC,STC}}$, $I_{\mathrm{MPP,STC}}$, $U_{\mathrm{OC,STC}}$, and $U_{\mathrm{MPP,STC}}$ for each of the 11 curves, the values of each parameter were averaged to obtain new guesses for the fitted parameters. The fitting procedure was then repeated iteratively until the obtained STC values converged. The final STC values for the electrical parameters are shown in Table A.1. As can be seen, the variance of the obtained STC values of the 11 fitted curves is very small, so their averages can very well be used as representative values for PV module 19. To demonstrate the accuracy of the fitting procedure utilising the determined STC characteristics, Fig. A.1 shows an example of the final fitted *I-U* curve jointly with the original data for the last, eleventh *I-U* curve.

Table A.1. Operating conditions and the determined electrical STC characteristics for the 11 measured *I-U* curves of PV module 19.

Time	G (W/m²)	T (°C)	$I_{\mathrm{SC,STC}}$ (A)	$I_{\mathrm{MPP,STC}}$ (A)	$U_{\mathrm{OC,STC}}$ (V)	$U_{\mathrm{MPP,STC}}$ (V)
10.04.37	984.4	24.56	8.721	7.949	32.80	23.03
10.04.38	984.9	24.56	8.719	7.946	32.79	22.99
10.04.39	984.8	24.56	8.713	7.938	32.79	22.97
10.04.40	984.8	24.56	8.719	7.931	32.78	22.95
10.04.41	985.1	24.57	8.717	7.925	32.76	22.93
10.04.42	985.8	24.58	8.720	7.929	32.75	22.91
10.04.43	988.2	24.59	8.722	7.930	32.74	22.89
10.04.44	990.4	24.60	8.707	7.947	32.72	22.84
10.04.45	992.3	24.61	8.713	7.944	32.72	22.83
10.04.46	995.1	24.64	8.710	7.945	32.71	22.82
10.04.47	996.9	24.66	8.708	7.942	32.70	22.82
Average	988.4	24.59	8.715	7.939	32.75	22.91

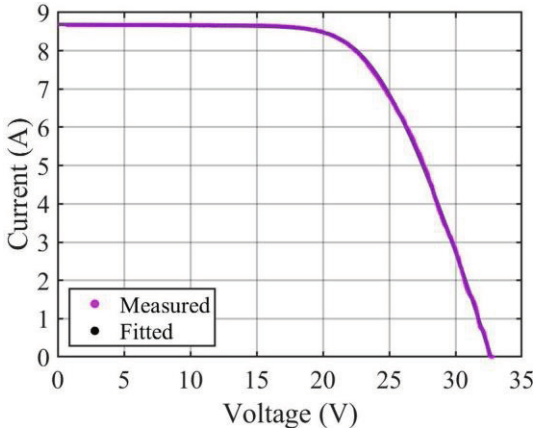

Figure A.1. The fitted curve jointly with the measured eleventh *I-U* curve used to determine the STC characteristic values of PV module 19.